CZECH TECHNICAL
UNIVERSITY
IN PRAGUE

FACULTY
OF MECHANICAL
ENGINEERING

MASTER'S
THESIS

2022

VOJTĚCH
SMOLÍK

ČVUT
ČESKÉ VYSOKÉ UČENÍ TECHNICKÉ V PRAZE

ZADÁNÍ DIPLOMOVÉ PRÁCE

I. OSOBNÍ A STUDIJNÍ ÚDAJE

Příjmení: **Smolík** Jméno: **Vojtěch** Osobní číslo: **465523**

Fakulta/ústav: **Fakulta strojní**

Zadávající katedra/ústav: **Ústav energetiky**

Studijní program: **Jaderná energetická zařízení**

Studijní obor: **Jaderná energetická zařízení**

II. ÚDAJE K DIPLOMOVÉ PRÁCI

Název diplomové práce:

Technologie odvodu vysokých tepelných toků

Název diplomové práce anglicky:

High Heat Flux Cooling Technology

Pokyny pro vypracování:

V teoretické části práce student provede rešerši současného stavu vývoje fúzních elektráren. V závěru rešerše se zaměří na teoretický rozbor přestupu tepla a technologie umožňující odvod vysokých tepelných toků. V praktické části práce student provede CFD simulaci kanálu hypervapotron podle J. Milnese s použitím stejných okrajových podmínek, ale v odlišném softwarovém řešiči.
Při prezentaci modelu bude student klást důraz na grafickou dokumentaci procesů probíhajících v kanálu, především na tvorbu a zánik parních bublin. Vytvořený model porovná s dostupnými experimentálními daty a zhodnotí, jak vytvořený model odpovídá experimentům. V dalším kroku student porovná model s modely vytvořenými dříve v jiných CFD simulačních prostředích a provede analýzu shody modelů s naměřenými daty. Na závěr práce student zhodnotí přínos hypervapotronu pro intenzifikaci přestupu tepla a možnosti simulovat děje podchlazeného varu pomocí softwaru ANSYS Fluent.

Seznam doporučené literatury:

J. Milnes. Computational Modelling of the HyperVapotron Cooling Technique for Nuclear Fusion Application, Disertační práce, 2010. Department of Aerospace Sciences Cranfield University Cranfield, UK.
P. Domalapally, F. Subba, “Computational thermal fluid dynamic analysis of hypervapotron heat sink for high heat flux devices application,” Fusion Engineering and Design, vol. 98-99, pp. 1267–1270, 2015.

Jméno a pracoviště vedoucí(ho) diplomové práce:

Ing. Slavomír Entler, Ph.D. ústav energetiky

Jméno a pracoviště druhé(ho) vedoucí(ho) nebo konzultanta(ky) diplomové práce:

Ing. Pavel Zácha, Ph.D. ústav energetiky FS

Datum zadání diplomové práce: **21.04.2022** Termín odevzdání diplomové práce: **03.06.2022**

Platnost zadání diplomové práce: **31.12.2023**

Ing. Slavomír Entler, Ph.D.
podpis vedoucí(ho) práce

podpis vedoucí(ho) ústavu/katedry

doc. Ing. Miroslav Španiel, CSc.
podpis děkana(ky)

III. PŘEVZETÍ ZADÁNÍ

Diplomant bere na vědomí, že je povinen vypracovat diplomovou práci samostatně, bez cizí pomoci, s výjimkou poskytnutých konzultací.
Seznam použité literatury, jiných pramenů a jmen konzultantů je třeba uvést v diplomové práci.

Datum převzetí zadání

Podpis studenta

Declaration

I declared that this thesis is entirely my own work and that where material could be construed as the work of others, it is fully cited and referenced, and/or with appropriate acknowledgement given.

in Prague, 25. May 2022

Bc. Vojtěch Smolík

Acknowledgment

I would like to thank my supervisors Ing. Slavomír Entler, Phd. and Ing. Pavel Zácha, Phd. for their great support. Also thanks to Ing. Miroslav Gleitz for advice and suggestions.

Finally, I'd like to thank my family and the closest ones for their support which has been invaluable in completing this work.

Annotation

Type of publication	Master's Thesis
Author	Bc. Vojtěch Smolík
Title	Hypervapotron - High Heat Flux Cooling Technology
Academic year	2021/2022
Department	Department of Energetics Nuclear Power Engineering Equipment
Supervisor	Ing. Slavomír Entler, PhD.
Co-supervisor	Ing. Pavel Zácha, PhD.
Number of pages	95
Number of figures	84
Number of tables	19
Number of attachments	4

Keywords CFD, hypervapotron, subcooled boiling, fusion, tokamak, heat transfer

Abstract

Master's thesis deals with the CFD simulation of hypervapotron subcooled cooling. The first part of this thesis focuses on the current state of nuclear fusion research, description of cooling technology, heat transfer theory and analysis of experimental and numerical works conducted on hypervapotron. Numerical part includes CFD calculations of hypervapotron using ANSYS Fluent and validation of results. Results are then compared with other thesis to evaluate the quality of used model.

Abstract (Czech)

Diplomová práce se zabývá CFD simulací podchlazeného varu v hypervapotronu. V první části práce je zhodnocen současný stav vývoje jaderné fúze, popsány technologie odvodu tepla, teorie přestupu tepla a rešerše předchozích prací zabývajících se problematikou hypervapotronu. Numerická část obsahuje CFD výpočty hypervapotronu pomocí nástroje ANSYS Fluent a následnou validaci výsledků. Získané hodnoty jsou porovnány s výsledky předchozích prací provedených na toto téma pro zhodnocení kvality použitého výpočetního modelu.

Hypervapotron
High Heat Flux Cooling Technology

Contents

List of Figures

List of Tables

List of Shortcuts

ASDEX	Axially Symmetric Divertor Experiment
CANDU	Canada Deuterium Uranium
CCWS	Component Cooling Water System
CFD	Computational Fluid Dynamics
COMPASS	Compact Assembly
DEMO	Demonstration Power Plant
DD	Deuterium Deuterium
DT	Deuterium Tritium
DNB	Departure From Nucleate Boiling
ECH	Electron Cyclotron Heating
ESS	Energy Storage System
HRS	Heat Rejection System
HSP	High Speed Photography
ICH	Ion Cyclotron Heating
INTF	Indian Test Facility
IPP	Institute for Plasma Physics
ITER	International Thermonuclear Experimental Reactor
JET	Joint European Torus
MAST	Mega Ampere Spherical Tokamak
NBI	Neutral Beam Injection
NIF	National Ignition Facility
PHTS	Primary Heat Transfer System
PIV	Particle Image Velocimetry
PLIF	Planar Laser-Induced Fluorescence
RPI	Rensselaer Polytechnic Institute
TCWS	Tokamak Cooling Water System
VVER	Water-Water Energetic Reactor
W7-X	Wendelstein 7-X

List of Symbols

A	$[m^2]$	area
C	$[m]$	circumference
c_p	$[J \cdot Kg^{-1} \cdot K^{-1}]$	specific heat capacity
D_H	$[m]$	hydraulic diameter
E_F	$[J]$	released fusion energy
f	$[Hz]$	bubble departure frequency
h	$[J \cdot Kg^{-1}]$	enthalpy
I	$[-]$	turbulence intensity
k	$[J \cdot Kg^{-1}]$	turbulence kinetic energy
p	$[Pa]$	pressure
Pr	$[-]$	Prandtl number
q	$[W \cdot m^{-2}]$	heat flux
Re	$[-]$	Reynolds number
T	$[^\circ C]$,$[K]$	temperature
T_w	$[^\circ C]$	wall temperature
T_l	$[^\circ C]$	liquid temperature
T_r	$[s]$	rotation time
u^+	$[-]$	non-dimensional velocity
v	$[m \cdot s^{-1}]$	velocity
y^+	$[-]$	non-dimensional distance
α	$[-]$	relaxation factor
ε	$[m^2 \cdot s^3]$	turbulence energy dissipation rate
λ, k	$[W \cdot m^{-1} \cdot K^{-1}]$	thermal conductivity
μ	$[Pa \cdot s]$	dynamic viscosity
ν	$[m^2 \cdot s^{-1}]$	kinematic viscosity
ρ	$[Kg \cdot m^{-3}]$	density
σ	$[N \cdot m^{-1}]$	surface tension
$<\sigma_\nu>$	$[m^2]$	fusion cross section
τ_ω	$[Pa]$	wall shear stress

Part I
Theoretical Part

1 Nuclear Fusion

1.1 Introduction

Energy source selection is always a compromise between cost, environmental impact, safety and many other factors. Fossil fuels do not represent a perspective solution due to their limited occurrence and the carbon dioxide production resulting from their usage. Solar and wind power plants are dependent on variable weather conditions, unable to provide a stable power supply. Hydroelectric power plants require the construction of large dams, negatively affecting the selected region and its ecosystems. Moreover, for example, the Czech Republic and other Central European countries have almost entirely used up the building potential for new hydroelectric dams.

The utilization of nuclear energy was a breakthrough for energetics. The fission chain reaction of uranium 235 opened a new way to provide a low emission power supply. The crucial benefit of nuclear plants is the density of energy stored in nuclear fuel: energy stored in 1 gram of uranium is equivalent to 3 tons of coal. One-third of the power consumption in the Czech Republic is currently provided by pressurized light-water (moderated and cooled) reactors, type VVER. Current fission energetics are limited by negative public perception of this energy source caused largely by the nuclear waste production. Nuclear fusion represents a revolutionary way of obtaining nuclear energy. Fusion power plants will not produce any long-lived fission products (half-life more than 200 000 years). Construction materials activated by neutron radiation will be the only radioactive waste produced by the fusion power plant. There are many types of fusion reactions, some of them do not produce any neutrons, so it is possible to operate a fusion power plant completely without radioactive waste.

One fusion power plant development problem is the extreme conditions required to sustain the fusion reaction. It is impossible to scale down the fusion reactor to a prototype model. Instead, it is necessary to build a full-size reactor, which requires a significant investment. Furthermore, in the case of an accident, it is physically impossible to create a spontaneous chain reaction: the fusion fuel will simply cool down and stop reacting. This inherent safety can influence public opinion about nuclear energy in countries avoiding current nuclear fission power plants.

1.2 Principle of Fusion Reactions

The nucleus of an atom is composed of positively charged protons and neutrons without charge. For example, let us consider the nucleus of helium: two protons and two neutrons. Common sense says that the total rest mass of this nucleus is equal to the sum of its parts, but the actual mass is slightly lower. This difference is known as *the mass defect*, and it represents the energy (*the binding energy*) that was released when a nucleus was created. Binding energy can also be understood as the energy needed to split a nucleus into individual particles. The relation between the binding energy E and the mass defect Δm is expressed by the Einstein equation (1).

$$E = \Delta m \cdot c^2 \tag{1}$$

Binding energy value depends on the composition of a nucleus, takes on different values for different isotopes. Figure 1 shows the relation between the average binding energy per nucleon and the number of nucleons in the nucleus of common isotopes. For example, the isotope of iron ^{56}Fe reaches the maximum value of 8.79 MeV per nucleon. Isotopes with fewer nucleons than ^{56}Fe can release energy by nuclear fusion. Conversely, isotopes with more nucleons can release energy by fission. The most suitable isotopes for nuclear fusion are in the area near hydrogen ^{1}H (1 proton), which has zero binding energy. The energetic product of any fusion reaction can be determined as the difference between the binding energies of reactants and their products. For the current research, the most important reaction for fusion energetics is the Deuterium-Tritium (DT) reaction, expressed by the following equation (2).

$$D + T \longrightarrow \; ^4He(2.5MeV) + n(14.1MeV) \tag{2}$$

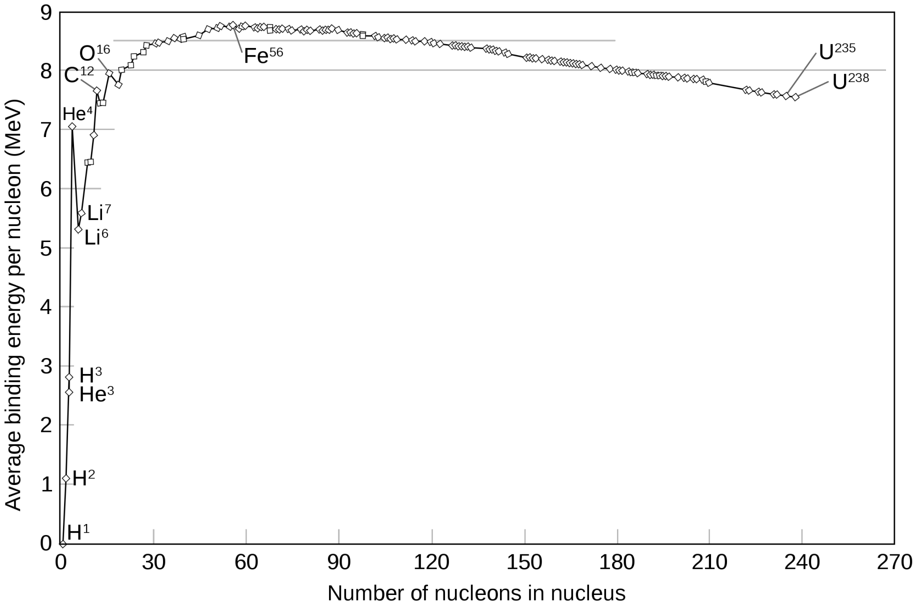

Figure 1: The Binding Energy Curve [1]

1.3 Proton-Proton Cycle

Nuclear fusion is also the source of energy of stars: therefore, the origin of all sources found on Earth except for tide force. The chain of reaction inside stars is called the proton-proton cycle. In its first phase, two protons are fused to create one deuterium, a positron and an electron neutrino. It is important to note that two protons cannot fuse directly due to their equal positive charge. In this reaction, one proton is recreated to a neutron by the beta+ decay. Beta+ decay is shown in the Feynman diagram in Figure 2.

$$p + p \longrightarrow {}^{2}H + e^{+} + \upsilon_e \tag{3}$$

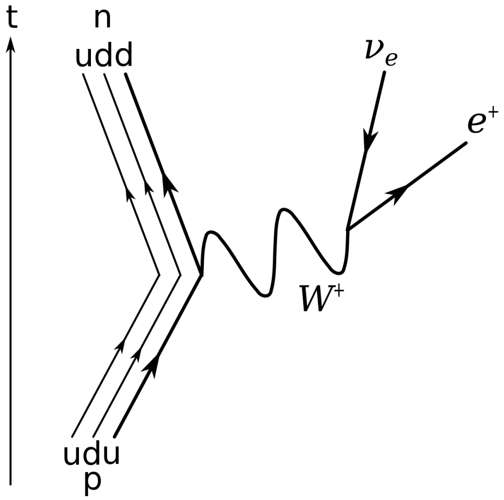

Figure 2: The Feynman Diagram of Beta+ Decay

In the next phase, deuterium reacts with a proton, creating one atom of helium ^{3}He and a gamma ray.

$$D + p \longrightarrow {}^{3}He + \gamma \tag{4}$$

In the final phase, two atoms of ^{3}He are fused, creating one ^{4}He and two protons.

$${}^{3}He + {}^{3}He \longrightarrow {}^{4}He + 2p \tag{5}$$

Fusion reactions inside stars are essential as a source of energy and as the source of new elements in our Universe. In the life cycle of stars, elements with proton numbers lower than 56 are created by fusion reactions. Energy input is needed to create elements of higher proton numbers. Those elements can be naturally created only in the final stage of the life cycle of stars, during the explosion [2].

1.4 Achieving the Fusion Reaction

Present physical description of the Universe describes the four fundamental interactions: gravitational, electromagnetic and strong and weak nuclear forces. In the case of interaction between two atoms, the gravitational force is negligibly weak. The weak nuclear force was mentioned in Beta+ decay, where the W boson represents it. Major forces present in the interaction between individual atoms are repulsive electromagnetic force and attractive strong nuclear force. The resulting potential between two atoms is shown in Figure 3. In order to make a fusion reaction happen, it is necessary to surpass the high potential Coulomb barrier and reach the area of strong nuclear interaction. On the scale of the atom nucleus, the quantum effects are appearing, helping the nucleus surpass the barrier. Particle described by the probability distribution in space can go beyond the high potential barrier by the effect called quantum tunnelling". This effect helps us to achieve the fusion reaction.

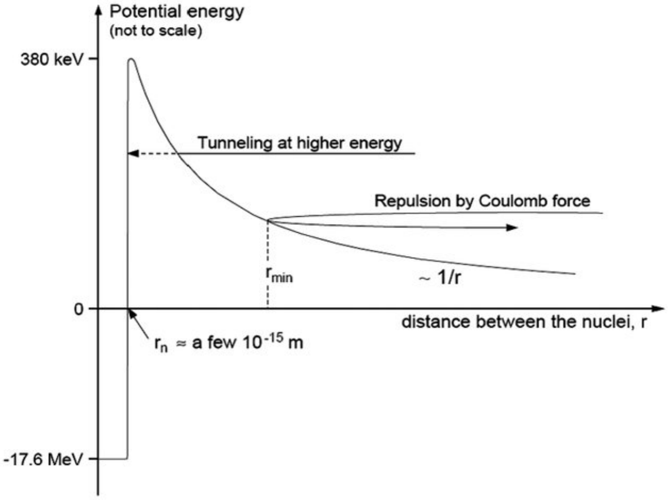

Figure 3: The Potential Energy [3]

Atoms need to have high energy to surpass the repulsive forces. The probability of a fusion reaction between two atoms is expressed as the cross section. Fusion cross sections versus centre-of-mass energy for some fusion reactions is shown in Figure 4. The goal is to achieve the maximum probability of a fusion reaction.

1.5 Lawson Criterion

In 1995, the British physicist J. D. Lawson expressed the energy balance of thermonuclear reactors, creating a vision for fusion power plants. In the article *Some Criteria for a Power Producing Thermonuclear Reactor* [5] , he concluded that the DD and DT reactions are the most suitable for achieving a power breakeven. The parameter R expresses the ratio between energy release in the plasma and the energy supplied. The efficiency of power returned to the reaction is set to *1/3*, which results in the criterion of *R>2*.

$$\eta(R+1) > 1 \tag{6}$$

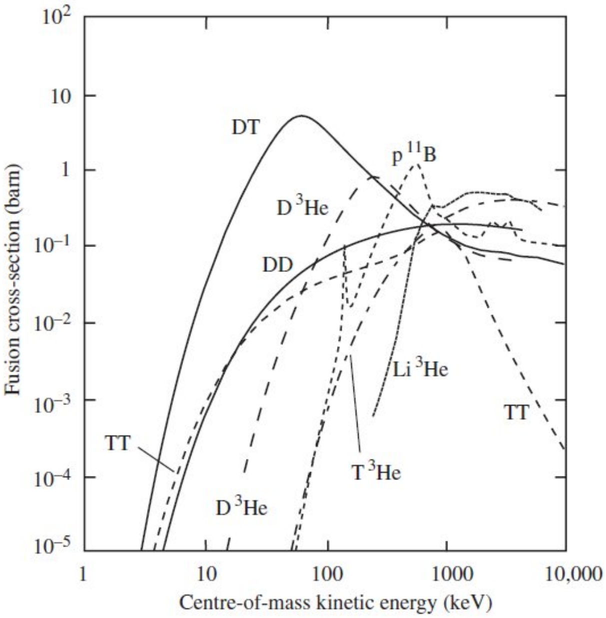

Figure 4: The Fusion Cross Section [4]

$$R = \frac{tP_R}{tP_B + 3nkT} = \frac{P_R/3n^2kT}{P_B/3n^2kT + 1/nT} \tag{7}$$

P_R is the power of a fusion reaction, P_B represents energy loss. Both values depend on the square of density n^2, the R parameter is the function of temperature, density and time. Lawson defines time t as *a time, for which the gas temperature is maintained*. Present forms of the Lawson criterion use energy confinement time τ_E. Energy confinement time is defined as the ratio of plasma internal energy per loss of power (8). The Lawson criterion for tokamaks (10) is defined as a triple product $nT\tau_E$.

$$\tau_E = \frac{W_P}{P_L} \tag{8}$$

The present form of Lawson criterion

$$n\tau_E \geq f(T) \qquad [m^{-3}s] \tag{9}$$

Lawson criterion (Ignition) for the DT reaction in tokamaks

$$nT\tau_E \geq \frac{60T^2}{< \sigma_\nu > E_F} \qquad [m^{-3}eVs] \tag{10}$$

1.6 Overview of Fusion Reactions

There is a wide range of fusion reactions available for energetic utilization. Reactions are in general divided in two groups based on the presence of neutron as a reaction product. Presence of neutrons as a fusion product is associated with many technical and safety difficulties (activated construction materials).

1.6.1 Neutronic Reactions

$$D + T \longrightarrow {}^4He + n + 17.6\ MeV \tag{11}$$

$$D + D \longrightarrow T + p + 4.03\ MeV \tag{12}$$

$$D + D \longrightarrow {}^3He + n + 3.27\ MeV \tag{13}$$

$$T + T \longrightarrow {}^4He + 2n + 11.33\ MeV \tag{14}$$

$$T + {}^3He \longrightarrow {}^4He + n + p + 12.1\ MeV \tag{15}$$

(The probability of DD reaction producing T + p, or $^3He + n$ is 50:50.)

1.6.2 Aneutronic Reactions

$$D + {}^3He \longrightarrow {}^4He + p + 18.35\ MeV \tag{16}$$

$${}^6Li + {}^3He \longrightarrow 2\ {}^4He + p + 16.9\ MeV \tag{17}$$

$$D + p \longrightarrow {}^3He + \gamma + 5.49\ MeV \tag{18}$$

$${}^3He + {}^3He \longrightarrow {}^4He + 2p + 12.86\ MeV \tag{19}$$

$$p + {}^{11}B \longrightarrow 3\ {}^4He + 8.7\ MeV \tag{20}$$

After analyzing the Lawson criterion of all possible fusion reactions, the DT reaction is achievable at the lowest temperature. DT reaction belongs to the category of neutronic reactions, meaning one of the products is a neutron. The first generation of fusion reactors will be based on neutronic reactions. However, damage to the reactor materials will significantly increase the costs of power plant operation: therefore, the long-term pursuit is to achieve aneutronic reactions. D^3He reaction is an aneutronic reaction achievable at the lowest temperature of 50 keV (580 mil. K). The fundamental problem of D^3He fuel is that the ^3He isotope does not occur naturally on Earth in a sufficient amount. The nearest deposits of ^3He are on the Moon: therefore, this reaction is a solution of the far future [6] [7].

1.7 Technical Realization

The fuel is in the plasmatic phase in the temperature range of fusion reactions. The fundamental characteristics of plasma are:

- There are free carriers of electric charge in the plasma.
- Plasma exhibits collective behavior. It responds to electric and magnetic fields as well as creates them.
- Plasma is quasi-neutral: macroscopic volume contains the same amount of positive and negative charges.

The collective behavior of plasma creates many different types of plasma instabilities. The stability of plasma is crucial for the operation of magnetically confined plasma devices. Plasma is also able to conduct current. When an electric current passes through plasma, the pinch effect forces the current-carrying particles together [8].

1.8 Magnetic Confinement - Tokamak

The magnetic confinement prevents contact between the plasma and the reactor wall. The plasma will cool down immediately after touching the wall, breaking the fusion reaction. The tokamak device is a toroidal chamber set around a transformer core, which induces the current in the plasma. The poloidal magnetic field created by the current in the plasma is combined with the toroidal field of coils set around the torus. The resulting magnetic field takes a helical shape, shown in Figure 5.
Large tokamaks contain blanket on the inner side of the vacuum chamber, protecting the superconducting coils from the neutron flux.

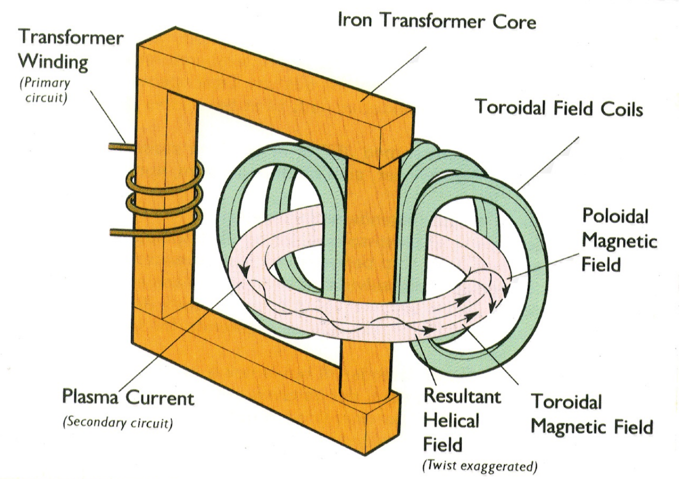

Figure 5: The Tokamak [9]

The products of the DT fusion reaction are the neutron and the alpha particle. The neutron carries around 4/5 of the released fusion energy, corresponding with the mass ratio between the alpha particle and the neutron (Momentum Conservation Principle). Neutrons can be captured by the blanket and release their energy in the form of heat. Alpha particles produced in the DT reaction are positively charged, unable to leave the magnetically confined plasma. Accumulating alpha particles in the plasma is negatively affecting the fusion reaction. The fusion reaction will stop working at a particular concentration of alpha particles.

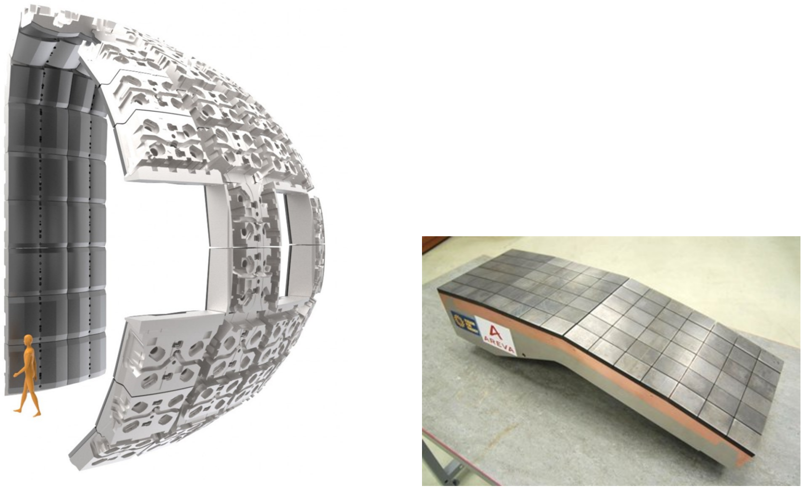

(a) The Blanket, ITER (b) The First Wall, ITER

Figure 6: The Blanket and The First Wall [9]

The first wall is directly facing the plasma, protecting the blanket in the case of contact with hot plasma. Following this event, only the damaged section of the first wall needs to be replaced. Protecting the structure of tokamak is essential because the quality of the material is declinig and the material itself becomes radioactive waste. However, in contrast with radioactive waste created in fission reactors, these materials are only low-activated. Choosing the materials of the tokamak structure creates another advantage: we can determine the radioactive waste composition. The vision for the future generation of fusion reactors is to achieve aneutronic fusion reactions, preventing the creation of any neutron-activated materials. In tokamaks built for energy production, the blanket will also have the function of tritium breeding. Tritium needed for a DT reaction is (unlike deuterium) not naturally occurring on Earth in the required amount. Tritium has a half-life of 12.3 years: it can be produced by the reaction of lithium and neutron (21)(22) [10].

$$^{6}Li + n \longrightarrow \ ^{4}He + T + 4.8MeV \tag{21}$$

$$^{7}Li + n \longrightarrow \ ^{4}He + T + n - 2.5MeV \tag{22}$$

The divertor is a tokamak component designed to extract helium from the plasma to keep the conditions required for the fusion reaction. The edge magnetic field lines are guided from the edge regions of the plasma to the divertor region.

The divertor (Figure 7) is located at the bottom of the vacuum vessel (it is theoretically possible to create the second divertor at the top of the vacuum vessel or many more ones). ITER divertors consist of an inner vertical target, an outer vertical target and a dome. It is divided into 54 individual cassettes. Divertor targets are in direct intentional contact with the plasma. They are the most thermally stressed components of the tokamak. Materials able to withstand the thermal conditions of the divertor are tungsten or molybdenum. Regular replacement of these highly stressed materials is considered for the fusion power plant operation.

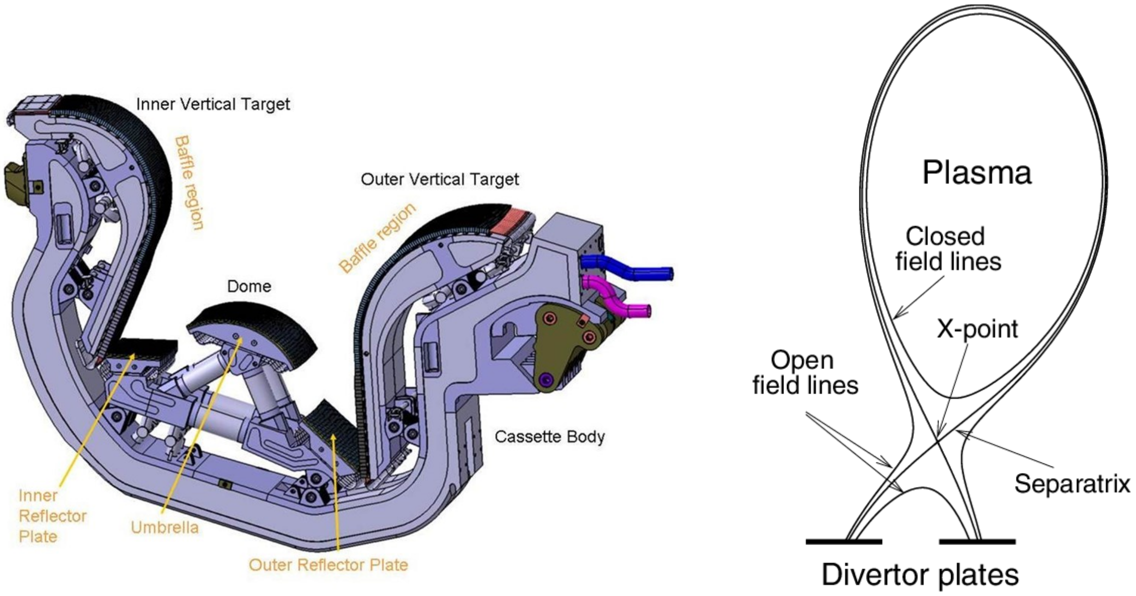

(a) The Divertor, ITER (b) The Magnetic Field Lines

Figure 7: The Divertor [11]

Plasma heating in the tokamak is provided in various ways, the primary method is ohmic heating. The plasma resistance decreases with increasing plasma temperature, limiting the heating ability of the current conducted in the plasma. High currents can also cause plasma instabilities. Therefore the heating is supported by neutral beam injection (NBI), electron cyclotron heating and ion cyclotron heating. The process of the neutral beam injection has four phases. The first phase is deuterium ionisation. An electromagnetic field accelerates ionised atoms. Then, the beam of particles is neutralised in the chamber filled with gas. Neutralised atoms can enter the magnetic field of tokamak and heat the plasma. The remaining charged parts must be magnetically diverted to the targets. The neutral beam injector targets are under heavy heat flux, similar to the first wall of the tokamak. From the viewpoint of thermodynamics, cooling of NBI targets and the first wall is an identical problem. Another heating method is using a high-intensity beam of electromagnetic radiation. This system is divided into two frequency ranges: ion cyclotron heating (ICH) and electron cyclotron heating (ECH). Cyclotron heating and NBI systems can generate current in the plasma non-inductively.

1.9 Stellarator

The stellarator (Figure 8) is an alternative concept to the tokamak. It is based on the same principle of magnetic confinement but with an entirely different coil geometry. Electromagnetic coils of the stellarator are designed to provide the most stable plasma flow. The complicated geometry of coils is the biggest challenge of stellarator research and development. Plasma in the stellarator does not conduct a current: it is heated only by the neutral beam injection and cyclotron heating. As a result, the stellarator should be able to operate continually, in significantly longer pulses than the tokamak.

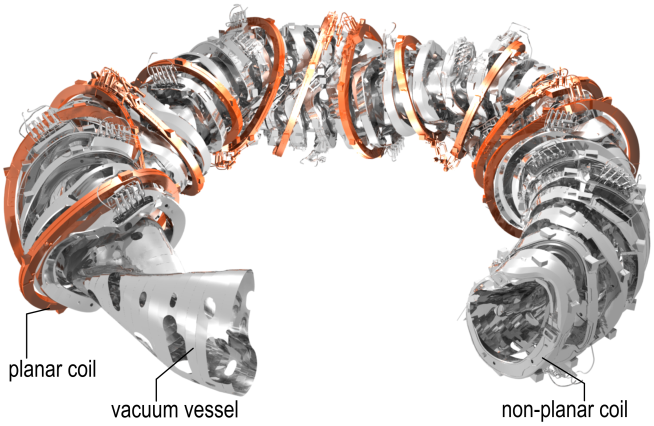

Figure 8: The Stellarator [12]

1.10 Inertial Confinement

The principle of inertial confinement is in the rapid compression of a small amount of fuel to reach the density and temperature necessary for the fusion reaction. A laser pulse heats the fuel pellet: the evaporated material then exerts pressure on the fuel. As the pellet surface reaches the plasmatic phase, it creates an impermeable plasma layer, so that the fuel can be further heated only by an infra-red laser beam. Any irregularity of the fuel pellet can cause uneven expansion and destruction of the pellet. The fuel pellet can be placed inside the tube called *the hohlraum* and heated indirectly to solve some of those problems.

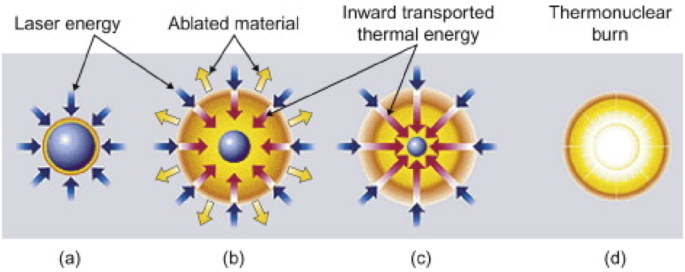

Figure 9: The Direct Inertial Confinement [13]

The fuel pellet (target, capsule) is a plastic or a glass ball with a diameter in the range of millimetres. One of the most common types of hohlraum is a golden cylinder with an opening at both bases and the fuel pellet placed in the centre. Laser beams are targeted through openings inside the cylinder, heating its surface. The inner surface of the hohlraum enters the plasmatic state and generates a soft x-ray radiation. The fuel pellet is then compressed by radiation simultaneously from all sides [14].

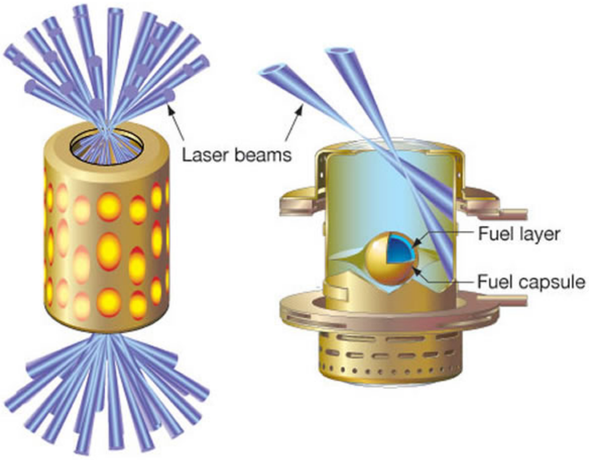

Figure 10: The Indirect Inertial Confinement [15]

The pulse mode of inertial confinement is inconvenient for continually operating power generation. One pulse explosion takes 10^{-9} seconds, so the frequency of pulses would have to be unfeasibly high. Another problem is also in the construction of the reactor chamber, providing the removal of released energy. In the present state of research, inertial confinement does not have as much potential for fusion energetics as the magnetic confinement. The inertial fusion leading research is centred in The National Ignition Facility (NIF) in California [15].

1.11 Fusion Energy Gain Factor

The biggest challenge of nuclear fusion research and development is creating a device that produces more energy than it consumes to heat the fuel. This balance of energies is represented by the fusion energy gain factor Q, the ratio of produced fusion power to the power required to maintain the plasma in a steady state.

$$Q = \frac{P_F}{P_H} \tag{23}$$

The breakeven value (or scientific breakeven) is Q=*1*, i.e. energy consumption and production are equal. This scientific breakeven does not consider the efficiency of the fusion reactor facility, which is described in the engineering breakeven. For $Q \geq 1$, the reaction is successfully producing the energy. The ignition is another critical threshold. In this phase of the DT reaction, plasma heating is fully covered by the alpha particles created by the fusion reaction itself. The ignition state represents the most significant benefit of nuclear fusion, the goal of scientific research [16].

1.12 Present and Future Fusion Projects

1.12.1 Joint European Torus

The Joint European Torus (JET) was built in the 1980s in the Culham Centre for Fusion Energy in the United States. It was built to reach the scientific breakeven (Q=1). In 1997, JET reached the record value $Q=0.67$ by producing 16 MW while consuming 24 MW of thermal power. The JET tokamak has undergone many changes and upgdrades since its original design. Currently, the JET is taking an essential role in testing and developing technologies for the ITER project. The similarity of the JET and the ITER tokamaks are, for example, in the ”D” shape of the vacuum chamber. The JET heating system consists of a 25 MW neutral beam source and a 15 MW cyclotron heating. During the plasma pulse, JET consumes around 500 MW of power (peaking at 1000 MW). Since the draw from the grid is limited to 575 MW, two 775-ton flywheel generators are installed to provide this power demand [17] [18].

1.12.2 International Thermonuclear Experimental Reactor

The International Thermonuclear Experimental Reactor (ITER) is the second most expensive scientific device built by humankind (the first one is ISS). The international agreement to build ITER was approved in 1985 by Ronald Reagan and Mikhail Gorbachev to develop peaceful uses of nuclear fusion. After years of planning and delays, in 2006, it was finally decided to build ITER in Caradache in southern France. The tokamak and all the support systems are currently under construction: the first plasma operation of ITER is planned for December 2025. It is important to note that the goal of ITER is not to produce any power output. The fusion power released in the tokamak will be fully transferred to cooling towers, not to the turbine and the generators. The goal of the ITER tokamak is to achieve the fusion energy gain factor $Q \geq 10$ by producing 500 W of fusion heat power and testing all the technologies needed for power plant operation. The ITER will test control and diagnostics systems, cryogenics, heating, remote maintenance, and so on [19].

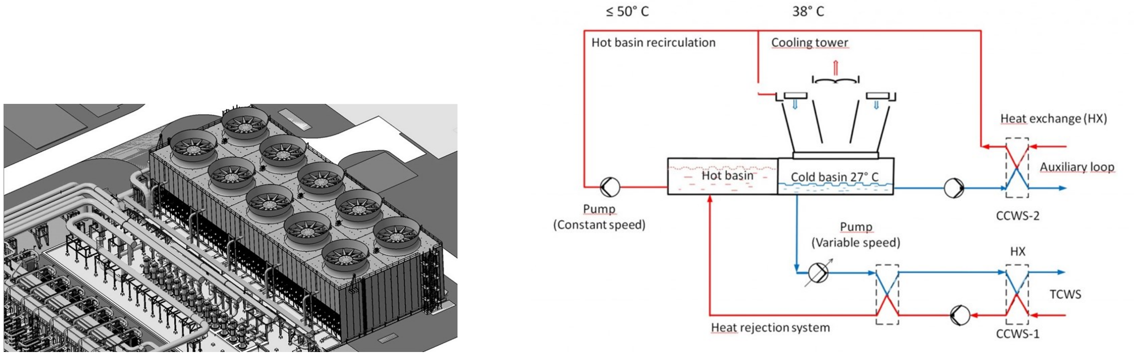

(a) Cooling Towers, ITER [9]

(b) The Heat Rejection System [20]

Figure 11: The ITER Cooling Systems

Cooling of some of the first wall panels and the divertor targets of ITER is based on hypervapotron technology, the topic of this thesis which is described in detail in the next chapter. Tritium needed for the DT reaction will not be producted by lithium breeding, but it will be supplied externally (from the CANDU reactors). The ITER's blanket purpose is to transfer the thermal energy and protect the structure of the vacuum vessel. Some breeding blanket modules will be installed on ITER, but only for testing and research. ITER blanket is cooled by water. From the peak power of 1100 MW, 960 MW will be cooled by the TCWS (Tokamak Cooling Water System) loop: the remaining 140 MW are transferred by the CCWS-2 (Component Cooling Water System). Both systems are connected to the HRS (Heat Rejection System), which transfers heat power through cooling towers to the atmosphere. Cooling towers of the ITER are not the usual "Iterson" type: they are based on the forced flow by fans to increase efficiency. Currently, the cooling towers (Figure 11(a)) are already installed on the site of ITER.

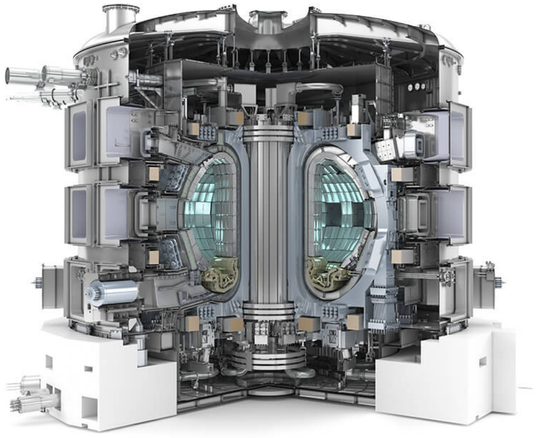

Figure 12: The ITER Tokamak [9]

1.12.3 COMPASS-Upgrade

The COMPASS tokamak was a fusion device operated in 2008-2021 on the Institute of Plasma Physics in Prague. Initially, the tokamak was constructed in the Culham Center for Fusion Energy in the United Kingdom in the 1989. At this moment, the COMPASS tokamak is under complete reconstruction to COMPASS-Upgrade. Although some supporting systems will remain, the tokamak itself will be completely replaced. Besides COMPASS, there are only two operational tokamaks (JET, ASDEX-U) with ITER-like configuration worldwide. Despite the smaller size compared to the ITER, small tokamaks play an essential role in fusion research.

1.12.4 Wendelstein 7-X stellarator

Wendelstein 7-X (W7-X) is an experimental stellarator (Chapter 1.9) constructed in Griefswalds Max Planck Institute for Plasma Physics (IPP). It was completed in October 2015 as the biggest stellarator built to advance the stellarator design and demonstrate its function. The geometry of W7-X is shown in Figure 8. The major radius of W7-X is 5.5 m, with a magnetic field of 5 T and heating power 14 MW. The purpose of W7-X is not to produce electricity, but to demonstrate the ability of a stellarator to operate in long (30 minutes) plasma pulses. For the fusion power plant operation, longer plasma pulses are the main advantage compared to tokamaks. Since no current is conducted in plasma, heating is provided by microwaves and neutral beam injection. The assembly of W7-X required more than 1 million hours of work [12].

1.12.5 Demonstration Power Plant

The Demonstration Power Plant (DEMO) represents an intermediate step between a research device and a fully functional power plant. DEMO's goal is to demonstrate the net production of electric power by nuclear fusion. The design of the DEMO power plant will be based on the results of project ITER, so there are no final proposals of DEMO design yet. One of the critical functions of DEMO is tritium production in the breeding blanket. There are four leading European concepts of the breeding blanket: HCPB, HCLL, WCLL and DCLL. Each concept is characterised by the coolant (HC = He, WC = water) and the type of tritium breeder in the form of pebble bed (PB) or liquid lithium lead (LL). Test modules of the breeding blanket will be tested on ITER to find out which is the most suitable and efficient. Another vital role of the DEMO blanket is to transfer energy from the plasma to steam generators and turbines to generate electricity. The Primary Heat Transfer System (PHTS) design depends on the coolant medium (He or water). The biggest challenge of heat transfer between the blanket and the turbine is the pulse operation of the tokamak. Pulses of 120-minute *burn* phase will be followed by a 30-minute shutdown *dwell* phase. The Energy Storage System (ESS) will be installed to compensate for the burn/dwell phases and output stable power load to the turbine. One of the solutions is to store heat energy in the tanks of molten salt. Power conversion to electrical energy can be based on the traditional Rankin-Clausius cycle or the supercritical CO_2 cycle [21].

Table 1: An Overview of Tokamak Parameters

	Gain Factor Q [-]	Magnetic Field [T]	Major Radius [m]
JET	0.67	3.45	2.96
COMPASS	-	0.9-2.1	0.56
COMPASS (U)	-	5	0.9
ITER	10	5	6.2
DEMO	25	dependend on the outcome of ITER	

1.12.6 Operating Tokamaks Overview

An overview of tokamak experimental research can give an interesting perspective to evaluate the current state of fusion research. The Figure 13 shows the sum of installed heating power of all tokamaks and the corresponding type of heating in time. The Figure 14 shows the total number of operating tokamaks and the sum of their toroidal field, since the toroidal field is one of the main tokamak characteristics. There are observable similarities between the number of operating tokamaks and the number of nuclear power plants under construction.

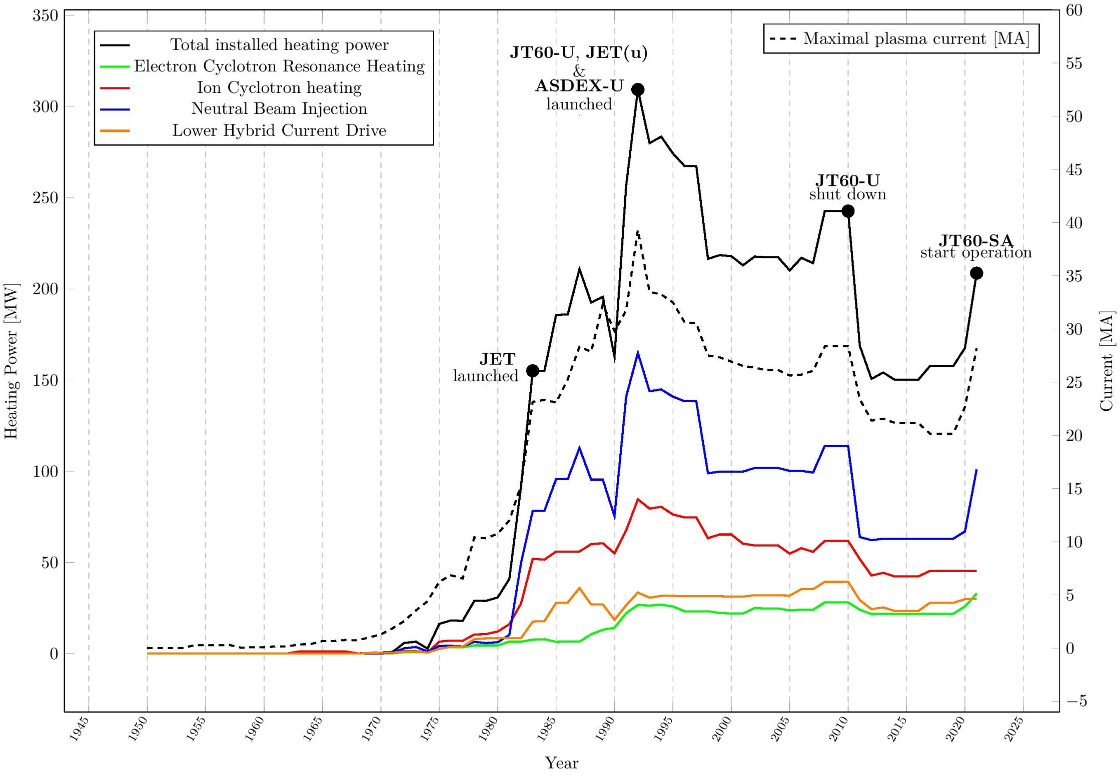

Figure 13: Installed Tokamak Heating Power

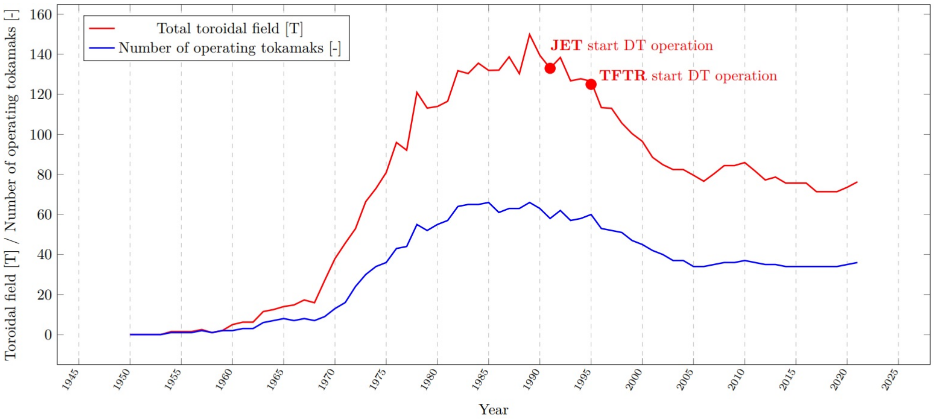

Figure 14: Number of Operating Tokamaks

2 High Heat Flux Cooling Technology

High heat flux can be defined as heat flux higher than 1 MW.m^{-2}. Although first wall panels of the ITER tokamak are designed for a "normal heat flux" of the order of 1-2 MW.m^{-2}, some panels (in the upper region of the reactor) will be required to withstand an "enhanced heat flux" up to 5 MW.m^{-2}. Divertor targets are components exposed to the highest heat load of 10-20 MW.m^{-2}. Besides nuclear applications, cooling such high heat flux is also crucial in developing electronic devices. As computer technology evolves, natural or forced air convection will not provide enough heat removal capability. Possible solutions for more powerful cooling are single-phase liquids flowing in microchannels through a heat sink, two-phase microchannel cooling, a heat sink with a porous layer instead of microchannels, jet impingement or spray cooling.

2.1 Single-phase and Two-phase Cooling

Single-phase cooling is the foundation of pressurised water reactors (PWR). PWRs are designed to keep the water in the primary circuit constantly in the liquid state. Evaporations on the surface of cooled objects create a vapour film on the surface, which decrease heat transfer efficiency and cause local overheating, an unacceptable situation in the nuclear reactor. This effect is referred to as the boiling crisis. Single-phase cooling design relies on keeping the water in the primary circuit under the critical pressure. Keeping the cooling loop constantly under certain pressure does increase the requirements for the piping system and increases the costs.

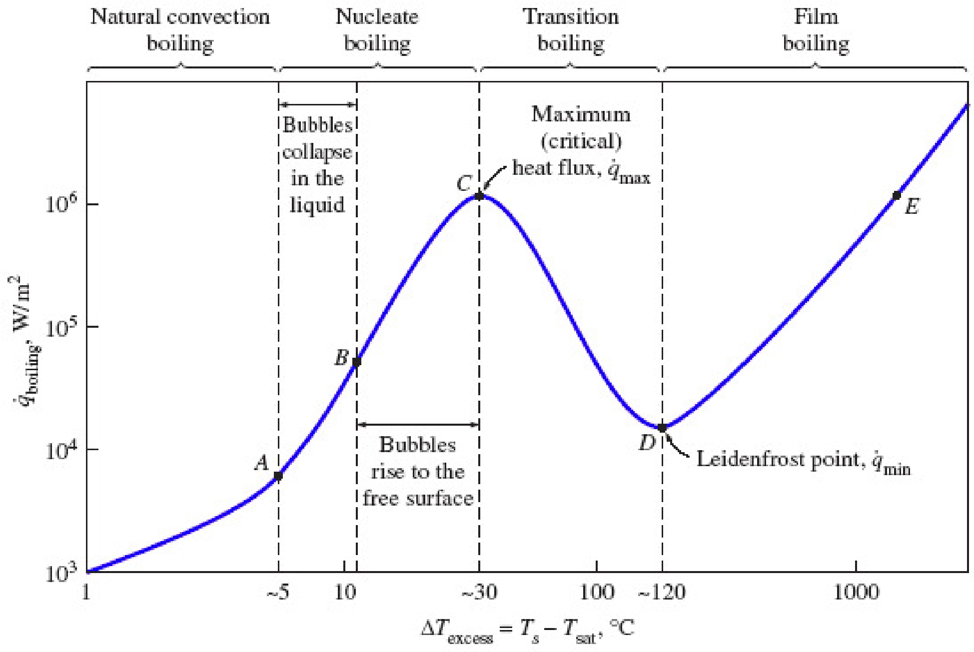

Figure 15: The Nukiyama Boiling Curve [22]

Two-phase cooling does include a phase change of cooling liquid (vaporisation and condensation). This complex phenomenon was studied in the 1930s by Japanese physicist Dr. Shiro Nukiyama, who measured the correlation between heat flux and wall temperature. The Figure 15 shows this correlation described by the boiling curve with several significant values. This boiling curve describes a natural flow without external forces (e.g., pump). In the "natural convection boiling" area below point A, any fluid motion is caused only by natural convection currents. Point A does represent the moment of formation of the first gas bubbles in the liquid. In the region between points A and B formed bubbles are collapse before reaching the free surface of the liquid: bubbles are also not interacting with each other. This motion of bubbles causes a stirring of the liquid, increasing the heat transfer. Between points B and C, bubbles are formed at such a high rate that they form columns of vapour in the liquid. These bubbles can now reach the surface of the liquid and release their vapour content - evaporation and motion of liquid results in more significant heat fluxes in this region. Point C represents the maximum (critical) heat flux. After reaching the critical value, heat flux decreases due to the formation of the vapour film on the heater surface, the area beyond point C is called a departure from nucleate boiling (DNB) or boiling crisis. The "transition boiling" region between points C and D represents a gradual transition from nucleate to film boiling. At point D, nucleate boiling is entirely replaced by film boiling. Point D is also called "the Leidenfrost point", related to the Leidenfrost effect. A stable vapour film fully covers the heater surface beyond the Leidenfrost point (point D). The heat flux in this region increases with increasing surface temperature by heat radiation through the vapour film. Point E in Figure 15 represents achieving the critical heat flux in the film boiling region.

2.2 Leidenfrost Effect

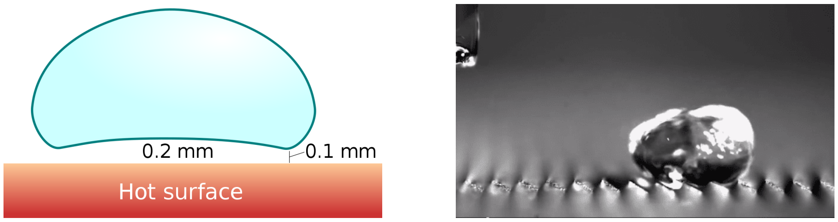

(a) A drop of liquid held up by a layer of vapour

(b) A drop of water placed on a hot surface with ridges

Figure 16: The Leidenfrost Effect [23]

The Leidenfrost effect (Figure 16a) represents the insulating ability of the layer of vapour between the drop of liquid and the heated surface, minimising the heat flux. As a result, the layer of vapour can not only keep the drop levitating over the hot surface but can also force the drop to movement. This movement can be achieved by creating a series of sloped ridges on the hot surface, as shown in Figure 16b. The Leidenfrost effect also allows dry ice to levitate on top of solid surfaces as it changes from solid to vapour phase.

2.3 Subcooled Boiling

Subcooled boiling occurs when the liquid near the heated surface is boiling, but the temperature of the main body of the liquid is below the boiling point (saturation temperature T_{SAT}). As a result, vapour bubbles are created, but they collapse back to the liquid state, unable to reach the surface. In the case of flowing liquid, vapour bubbles collapse in the main stream of liquid, enhancing the total heat flux from the hot surface to the cooling liquid. A subcooled boiling regime gives higher heat fluxes for the exact temperature difference than single-phase convection [24].

Stable subcooled boiling near the maximum (critical) heat flux can be achieved with the optimal combination of channel geometry and liquid parameters. In the case of the ITER tokamak, there are several types of cooling channel geometries: swirl tubes (twisted tape inside a tube), tubes and hypervapotron. The vertical divertor targets of tokamak ITER consist of tungsten blocks with swirl tube channels: divertor targets represents the area of a tokamak with the highest heat flux up to 20 $\mathrm{MW.m^{-2}}$. The ITER first wall, with the area of 600 $\mathrm{m^2}$, is the largest component of the cooling system. The cooling of "enhanced heat flux" first wall panels is based on the hypervapotron design.

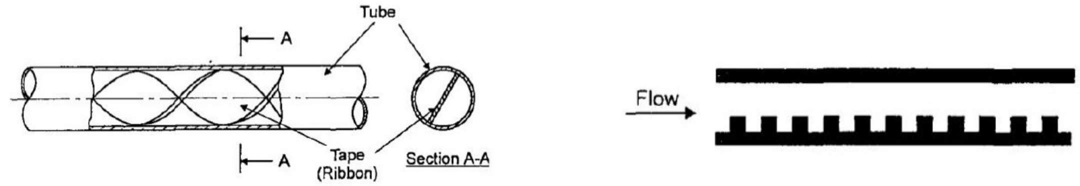

(a) Swirl Tube

(b) Hypervapotron

Figure 17: The Cooling Channel Geometry

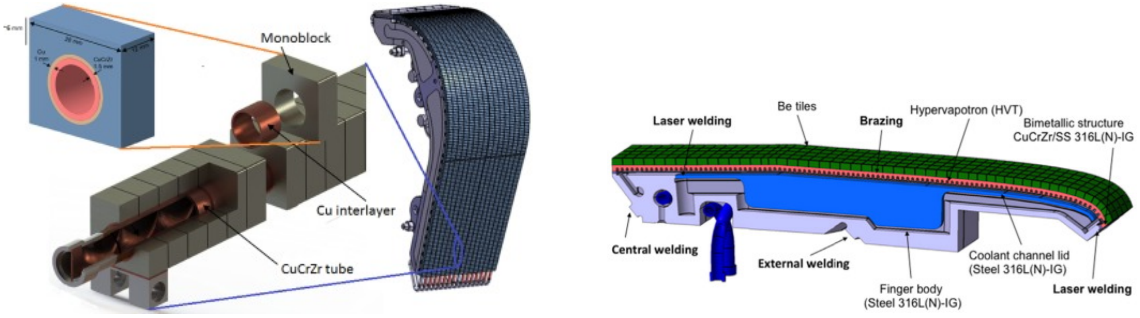

(a) The Vertical Target of Divertor

(b) The Finger of The First Wall

Figure 18: The Cooling Channel Construction for ITER [25]

3 Heat Transfer Theory

3.1 Fundamental principles

There are three types of heat transfer: conduction, convection and radiation.

3.1.1 Radiation

The heat energy of an object is related to the thermal motion of its particles. It is the main idea behind the kinetic theory of gasses but also applies to liquids and solids. This thermal motion of particles generates electromagnetic radiation, emitting energy from the object. Heat transfer by radiation is expressed by **the Stefan-Boltzmann law** (24), the Planck's law describes the spectral density of thermal radiation.

$$q'' = \sigma \cdot \varepsilon \cdot T^4 \quad [MW.m^{-2}] \tag{24}$$

σ is the Stefan-Boltzmann constant ($\sigma = 5.67 \cdot 10^{-8}$ $[W \cdot m^{-2} \cdot K^{-4}]$), ε is the object emissivity ($0 \leq \varepsilon \leq 1$), T equals to the temperature of radiating object.

3.1.2 Conduction

Particle collisions cause conductive heat transfer. Heat flows from a point with a higher temperature to a colder point, approaching the thermal equilibrium. Conduction heat flux density equals the product of thermal conductivity λ [W . m^{-1} . K^{-1}] (depends on the material) and the negative temperature gradient, expressed by the Fourier's law (25). Thermal conductivity can be simplified as a constant value, but it does depend on the temperature of the material. For an isotropic material, **Fourier's law** (25) can be extended to a heat equation (26). Material ability to transfer heat is represented by thermal diffusivity α [mm^2.s^{-1}].

$$q'' = -\lambda gradT \quad [MW.m^{-2}] \tag{25}$$

$$\frac{\partial T}{\partial t} = \alpha \left(\frac{\partial^2 T}{\partial x^2} \frac{\partial^2 T}{\partial y^2} \frac{\partial^2 T}{\partial z^2} \right) \qquad \alpha = \frac{\lambda}{\rho \cdot c_p} \tag{26}$$

3.1.3 Convection

Convection of heat occurs in fluids and is caused by the motion of the cooling medium. Liquid or gas is heated near the hot surface: it becomes less dense and forced to move away from the heat source. **Newton's law of cooling** (27) states the relationship between the temperature difference and the heat flux density. The temperature difference is defined by the mean temperature of fluid T_∞ and temperature of wall T_{wall}. The heat transfer coefficient h [W . m^{-1} . K^{-1}] does have a wide range of values, numerous methods and correlations calculate it. Calculating the subcooled boiling heat transfer in the hypervapotron does require a complex CFD model.

$$q'' = h \cdot (T_\infty - T_{wall}) \quad [MW.m^{-2}] \tag{27}$$

3.2 Eulerian Two-phase Model

CFD codes solving this two-phase model are based on conservation equations for each phase's mass, momentum and energy. Interactions between two phases are calculated based on the interfacial density model. The liquid phase is assumed to be a continuous, and the vapour phase is dispersed in form of spherical bubbles. Equations (28) to (31) represent conservation equations for one of two phases.

mass equation:

$$\frac{\partial}{\partial t}(\alpha_i \rho_i) + \nabla \cdot (\alpha_i \rho_i \vec{v}_i) = S_i + \dot{m}_{ji} - \dot{m}_{ij} \tag{28}$$

momentum equation:

$$\frac{\partial(\alpha_i \rho_i \vec{v}_i)}{\partial t} + \nabla \cdot (\alpha_i \rho_i \vec{v}_i \vec{v}_i) = - \alpha_i \nabla p + \nabla \vec{\vec{\tau}}_i + \alpha_i \rho_i \vec{g} \tag{29}$$

$$+ \dot{m}_{ji} \vec{v}_j - \dot{m}_{ij} \vec{v}_i + \vec{F}_{D,i} + \vec{F}_{L,i} + \vec{F}_{wl,i} + \vec{F}_{td,i} + \vec{F}_{vm,i} \tag{30}$$

energy equation:

$$\frac{\partial}{\partial t}(\alpha_i \rho_i h_i) + \nabla \cdot (\alpha_i \rho_i \vec{v}_i h_i) = \alpha_i \frac{\partial p_i}{\partial t} - \nabla \cdot \vec{q}_i + S_i + Q_{ij} + \dot{m}_{ji} h_j - \dot{m}_{ij} h_i \tag{31}$$

$\alpha_i, \rho_i, \vec{v}_i, P_i, \vec{\vec{\tau}}_i, h_i$ and $\vec{q}_i$ are the volume of fraction, density, velocity, source term, pressure, stress tensor, specific enthalpy and heat flux for i phase, $\dot{m}_{ji}$ and Q_{ji} are the energy and mass transfer from jth to ith phase, forces F in the energy conservation equation represents the drag force, lift force, wall lubrication force, turbulence dispersion force and virtual mass force.

3.3 Standard Wall Boiling Model

Total heat flow (32) from the heated wall to the fluid is divided into three parts: the single-phase convective heat flux q_C , the evaporate heat flux q_E and the wall quenching heat flux q_Q.

$$q_W = q_C + q_E + q_Q \begin{cases} q_C = h_C(T_w - T_l)(1 - A_b) \\ q_E = V_d N_w \rho_q h_{fg} f \\ q_Q = \dfrac{2\sqrt{k_l \rho_l c_{c,p} f}}{\sqrt{\pi}}(T_w - T_l) \end{cases} \tag{32}$$

the proportion of heated wall covered by bubbles:

$$A_b = min\left(1; K\frac{N_w \pi d_{bw}^2}{4}\right) \tag{33}$$

empirical constant K:

$$K = exp\left(-\frac{\rho_l c_{p,l}(T_w - T_l)}{80 \rho_q h_{fg}}\right) \tag{34}$$

active nucleate site density:

$$N_w = 210^{1.805}(T_w - T_{sat})^{1.805} \tag{35}$$

the frequency of bubble departure:

$$f = \frac{1}{T} = \sqrt{\frac{4g(\rho_l - \rho_g)}{3d_{bw}\rho_l}} \tag{36}$$

h_c is the coefficient for single-phase turbulent heat transfer, T_w and T_l are wall and fluid temperatures, ρ_l and ρ_g are densities of liquid and vapour phase, h_{fg} is the latent heat of evaporation, V_d is the volume of the bubbles based on the bubble departure diameter, $c_{p,l}$ and k_l are the specific heat and conductivity of liquid phase.

diameter of departing bubbles:

$$d_{bw} = min\left(0.0006 \cdot e^{\left(-\dfrac{\Delta T_{sub}}{45.0}\right)}; 0.0014\right) \tag{37}$$

Equation (37) is used as the default setting of the CFD model in ANSYS Fluent: this equation is based on empirical correlations. Other methods to calculate the bubble departure diameter are the Kocamustafaogullari and Ishi equation (38) or the Unal correlation (39).
Ψ represents the contact angle in degrees. Results of the Unal correlation are in millimetres.

Kocamustafaogullari and Ishi correlation:

$$d_w = 0.0012(\rho^*)^{0.9} \cdot 0.0208 \cdot \Psi\sqrt{\frac{\sigma}{g(\rho_l - \rho_v)}} \tag{38}$$

Unal correlation:

$$d_w = 2.4210^{-5} P^{0.709}\left(\frac{a}{b\sqrt{\varphi}}\right) \tag{39}$$

$$a = \frac{\Delta T_{sup}}{2\rho_g H_{lv}}\sqrt{\frac{\rho_s C_{ps} k_s}{\pi}} \tag{40}$$

$$b = \begin{cases} \dfrac{\Delta T_{sub}}{2(1 - \dfrac{\rho_g}{\rho_l})} e^{\frac{\Delta T_{sub}}{3} - 1} & \text{for } \Delta T_{sub} \leq 3 \\ \dfrac{\Delta T_{sub}}{2(1 - \dfrac{\rho_g}{\rho_l})} & \text{for } \Delta T_{sub} > 3 \end{cases} \tag{41}$$

$$\varphi = max\left(\left(\frac{U_b}{U_0}\right)^{0.47}; 1.0\right) \tag{42}$$

4 Hypervapotron

The term ”vapotron” refers to a channel with cooling fins to intensify the heat flux from the heated wall to the cooling liquid. In a ”supervapotron”, cooling fins are parallel to the forced flow of liquid. Supervapotron can achieve maximal heat flux of 3 MW.m^{-2}. Narrowing the slots between the fins can increase the heat flux to 5 MW.m^{-2}. Cooling fins in hypervapotron are perpendicular to the flow of cooling liquid. This design allows more intense vapour production in the slots, increasing the possible heat flux to 20 MW.m^{-2}. Some studies [26] have been conducted on the hypervapotron cooled by tetrafluoroethane (R134a), a standard refrigerator coolant with the boiling point at -26.3 $^{\circ}C$, but the available research focuses on the water-cooled hypervapotron [27].

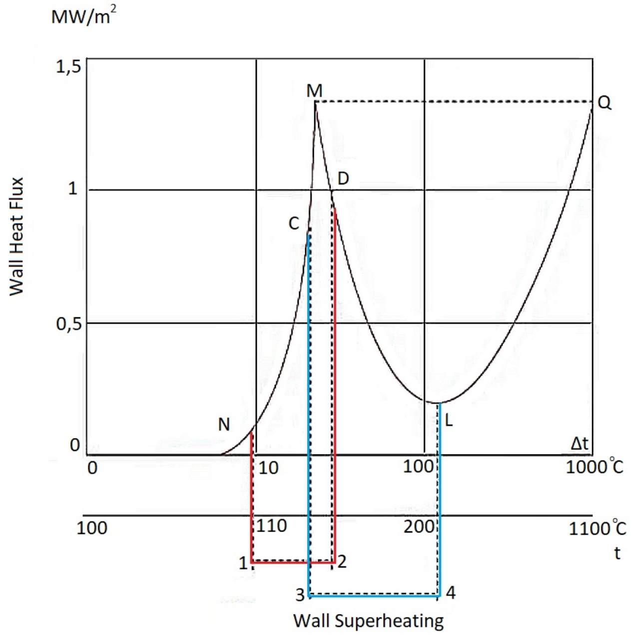

Figure 19: Boiling Curve of Vapotron (red) and Hypervapotron (blue)

4.1 Geometry of Hypervapotron

The Figure 20(a) shows the most common type of hypervapotron geometry with the visualisation of the flow between the fins. Fins can be rectangular, triangular, in the shape of the sin curve or many other variations (Figure 20(b,c,d)), but always perpendicular to the liquid flow. Some experiments with fins under a certain angle to the main flow have been realized, but perpendicular fins are still the main focus of research and development. The geometry in the figure 20(a) corresponds with the hypervapotron installed on tokamak JET in Culham in the United Kingdom. Hypervapotrons in JET are being used for example as beam stopping elements in both Neutral Beam Injectors and in the Neutral Beam Test Bed. The JET hypervapotron is made of CuCrZr: the device has operated since 1986.

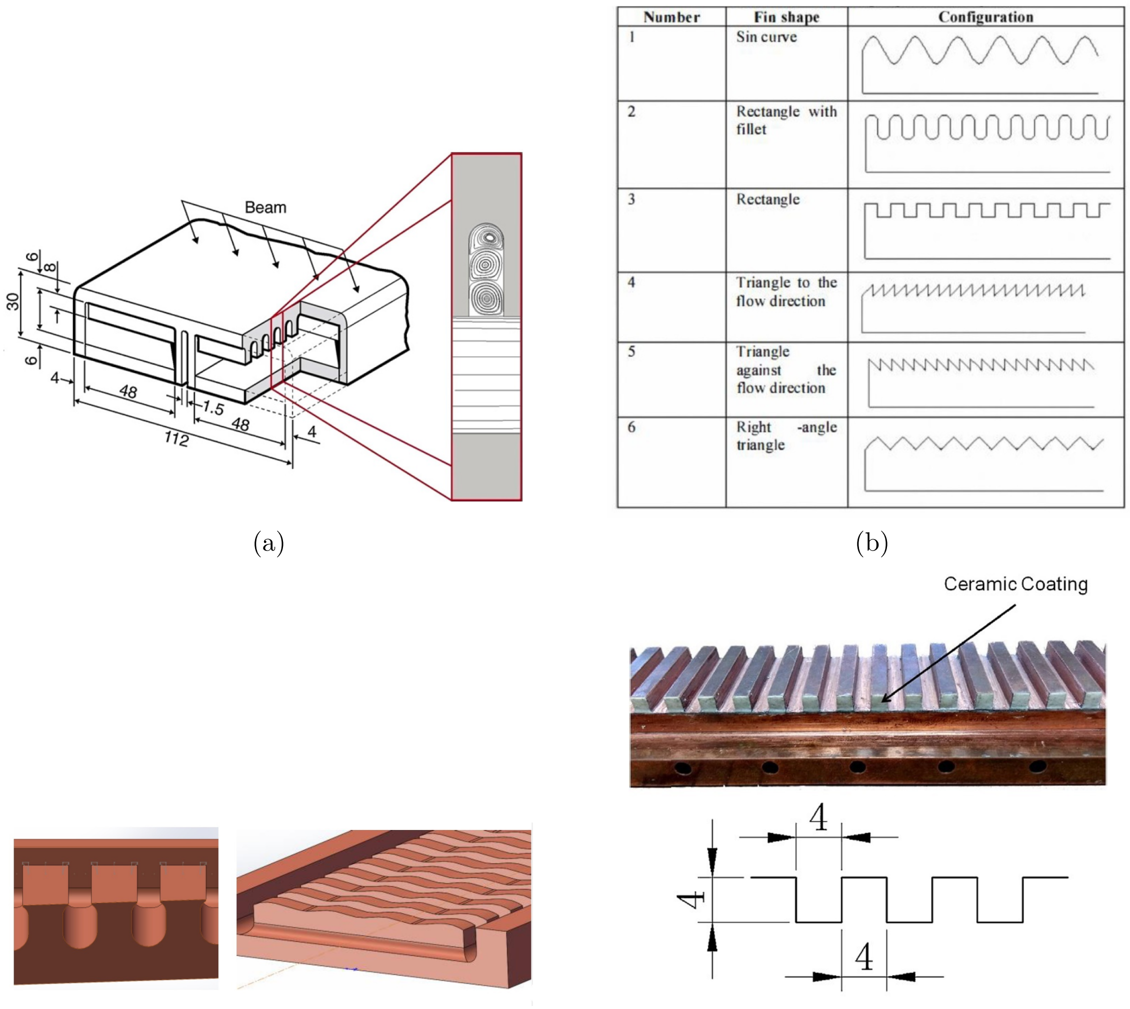

Number	Fin shape	Configuration
1	Sin curve	
2	Rectangle with fillet	
3	Rectangle	
4	Triangle to the flow direction	
5	Triangle against the flow direction	
6	Right -angle triangle	

(a)

(b)

(c)

(d)

Figure 20: Variations of Hypervapotron Design [27]

4.2 Pressure Drop in Hypervapotron

To determine the hydraulic resistance and required pumping power, equation (44) can calculate the pressure drop in a hypervapotron. Equation (43) shows the hydraulic diameter of hypervapotron with a channel height of h and a width of w. Hydraulic loss is proportional to the square of flow velocity v, L is the length of the channel, ρ_l is the density of flowing liquid, A_{vap} and A_{feed} are cross sections of the channel.

$$d_h = \frac{2(h \cdot w)}{h + w} \tag{43}$$

$$\Delta p_v = \frac{\rho_l}{2} \cdot v^2 \left(\zeta_1 \cdot \frac{L}{d_h} + \zeta_2 \cdot \left(\frac{A_{vap}}{A_{feed}} \right)^2 \right) \tag{44}$$

4.3 Nanofluids

Hypervapotron cooling with nanofluids is an alternative way to improve heat transfer performance. Nanofluids are deionised water-based suspensions with alumina (Al_2O_3) nanoscale particles with 10 to 40 nm in diameter, improving thermal conductivity. The concentration of nanoparticles depends on the purpose of the experiment. Mass fraction of 0.0001 % and particle diameter of 1 μm are used for particle image velocimetry (PIV). PIV is a method used to measure of the spatial distribution of the flow velocity in transparent fluids. Particles in the fluid are highlighted by pulsating laser and recorded with a camera. The framerate of the camera is synchronised with laser pulses. By comparison of consecutive frames, a two-dimensional vector field is created. Figure 21(a) shows the example of the result of particle image velocimetry measurement [28].

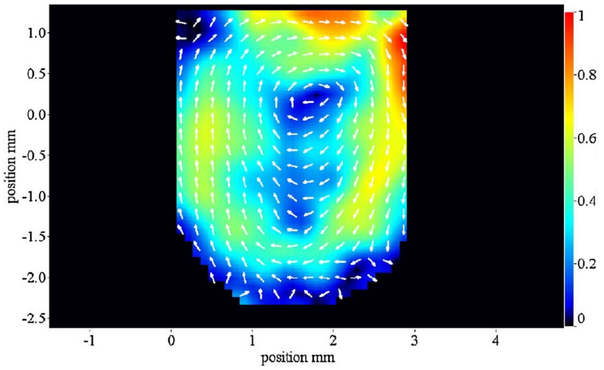

(a) The Particle Image Velocimetry

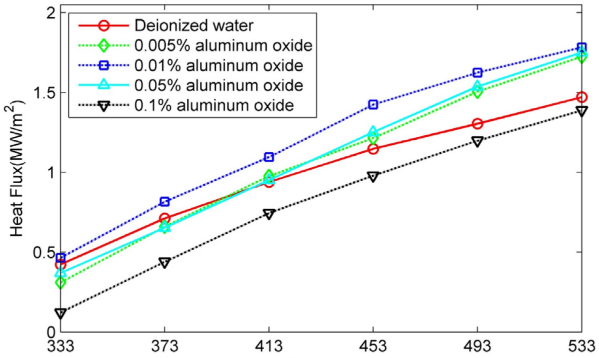

(b) Heat transfer performance of deionized water and four different mass fractions of alumina–water nanofluids

Figure 21: Nanofluids [28]

Higher nanoparticle concentrations can also be used to improve the thermal conductivity of the cooling liquid. Nanofluids with mass fractions of 0.005%, 0.01%, 0.05% and 0.1% were tested on hypervapotron with triangular fins (flow velocity of 2 m.s^{-1}), results of this experiment are shown in figure 21(b). Mass fraction of 0.01% increased the heat flux on average by 22%, compared to the deionised water [29].

5 Experimental Studies of Hypervapotron

5.1 National Research Foundation of Korea, 2020

The 2020 paper *"Experimental study of hypervapotron channel with square fin structure for divertor cooling by one-side, electric joule heating system"* [30] conducted at Pohang University of Science and Technology (POSTECH) is focused on the subcooled flow boiling heat transfer correlations in hypervapotron. An experimental loop, as shown in Fig. 22(a), was built to carry out stable heat load experiments with high heat flux, high pressure (20 bar) and high coolant temperature (150 $°C$). In order to simulate the heat flux conditions loaded on the plasma-facing component inside the tokamak, it is necessary to develop a heater capable of loading high heat flux in a one-side direction. Electric joule heating was selected as the most suitable method for the steady-state control of heat flux, simple manufacturing and low cost. Heating element material must have a high melting point, high resistivity and low thermal expansion coefficient. FeCrAl (Fe 72.2 %, Cr 22 %, Al 5.8 %) alloy was selected as the heat-generating material. Conjunction between the heating element and the hypervapotron channel was realized by spray coating of Al_2O_3 and thermal paste to reduce the high contact thermal resistance. Heat flux generated by the heating element can be calculated by the following equation:

$$Q = R \times I^2 \ [W] \qquad q'' = \frac{Q}{A} \ [W.m^{-2}] \tag{45}$$

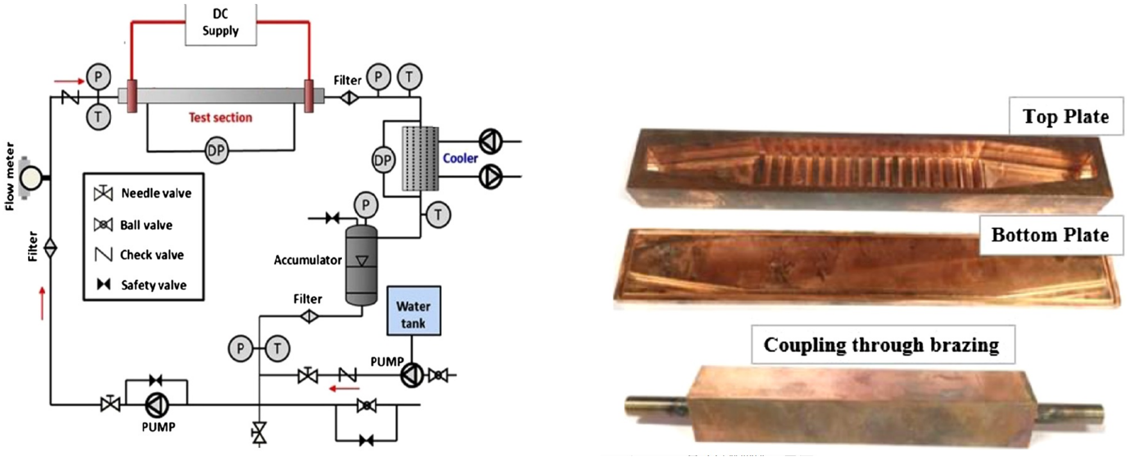

(a) Design of the experimental loop

(b) Manufactured Hypervapotron Cooling Channel

Figure 22: National Research Foundation of Korea, 2020

The Figure 22(b) shows the hypervapotron channel design used in an experiment: CuCrZr was selected as the building material. Hypervapotron fins are rectangular: the width, height, and spacing are 3 mm x 4 mm x 3 mm. In addition, ten thermocouples for temperature measurements were installed in the channel. Experiments were performed with flow rates ranging from 0.108 to 0.284 Kg.s^{-1} and inlet temperatures ranging from 100 to 140 $°C$. The maximal heat flux achieved in the experiment was 6.87 MW.m^{-2}.

Results of the experiment

In the area of nucleate boiling regime, the Shah correlation (1977) predicted values with an average error rate of 6.55 % and 2.94 % which suggests that Shah correlation predicts experimental results very well.

Shah correlation

The Boiling number:

$$Bo = \frac{q}{\dot{m} \cdot h_{fg}} \tag{46}$$

$$Bo > 0.3.10^{-4} \qquad \psi_0 = 230 \cdot Bo^{0.5} \tag{47}$$

$$Bo < 0.3.10^{-4} \qquad \psi_0 = 1 + 45 \cdot Bo^{0.5} \tag{48}$$

$$\textit{low subcooling region}: \qquad \psi = \psi_0 \tag{49}$$

$$\textit{high subcooling region}: \qquad \psi = \psi_0 + \frac{\Delta T_{SC}}{\Delta T_{SAT}} \tag{50}$$

$$\psi = \frac{q}{\Delta T_{SAT} \cdot h_L} \tag{51}$$

The low subcooling region corresponds to fully developed boiling, while the high subcooling region corresponds to partial or local boiling. ψ_0 is the value of ψ at zero subcooling and zero vapour quality, h_L is the heat transfer coefficient for all mass flowing as a liquid without any boiling, h_{fg} is the latent heat of vaporisation. Comparison of results with values calculated by Shan (1977) correlation are plotted in Fig. 23(a).

The condition for boiling:

$$\Delta T_{SAT} = (T_{WALL} - T_{SAT}) > 0 \tag{52}$$

Total heat flux:

$$q = q_{single\,phase\,convection} + q_{nucleate\,boiling} \tag{53}$$

$$q = h_L(T_{WALL} - T_B) + h_L(\psi_0 - 1)(T_{WALL} - T_{SAT}) \tag{54}$$

The second part of the experiment was focused on the heat flux of a fully developed subcooled flow boiling. The Figure 23(b) shows the results compared to other correlation predictions. For example, Thom (1965), Aladiev (1957) and Jens & Lottes (1951) predicted the heat flux two to three times lower than the experimental values, and do not agree well with the experiment. On the other hand, Kandlikar (1998) correlation predicted the heat flux reasonably good, with an average error rate of 16.57 %.

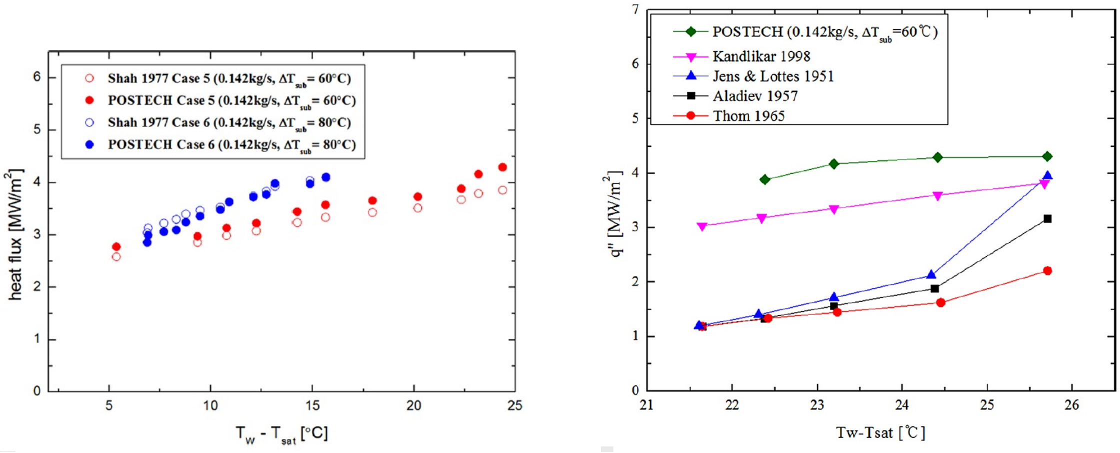

(a) Comparison with Shan (1977) correlation

(b) Comparison of results with other correlations

Figure 23: Results of The Experiment

Thom correlation

$$T_{WALL} = \frac{0.022 \cdot q^{0.5}}{exp\left(\dfrac{p}{8.6}\right)} + T_{SAT} \qquad 0.29 \leq q \leq 1.57 \quad [MW.m^{-2}] \tag{55}$$

Jens & Lottes correlation

$$T_{WALL} = \frac{0.79 \cdot q^{0.25}}{exp\left(\dfrac{p}{6.2}\right)} + T_{SAT} \qquad 3.5 \leq p \leq 14 \quad [MPa] \tag{56}$$

Kandlikar correlation

$$\dot{q} = \left(1058(\dot{m} \cdot h_{lg})^{-0.7} F_{fl} \alpha_{lo} \Delta T_{SAT}\right)^{\frac{1}{0.3}} \tag{57}$$

5.2 New Star Institute of Applied Technology, P.R. of China, 2014

The goal of this experiment was to observe the vortex evolvement and bubble characteristics of coolant between the fins of hypervapotron [31]. Two testing loops were built: Hypervapotron Loop-I (HVL-I) and Pressure Water Hypervapotron Loop-II (PWHL-II), facilities are in the figure 24. Both the Hypervapotron design with grooves and the one with triangular fins were tested to examine the differences in vortex creation and heat flux values. Vortex formation was measured by Particle Image Velocimetry (PIV) and high-speed photography (HSP) techniques. In addition, heat transfer on the surface of grooves and triangular fins was observed and measured with the Planar Laser-Induced Fluorescence (PLIF).

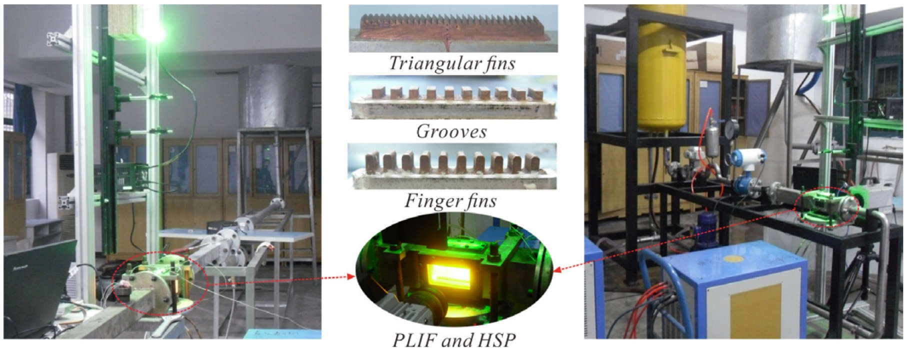

Figure 24: Hypervapotron Loop-I and Pressure Water Hypervapotron Loop-II

Hypervapotron Loop-I (HVL-I) has been set up to simulate the operating conditions of an ITER-like device with one side heating and water pressure 0.3-3 MPa. Pressure Water Hypervapotron Loop-II (PWHL-II) simulates the high heat flux parameters of divertor first wall and neutral beam injector components with geometries based on the MAST and the EAST hypervapotron at full scale. Heating by electromagnetic induction can provide input heat flux 1-10 MW.m^{-2}. However, because the heat resistance of the thermal insulation between the fins and grooves and the channel body is limited, the maximum input heat flux is set to 5 MW.m^{-2}. The Figure 25(a) shows greyscale PLIF images of hypervapotron grooves in case of heat flux 4.56 MW.m^{-2}, the figure 25(b) shows averaged temperature field for the exact measurement. Bubble and vortex characteristics are clearly heavily dependent on the internal geometry, flow conditions and input heat flux. The primary heat transfer mechanism of hypervapotron is the latent heat evaporation: the percentage of wall heat flux going into vapour production is almost 70%. Therefore, the high bubble departure frequency and smaller bubble sizes benefit the overall thermal performance.

The Figure 28 shows the results of the PIV and HSP technique, vortex creation and interaction with the free-stream flow. With the increasing streamflow velocity, the vortex rotary speed and breakup events increase, the central location of the vortex accelerates upward to half of the fins, and the vortex becomes more unstable, which might be attributed to the effects of the radial momentum of the stream and spin momentum of the vortex. When the input heat flux increases, the bubble density increases locally, and the upward acceleration increases.

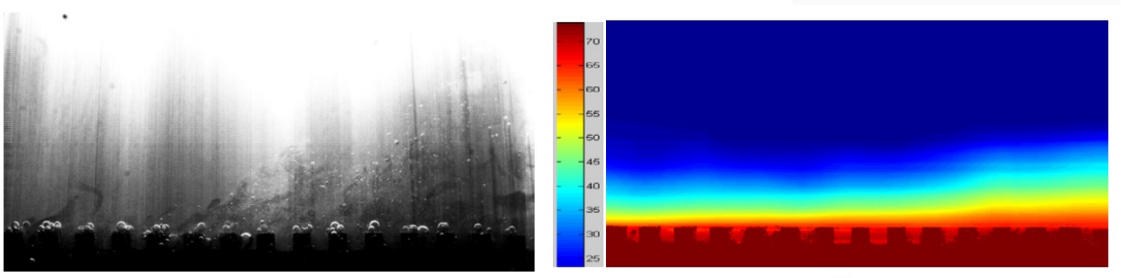

(a) (b)

Figure 25: Results of PLIF and temperature field for the heat flux 4.56 MW.m^{-2}

The second part of this article is focused on numerical simulation with the same parameters as the experimental part. PIV measurements resulted in similar vortex formations as the CFD model. Figure 26 represents the results of heat flux calculation and measurements for the grooves (a) and triangular fins (b) geometry. In similar conditions, grooves can achieve 20-70 % higher heat flux than triangular fins.

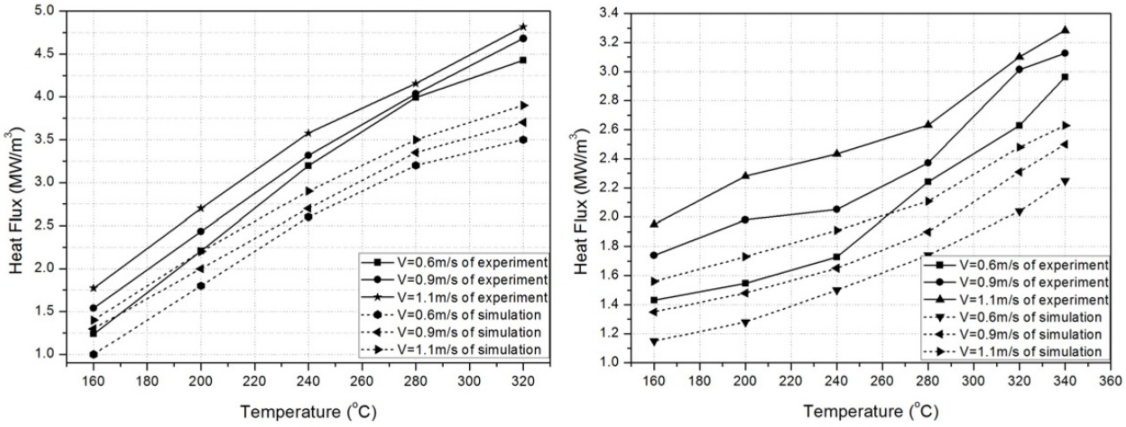

(a) (b)

Figure 26: Comparing the heat flux of calculation results and measured values for grooves (a) and triangular fins (b)

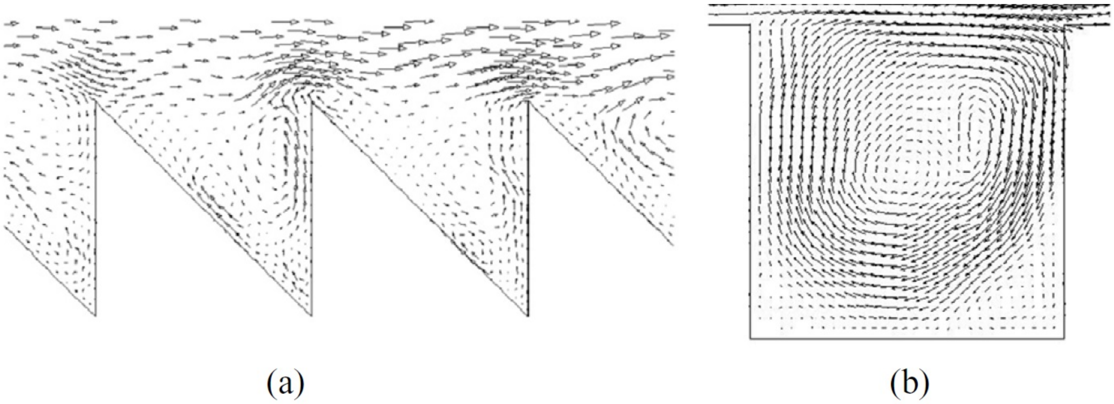

Figure 27: Velocity vector and vortex formation near the triangular fins and grooves (simulation)

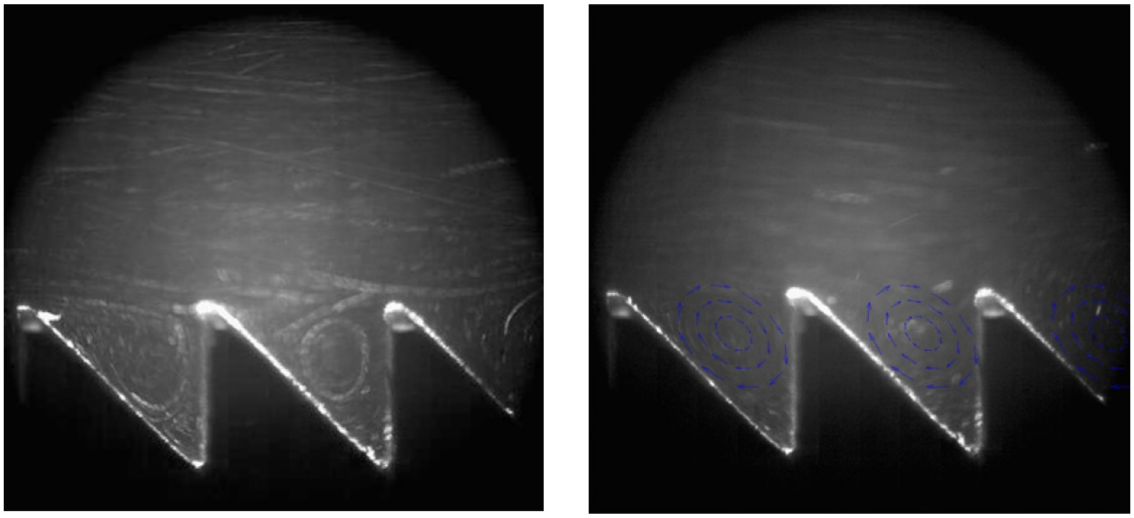

Figure 28: Vortex formation between triangular fins (experiment)

5.3 Institute for Plasma Research, India, 2020

Indian Test Facility (INTF) is being built to experiment with neutral beams with peak power densities up to 66 $MW.m^{-2}$. Hypervapotron elements are considered thermal target systems building blocks of the First Calorimeter and Second Calorimeter. The scheme of calorimeters position is shown in figure 29(a). This paper [32] focused on the evaluation of the heat transfer performance of hypervapotron by three approaches:

- 3D FEA ANSYS model using Empirical correlations available in the literature
- 2D CFD in ANSYS CFX
- High heat flux experiments on hypervapotron element

Calorimeters are used to measure the energies of the accelerated beam at 6 m and 21 m distance from the beam source. Calorimeters consists of V-shaped panels made from a stack of hypervapotron elements. These elements are designed to withstand the high power densities of the beam. Hypervapotron elements need to be oriented to the beam at a certain angle to lower the abovementioned power densities. Calculation of this angle is the aim of this paper. The safe operating temperature limit of hypervapotron material (CuCrZr) is 350 °C. The cooling water pressure is 1 MPa, andthe inlet temperature is 40 °C. This test has two different water velocities: 4.4 and 2.2 $m.s^{-1}$. (Flow rates of 60 and 30 litres per minute.)

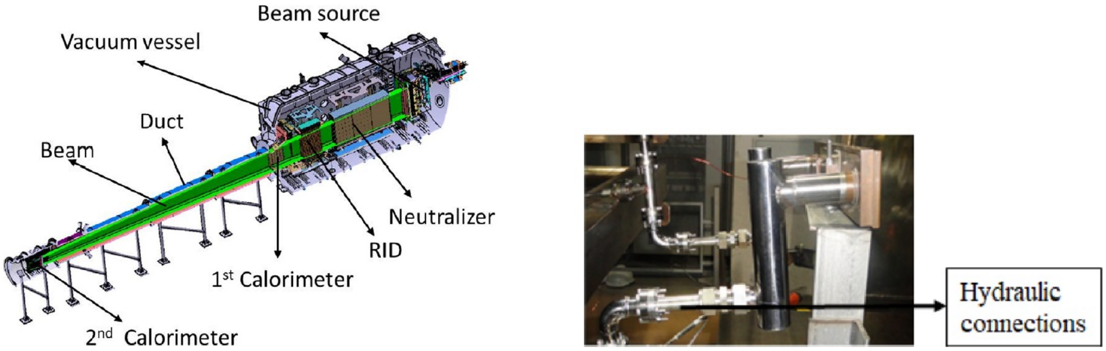

(a) Indian Test Facility (INTF)

(b) Hypervapotron inside vacuum chamber

Figure 29: The Experimental Setup

The primary purpose of the experimental part of this study is to validate the CFD simulation results. Hypervapotron channel is mounted inside the vacuum chamber. The heat source is provided by rastering the electron beams for a localised area. The beam target area is 80x65 mm^2, covering 13 fins of the hypervapotron. The test facility is equipped with an electron gun with a maximum beam power of 200 kW and the ability to raster at 10 kHz, covering the surface up to 1 m x 1 m. The beam power used in this test range from 15 to 60 kW, generating beam flux 2-12 $MW.m^{-2}$. Material temperature is measured by IR camera and thermocouples. IR calibration is performed to find the correct emissivity value for the IR temperature measurement.

A copper alloy block of the same grade as the mockup with an identical surface finish is used for this calibration. The temperature of the wet wall is estimated from the numerical simulations, since there are no diagnostics installed. A schematic of the experimental setup is shown in figure 30(a). Figure 30(b) shows the dimensions of the hypervapotron channel used in this test.

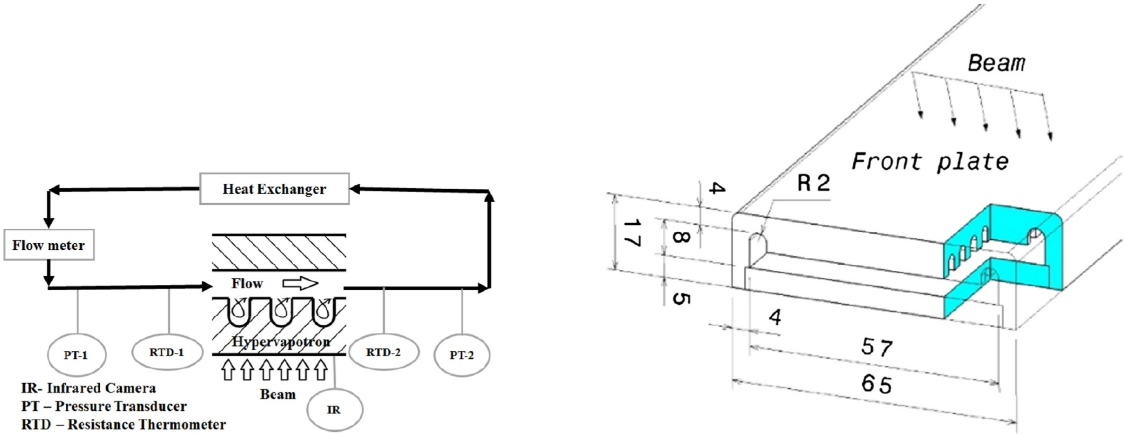

(a) Experimental loop

(b) Cut section of Hypervapotron

Figure 30: The Indian Test Facility

Figure 31 compares simulations and experimental results for coolant velocities of 4.4 and 2.2 m.s^{-1}. In the single-phase heat transfer regime, results are in good agreement (within 10 %). The two-phase regime results deviate gradually from the ONB (Onset of Nucleate Boiling). ONB starts near 3.6 and 5.5 MW.m^{-2} (2.2 and 4.4 m.s^{-1}). Higher heat flux results in higher temperature deviation. 3D FEA ANSYS model using Empirical correlations is nearer to experimental results. The result of the conducted experiment is that: hypervapotron channel, in the conditions of this facility, can provide heat flux of 10 and 12 MW.m^{-2} (2.2 and 4.4 m.s^{-1}) and keep the surface temperatures falling below the material limit of 350 °C.

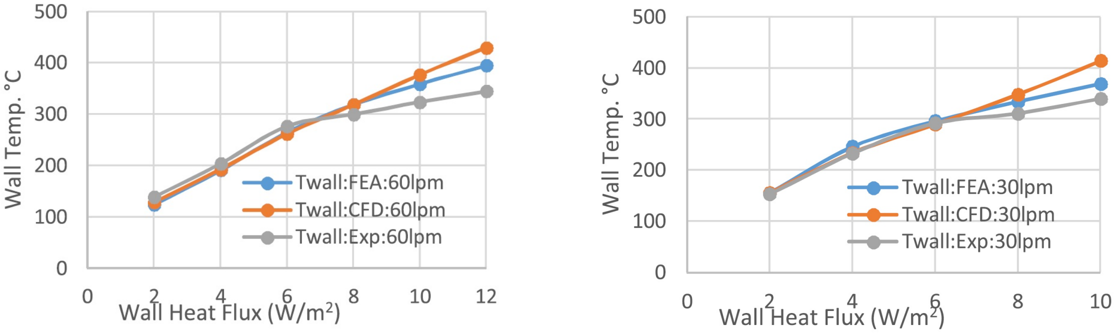

(a) 4.4 m.s^{-1}, 60 liters per minute

(b) 2.2 m.s^{-1}, 30 liters per minute

Figure 31: The Experimental Data compared with FEA ANSYS and CFD ANSYS CFX

6 Numerical Studies of Hypervapotron

6.1 Milnes Thesis, ANSYS CFX, 2010

Milnes thesis [33] is a complex analysis of subcooled boiling in hypervapotron channel. There are two chapters in Milnes thesis beneficial for this work: 2D analysis of flow patterns and temperature distributions in hypervapotron channels of different shapes and dimensions and complex 3D analysis of hypervapotron based on the same boundary conditions as this thesis.

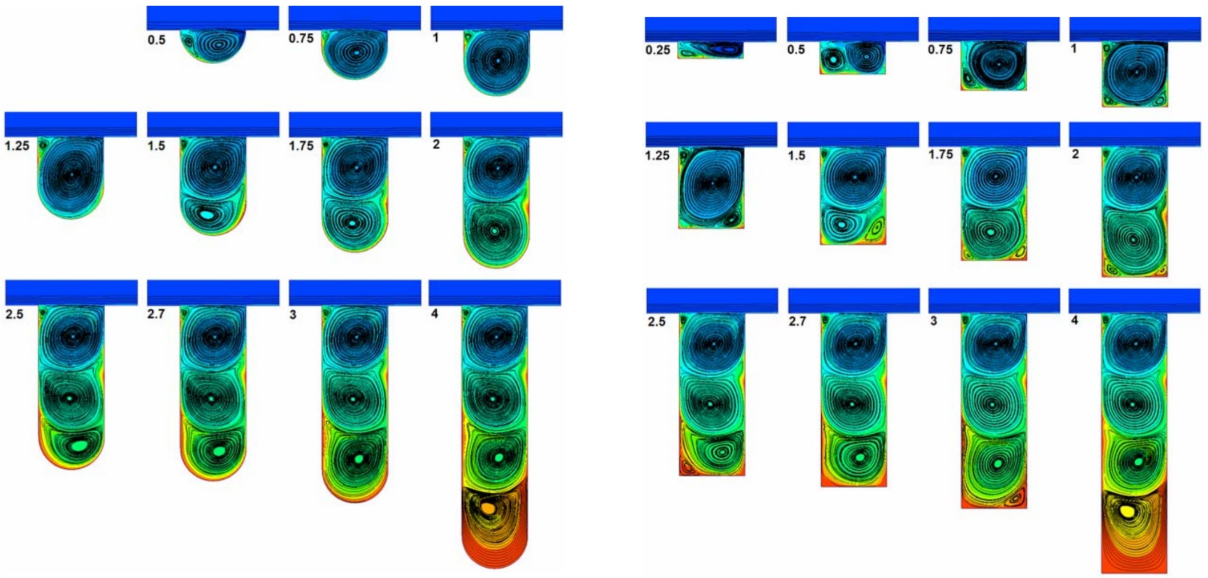

(a) Round Hypervapotron [33]

(b) Rectangular Hypervaporon [34]

Figure 32: Flow Patterns and Fluid Temperature Distributions in Hypervapotron (Milnes)

The Figure 32 shows the results for variable aspect ratio (depth divided by width of channel) for rectangular and round cavities. The presence of one flow vortex inside cavity is clearly resulting in the lowest temperature maximum, results are corresponding with experimental measurements obtained by particle image velocimetry (PIV) mentioned in Chapter 4.3. Milnes analysis concluded: 1.25 is the optimal aspect ratio of round hypervapotron channel design. Additional vortexes result in lower heat removal, since the velocity of vortex rotation is linearly decreasing with the number of present vortexes. From this point of view, examined 3D geometry (3x4 mm) does have the optimal parameters.

The second part of Milnes thesis examines 4 different hypervapotron 3D geometries, 2 are rectangular and 2 are round shaped. The 3x4 round "Boxscraper" match the geometry used in my numerical analysis, therefore Milnes model and results described in detail. Milnes successfully validated his model by experimental data [35], the following work by Pitoňák [36], Písek [37] and my thesis are based on Milnes research. Milnes later publicated results of his thesis in article *Computational modeling of the HyperVapotron cooling technique* [38].

Turbulence Numerics	First Order
Advection Scheme	High Resolution
Multiphase Control	Volume Fraction Coupling
Water Morphology	Continuous Fluid
Vapour Morphology	Dispersed Fluid
Turbulence Model (Water)	SST $k-\omega$
Turbulence Model (Vapour)	Dispersed Phase Zero Equation
Drag Force	Schiller Naumann
Lift Force	0.5
Turbulence Transfer	Sato Enhanced Eddy Viscosity
Virtual Mass Force	not considered
Wall Lubrication Force	not considered
Turbulent Dispersion Force	Favre Average Drag Force
Wall Boiling Model	RPI Model
Bubble Departure Model	Tolubinski Kostanchuk
Bubble Detachment Frequency	Situ (limited to 412-881 Hz range)
Nucleation Site Density	Lemmert Chawla
Max. Area Fraction of Bubble Influence	0.95
Bubble Diameter Influence Factor	2
Bulk Bubble Diameter	Anglart and Nylund
Fixed y+	250
Quenching Heat Transfer Coefficient	Dell Valle Kenning
Heat Transfer	Ranz Marshall

Table 2: Milnes Thesis Settings (ANSYS CFX)

Milnes mesh is based on a hexahedral element type, it is shown in the Figure 33(a). This mesh represents a template for the following works by Písek and Pitoňák. Table 2 shows the ANSYS CFX setting used for a solution. Most of the settings are set on default values, a bubble departure diameter approximation was changed to Tolubinski-Kostanchuk correlation and the Situ correlation for a bubble detachment frequency was customised. Situ correlation was limited to range 412-881 Hz to match the conditions in hypervapotron. Milnes work represents the foundation for settings used in numerical part of this thesis.

Figure 33(b) shows the liquid velocity streamlines. There is a visible difference between the simplified 2D vortex simulation a the 3D model. A narrow side groove parralel to a flow direction evidently affects the rotation of fluid between the fins of hypervapotron. Disturbing the typical one-vortex rotation (seen in 2D) between fins visibly changes the behaviour of vapour and heat transfer. The streamline velocity scale shows how slower is the vortex rotation of fluid between fins compared to the main flow. Important note: inlet fluid flow directions of Milnes and this thesis are mirror-inverted.

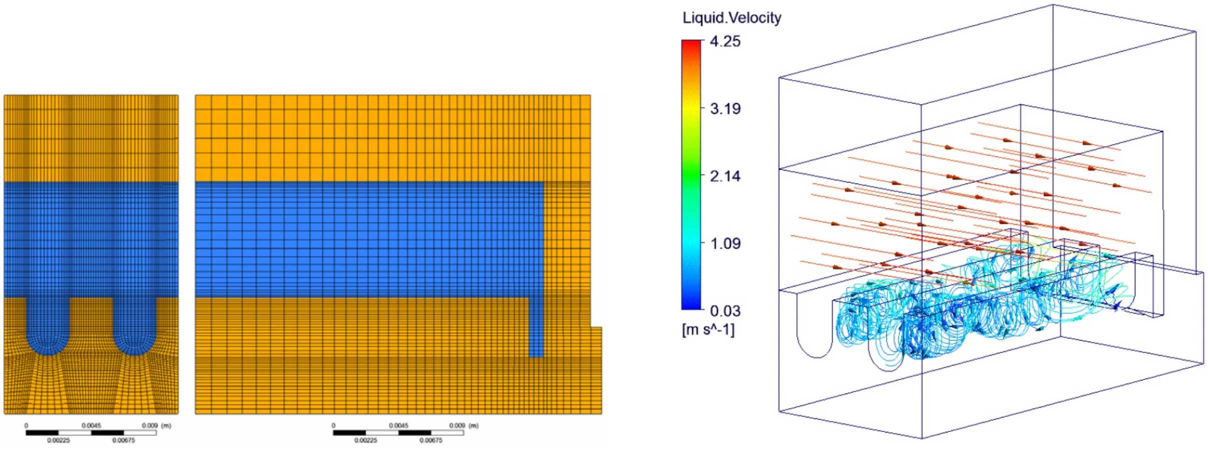

(a) Milnes Mesh (b) Liquid Velocity Streamlines

Figure 33: Milnes Model

The Figure 34 shows final Milnes results: vapour volume fraction in hypervapotron channel and temperature profile of a solid hypervapotron body. Milnes model of the solid body is slightly raised on the right side (Fig. 34) to more precisely match temperature distribution in solid body used for validation experiment. Validation experiment used by Milnes and the following thesis is described in detail in The Chapter 7.1.11. Maximal volume fraction of vapour reached 0.1 in the center between fins, where detached bubbles of vapour are coupling. Although Milnes model is based on simplified VOF (volume of fluid) model, behaviour of vapour bubbles is successfully simulated. Using more advanced Eulerian approach to simulate individual bubbles in fluid is one of the objectives of this thesis. Milnes model results are in agreement with experimental data and predicted behaviour of subcooled boiling.

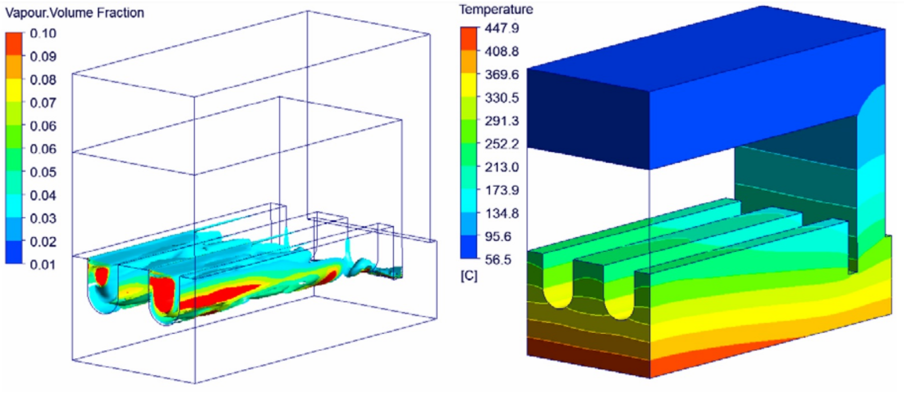

Figure 34: The Vapour Volume Fraction and The Temperature Distribution (10 MW.m^{-2}, Milnes)

Conclusion of Milnes thesis: ***Subcooled boiling in hypervapotron channel was successfully simulated using ANSYS CFX software, results were validated by experimental data.***

6.2 Domalapallya, Subba, Star CCM+, 2014

This paper [39] by the authors Phani Domalapallya and Fabio Subba is focused on comparing the two computational boiling models. At first, the Rohsenow and the transition boiling models are compared on the geometry of a 4x3 hypervapotron further described in Section 7.1.1. The Rohsenow boiling model can model both nucleate and film boiling: the transition model can model nucleate and transition boiling. Both models were tested using the commercial CFD software STAR CCM+, with the Volume of Fluid (VOF) approach for the multiphase flow analysis.

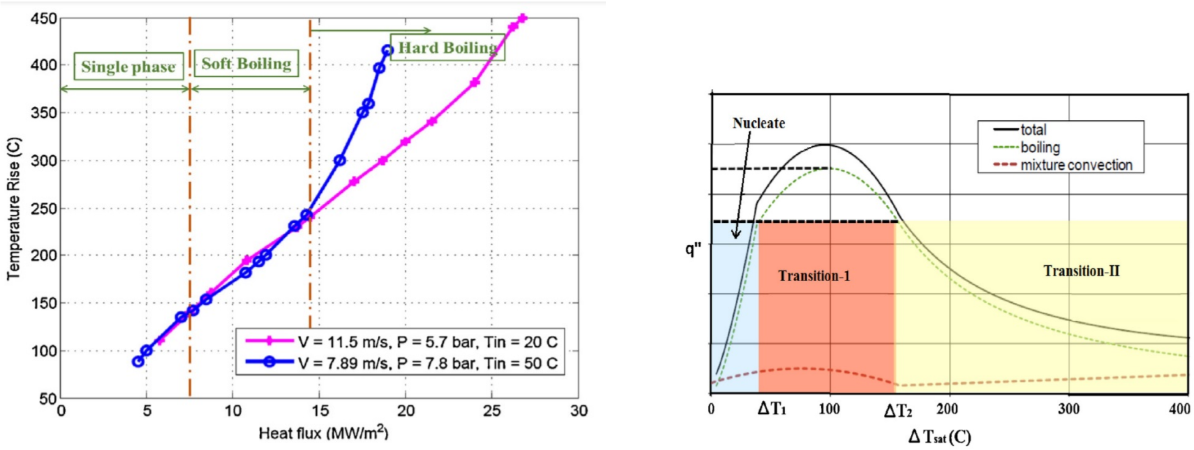

(a) Heat Flux vs Excess Temperature

(b) Experimental Data Showing Different Boiling Regimes

Figure 35: The Boiling Regimes

Rohsenow Boiling Model

This model consists of the three different correlations for the three regions shown in Figure 35(b), trying to accurately capture the nucleate region and the two transition regions.

$$q_{boiling}(\Delta T) = q_{max} S \phi \left(\frac{\Delta T}{\Delta T_1}\right)^{k_i} \qquad 0 \leq \Delta T \leq \Delta T_1 \tag{58}$$

$$q_{boiling}(\Delta T) = q_{max} S \left(1 - 4(1-\phi)\left(\frac{\Delta T - \Delta T_{max}}{\Delta T_2 - \Delta T_1}\right)^2\right) \qquad \Delta T_1 \leq \Delta T \leq \Delta T_2 \tag{59}$$

$$q_{boiling}(\Delta T) = q_{max} S \phi \left(\frac{\Delta T - \Delta T_1}{\Delta T_2 - \Delta T_1}\right)^{-k_2} \qquad \Delta T_2 \leq \Delta T \tag{60}$$

The Transition Boiling Model

Both models are based on the similar set of equations: the $k - \varepsilon$ model solves the turbulent flow. The wall function of this model is set to handle y+ 30 near the wall.

C_{qw}	C_{ew}	$C_{HTC\,x\,area}$	$\alpha_{film\,boiling}$	η_p	S_{ct}
0.01	0.0125	$1 \cdot 10^6$	0.1	1	0.85

Table 3: Parameters Used in The Rohsenow Model

Q_{max}	C_{ew}	ϕ	K_1	K_2	ΔT_1	ΔT_2	η_p	S_{ct}
$9 \cdot 10^6$	0.0125	0.75	1.2	1.25	55	140	1	1

Table 4: Parameters Used in The Transition Model

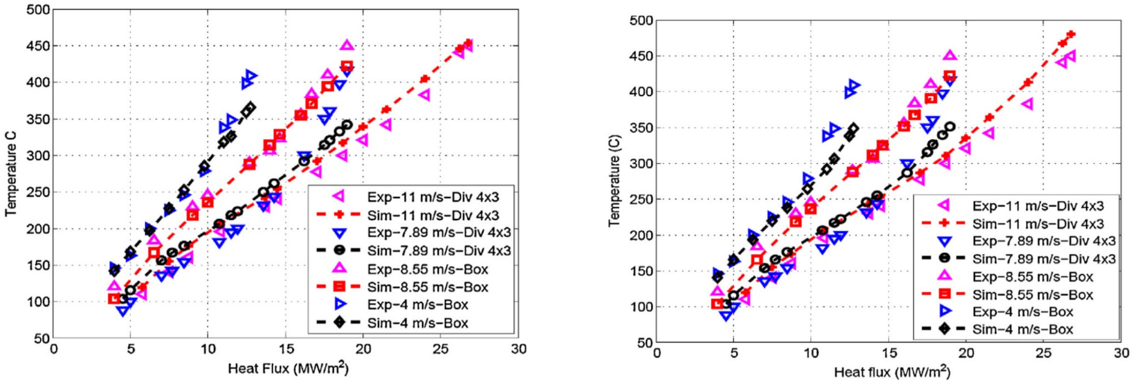

(a) The Rohsenow Model (b) The Transition Model

Figure 36: The Comparison of temperatures computed with Rohsenow and Transition model with the experimental data for different heat fluxes and inlet velocities

Although gravity and surface tension effects are included, the model takes advantage of the geometry symmetry. The velocity inlet of the cooling water is set to v_{in}=11 ms^{-1}, two heat fluxes at the verge of changing boiling regime (5.8 MWm^{-2}, 18.7 MWm^{-2}) are considered. The computational parameters are set to minimise the discrepancy between experimental and simulated data below 5%. The Figure 35(a) shows the typical experimental data. The results are divided into three regimes: a single-phase (forced convection) regime with a constant slope of the curve, a nucleate or soft boiling regime with a decreasing slope of the curve and a regime of hard boiling (increase in slope, more bubbles formed). The Figure 37 compares the Rohsenow model (a) and the Transition model (b) results with the experimental data. The simulations show an accurate correlation with the experimental results for all given inlet velocities and heat fluxes. The same grid was used for both the Rohsenow and the Transition model. The change in slope of the Rohsenow model is visible only while going from a no boiling to a nucleate boiling conditions, the second change in slope is not perceptible. The Transition model has an advantage in the variation of the free parameters which allows us to simulate the three boiling regimes by properly adjusting them. The Transition boiling model shows an accurate agreement with the experimental data for all given inlet velocity conditions and heat fluxes, showing both slope changes. In Figure 37, the data for 3x4 hypervapotron geometry (Section (7.1.1)) are accompanied by data for the Box scraper geometry [39].

The conclusion of this article is: *”Heat transfer in subcooled boiling conditions relevant for high heat flux application of fusion reactor are studied comparing Rohsenow and Transition boiling models, which are available in STARCCM+. The tests conducted using the Rohsenow model on Hypervapotron are very promising. Quantitatively, the discrepancies in temperatures reported for all the test cases are about 10 %. Qualitative features using this model are good till the nucleate boiling regime only. The tests conducted using the Transition boiling model on Hypervapotron are very promising, both quantitatively and qualitatively. The discrepancies reported for all the test cases are either similar or better in some cases than the Rohsenow model. This model gives us confidence in using commercial CFD codes for predicting the thermal performance of the Hypervapotron as these results also follow the qualitative shape of the experimental data [39].”*

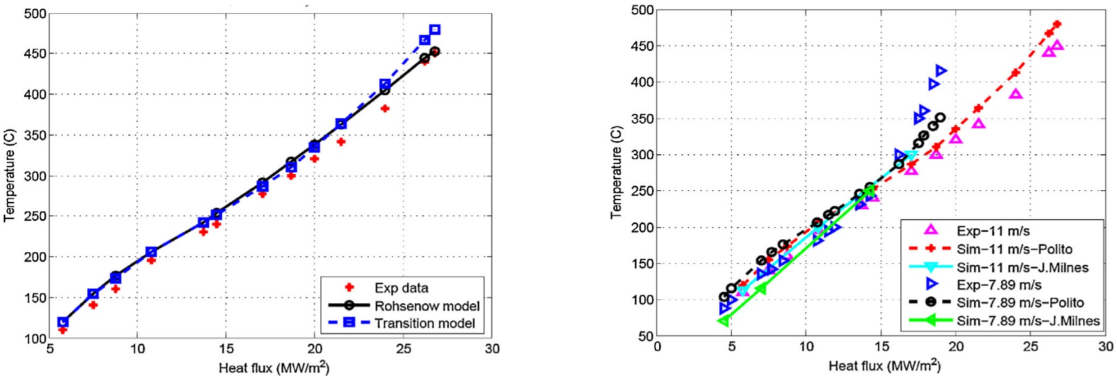

(a) Comparison of Rohsenow model and Transition boiling model with experimental data

(b) Comparison of data by Milnes and Transition boiling model with experimental data

Figure 37: Comparison of The Results

6.3 Písek Thesis, ANSYS Fluent, 2016

Písek thesis [37] is solving the same problem as the numerical part of this thesis, therefore its important to point out the differences of our solutions. Písek created his model in ANSYS Fluent software with $k-\varepsilon$ turbulence settings and non-equilibrium wall functions, used mesh consist of 170 000 hexahedral cells. Boundary conditions of inlet/outlet are identical to this thesis, described in detail in The Chapter 7.1.3. Wall flux boundary condition is varying from 4.5 to 12 MW/m^2. The Multiphase Eulerian RPI model was selected to simulate boiling. Písek considered 5 different variants of boiling model setting, the selected variant used for solution is described below (Tab. 5). Písek model was validated with data available from Milnes thesis [33].

Bubble Departure Diameter	Tolubinski-Kostanchuk
Bubble Diameter	$d_b = 0.00015m$
Interfacial Area Concentration	On
Breakage Kernel	Yao-Morel
Frequency of Bubble Departure	$f_{constant} = 412Hz$
Turbulent Dispersion	not considered
Heat Transfer Coefficient	Ranz-Marshall
Fixed Yplus Value	250

Table 5: Písek Thesis Settings (ANSYS Fluent)

The Figure 38(a) shows the boundary heat flux condition was not applied on the whole underneath wall. Heat flux is applied only on the part of the wall directly facing the cooling channel to match with Milnes results. The solid model temperatures measured on the side of hypervapotron body for different heat flux settings matched the experimental data. Unfortunatelly, validation data were misinterpreted and comparison of Figures 38(a) and 34 clearly shows the difference in temperature profile. Maximal solid temperature for the 10 MW/m^2 heat flux in Milnes model is 447.9 °C, Písek model maximum is only 412.6 °C. This inaccuracy is most likely caused by the inaccurate solid material properties setting, more explained in Chapter 7.1.2.

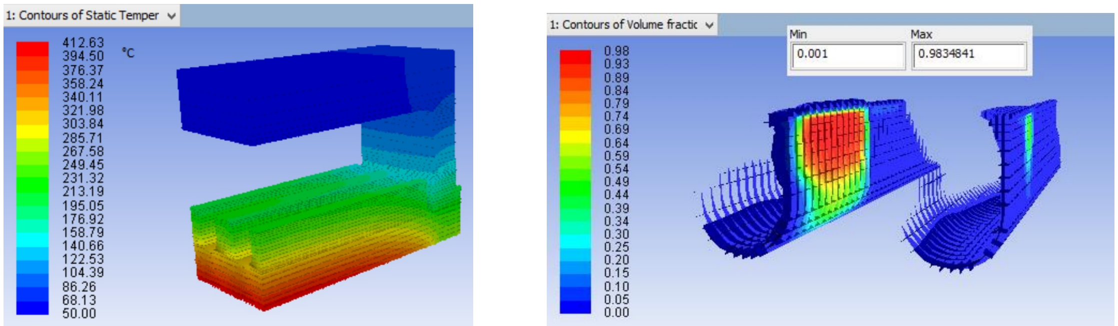

Min 0.001

Max 0.9834841

(a) Solid Temperature Contours (b) Vapour Volume Fraction (10 MW/m^2, Písek)

Figure 38: Písek Thesis Results

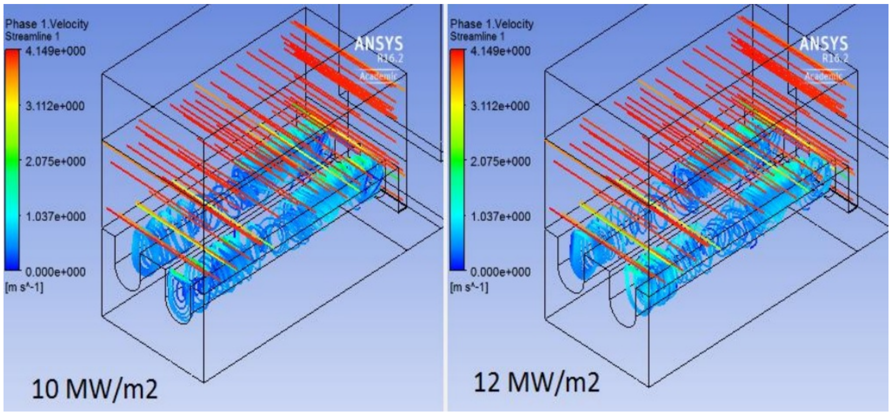

Figure 39: The Velocity Streamline (10/12 MW.m^{-2}, Písek)

The results of Písek solution are shown in Figures 38, 39 and 40. Velocity streamline view (Figure 39) shows the velocity in main stream (4 m/s) and lower velocity of circulating fluid between the fins (around 1 m/s). Contours of the vapour volume fractions show higher values on the second fin, caused by the increase of main stream temperature. Maximum of vapour volume fraction is around 0.98, indicating the boiling crisis: unfavorable phenomenon in the case of hypervapotron.

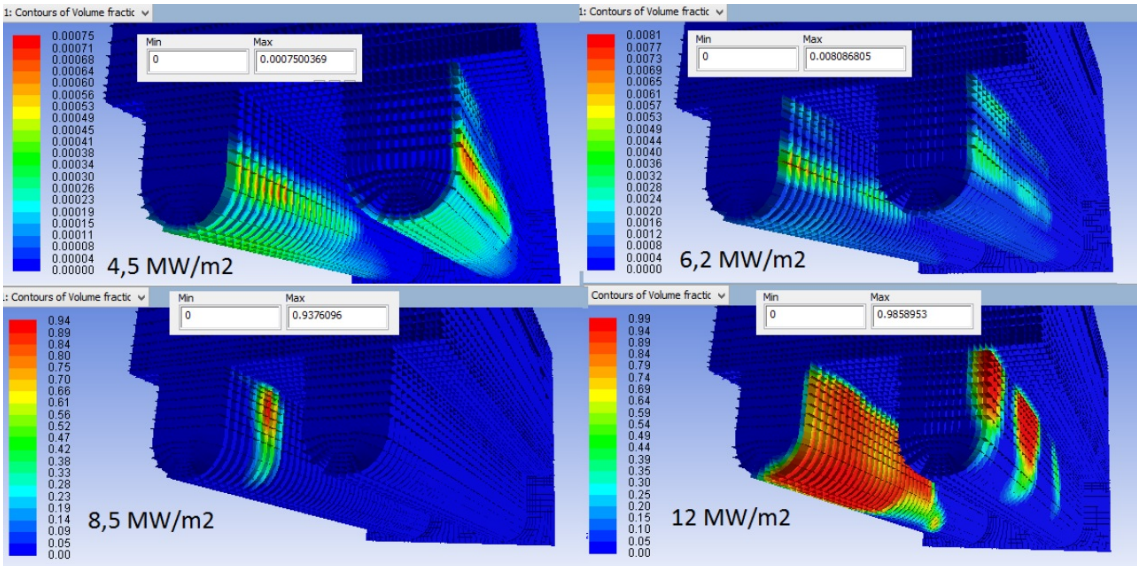
Min 0 Max 0.0007500369

Min 0 Max 0.008086805

Min 0 Max 0.9376096

Min 0 Max 0.9858953

Figure 40: The Contours of Vapour Volume Fraction (10 MW.m^{-2}, Písek)

Conclusion of Písek thesis: ***ANSYS Fluent is at the moment not able to fully simulate the subcooled boiling regime in hypervapotron conditions.*** Písek thesis and its conclusions were based on version ANSYS Fluent 16.2.

6.4 Pitoňák Thesis, ANSYS CFX, 2017

The numerical part of Pitoňák thesis [36] is based on the calculations in ANSYS CFX software. Pitoňák took over the mesh created by Václav Písek to show the differences in ANSYS Fluent and ANSYS CFX solution. The Settings of Pitoňák model are based on the previously mentioned Milnes thesis. Boundary conditions match Písek thesis, solution was calculated for heat fluxes of 2, 6, 10 and 12 MW/m^2. The Table 6 summarise the Pitoňák model settings. Majority of parameters are part of default CFX, but some correlations (Tolubinski Kostanchuk, Situ, Anglart Nylund) were added to CFX using user-defined functions.

Turbulence Numerics	First Order
Multiphase Control	Volume Fraction Coupling
Water Morphology	Continuous Fluid
Vapour Morphology	Dispersed Fluid
Turbulence Model (Water)	SST $k-\omega$
Turbulence Model (Vapour)	Dispersed Phase Zero Equation
Drag Force	Schiller Naumann
Lift Force	0.5
Turbulence Transfer	Sato Enhanced Eddy Viscosity
Virtual Mass Force	not considered
Wall Lubrication Force	not considered
Turbulent Dispersion Force	Favre Average Drag Force
Wall Boiling Model	RPI Model
Bubble Departure Model	Tolubinski Kostanchuk
Bubble Detachment Frequency	Situ (limited to 412-881 Hz range)
Nucleation Site Density	Lemmert Chawla
Max. Area Fraction of Bubble Influence	0.95
Fixed y+	250
Quenching Heat Transfer Coefficient	Dell Valle Kenning
Heat Transfer	Nusselt Number = 2

Table 6: Pitoňák Thesis Settings (ANSYS CFX)

The second part of Pitoňák thesis is focused on design and simulation of hypervapotron cooling channel for BESTH device. The BESTH (Beryllium Sample Thermal Testing) in located in ÚJV Řež, a.s. resarch facility, built to test fatigue of beryllium samples. The samples can be exposed to heat flux up to 0.9 MW/m^2 provided by joule heating graphite element. The graphite conductor is surrounded by protective helium atmosphere. One fatigue test consist of 12 thousand 300-second cycles of heating up the sample to simulate the conditions in fusion reactor. Inlet coolant parameters are 6 bar, 1 m/s, 100 °C, heat flux is set to 0.9 MW/m^2. The BESTH cooling channel was created by the connection of 19 hypervapotron mesh models with total number of 4.47 million cells. This complex solution was solved by a parallel processing on Czech Technical University servers. Results of the BESTH hypervapotron simulation are shown in the Figure 42.

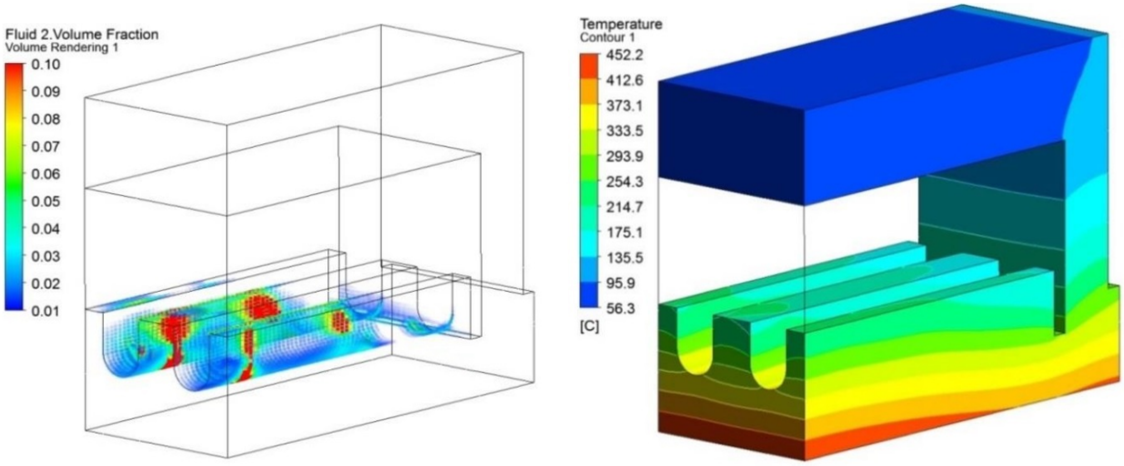

Figure 41: Vapour Volume Fraction and Temperature Distribution (10 MW.m^{-2}, Pitoňák)

The thesis results were validated by the same experimental data as Milnes, Písek, and this thesis (Chapter 7.1.11). Figure 41 shows vapour volume fraction and temperature profile in hypervapotron. This result can be easily compared with results of Milnes thesis (Figure 34). Diverse temperature profile is most probably caused by the difference in solid CuCrZr thermal conductivity setting, this problem is further explained in Chapter 7.1.2. Vapour volume fraction contour in Figure 41 is result of the simulation with Cole bubble detachment frequency correlation. Pitoňák included Cole correlation to match Milnes setting and compare with his results. In the case of Pitoňák model, Situ correlation for bubble detachment frequency provided much better results than Cole correlation, matching the experimental data. Switching from Cole to Situ correlation caused decrease of solid body temperature by 30 °C (10 MW/m^2 heat flux).

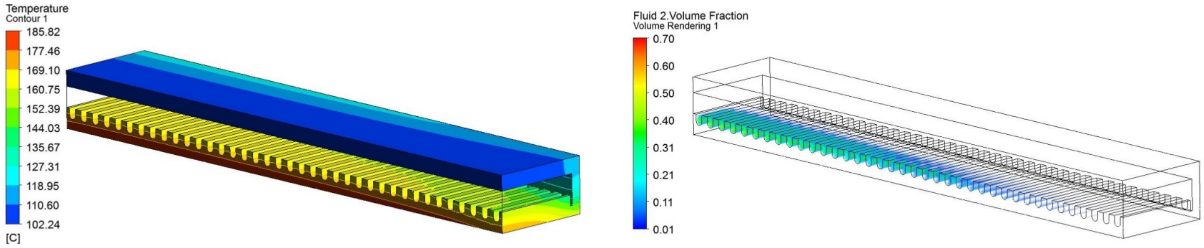

Figure 42: Vapour Volume Fraction and Temperature Distribution (BESTH, Pitoňák)

Conclusion of Pitoňák thesis: ***ANSYS CFX is able to simulate the subcooled boiling regime in hypervapotron conditions. Validated CFX model was used to simulate conditions in BESTH device.***

6.5 Gleitz Thesis, Star CCM+, 2022

Gleitz PhD thesis [40] consist of two main parts: the numerical analysis of subcooled boiling in hypervapotron (Star CCM+ software) and the design of experimental loop. The experimental loop will be used to validate numerical results and help better understanding of hypervapotron physics, since there are only a few reliable experimental results available at the moment. In the recent time, the Gleitz work is not finished yet, but some results were publicated and shared directly for the purpose of this thesis.

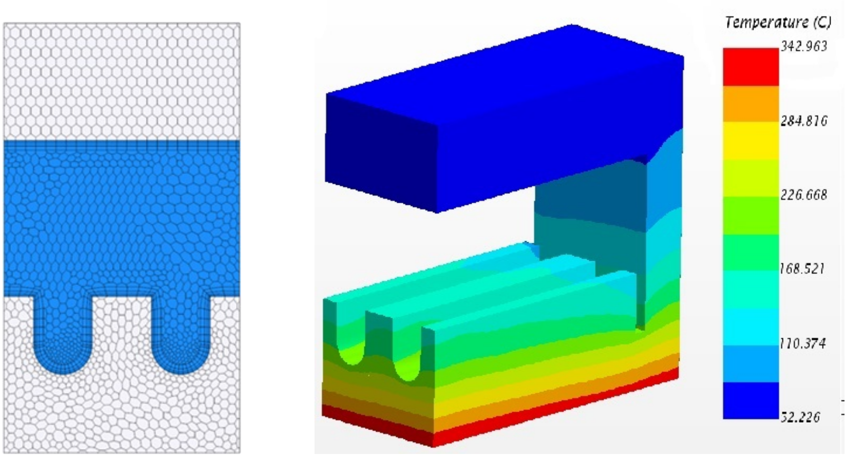

(a) Polyhedra Mesh (b) Gleitz Temperature Profile

Figure 43: Gleitz Mesh and Solid temperature Distribution, 10 MW.m^{-2}

Gleitz numerical anylysis is based on Rohsenow boiling model, previously mentioned and described in Chapter 6.2. Early Gleitz solution included the same mesh as Písek thesis, polyhedra mesh was then implemented to improve the convergence of simulation. The used polyhedra mesh is visualised in the Figure 43. The Rosenhow boiling model is based on Equation (61). The adjustable parameters were taken from Domalapallya a Subba article. Figure 44 shows the vapour volume fraction for the 10 MW/m^2 heat flux. Results of parametric simulation considering various heat fluxes and inlet velocities are shown in the Figure 45. The dashed line represents the velocity 4 m/s^{-1}, boundary condition used in the numerical part of this thesis and other previous works. Gleitz results shows this velocity is optimal value, considering the minimal temperature drop for higher velocities on the same heat flux.

$$q_{bw} = \mu_l h_{lat} \sqrt{\frac{g(\rho_l - \rho_v)}{\sigma}} \left(\frac{c_{Pl}(T_w - T_{sat})}{c_{qw} h_{lat} Pr_l^{np}} \right) \tag{61}$$

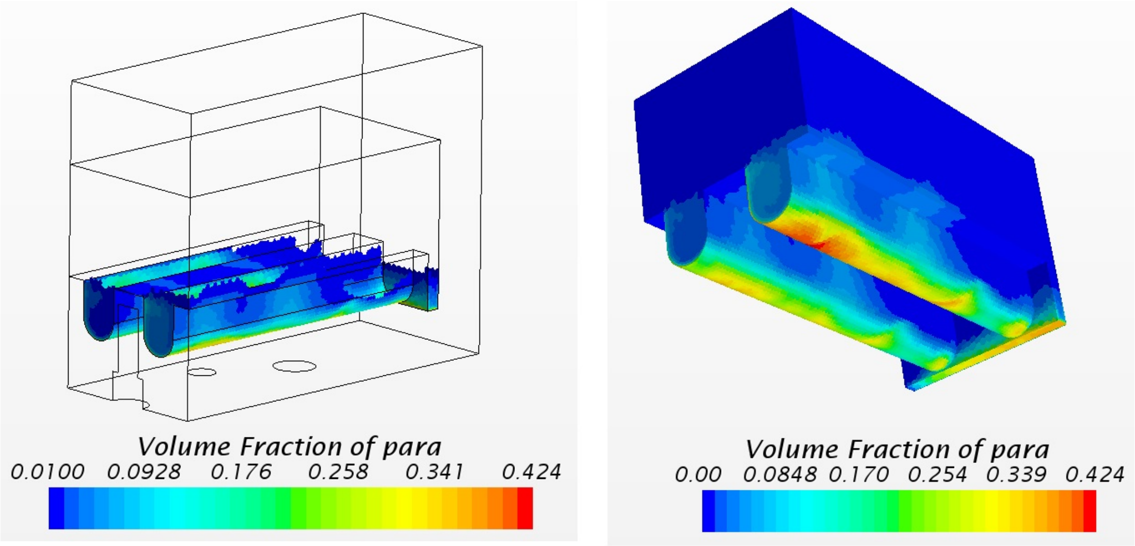

Figure 44: Gleitz Steam Volume Fraction, 10 MW.m^{-2}

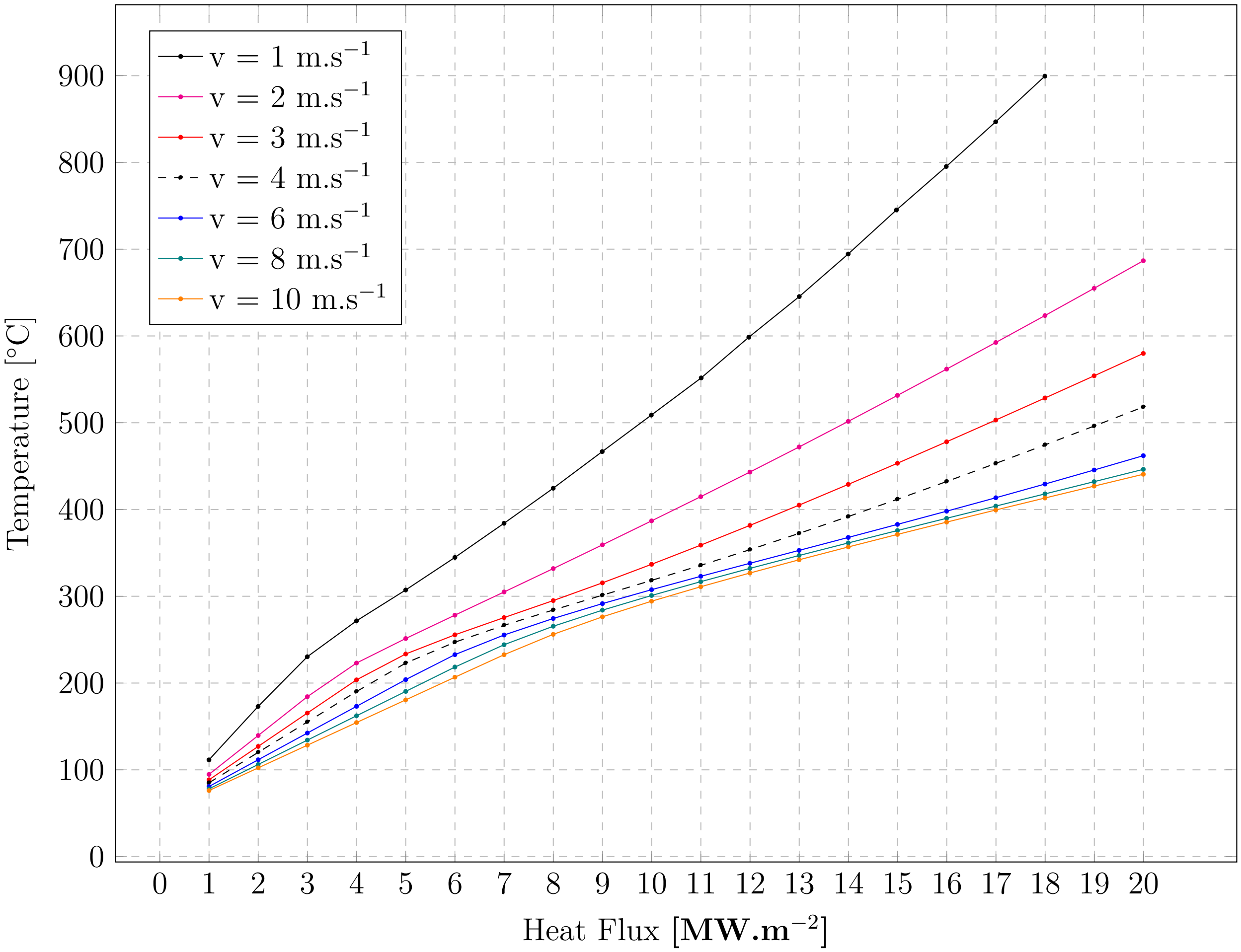

Figure 45: Gleitz Results

Part II
Practical Part

7 Numerical Part

The numerical part of this thesis describes the simulation of subcooled boiling in hypervapotron channel using ANSYS Fluent software. The following chapters contain description of used geometry, mesh, multiphase and viscous settings and results of simulation. The results are compared with experimental data and other numerical analysis mentioned in the previous chapter to evaluate quality of simulation.

7.1 Model

7.1.1 Geometry

The geometry and the dimensions of the hypervapotron channel used for the numerical simulation is shown in the Figure 46. This hypervapotron geometry was already used in the works of Milnes, Gleitz, Pitoňák and Písek, therefore it is possible to compare our results. Above all, there are experimental data measured on this geometry so the CFD simulation results can be validated. The experimental results and validation process are described in the Chapter 7.1.11. Used channel design is often reffered to as the "Box Scraper" hypervapotron.

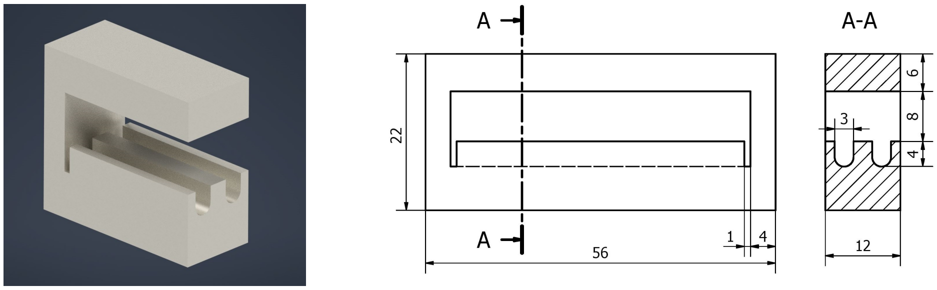

(a) Hypervapotron (one half)

(b) Dimensions of The Hypervapotron

Figure 46: The Geometry of The Hypervapotron Sample

The symmetry of the model was taken into account to reduce number of mesh cells and computational time needed to run the simulation. There is one visible difference between the geometry used in this thesis and Milnes model: small block of solid added on the outside wall of channel. This modification was introduced by Milnes to match temperature profile of a solid in the two-channel hypervapotron geometry used in validation experiment (Chapter 7.1.11). The simulation results of solution described in Chapter 7.2.5 proved the effect of this modification is minor, therefore it was neglected and geometry was simplified. Temperature profile on the solid/fluid interface is the crucial measure for the subcooled boiling simulation.

7.1.2 Material Properties

Solid material - CuCrZr

Si [%]	Cr [%]	Zr [%]	Cu [%]	Fe [%]
≤ 0.10	0.10-1.20	0.03-0.3	Rest	≤ 0.08

Table 7: CuCrZr Chemical Composition (CuCr1Zr) [41]

The most important solid material properties for thermohydraulic analysis are thermal conductivity and specific heat in the range of hypervapotron operating temperatures. Unfortunatelly, other hypervapotron studies do not use the same material properties. There are some experiments on CuCrZr that can provide accurate material data, but this thesis has objective to compare results with previous calculations. Therefore, solid material properties are chosen to match other thesis. In the case of thermal conductivity: Milnes and Pitoňák use similar values (345 and 335 W/m.K), but Písek works with temperature-dependent conductivity on much higher values (365 W/m.K at 300 °C). According to citations, Písek is using parameters of pure copper in his model. From this point of view, Písek model should not be able to give same results as the other analysis. Pitoňák thesis conclusion says: increasing thermal conductivity from 330 to 335 W/m.K resulted in 3 °C decrease of maximal solid temperature. For this model, thermal conductivity is set to 340 W/m.K to match Milnes and Pitoňák results. According to available data and articles, CuCrZr alloy properties are also dependend on applied material treatment (annealed, hardened), see Figure 47. Important note: data in Figure 47 do not share the same temperature unit. Properties of solid body in this thesis are set to constant values, not temperature-dependent [41] [42] [43].

Density [kg/m^3]	Specific Heat [J/kg.K]	Thermal Conductivity [W/m.K]
8910	390	340

Table 8: CuCrZr Properties

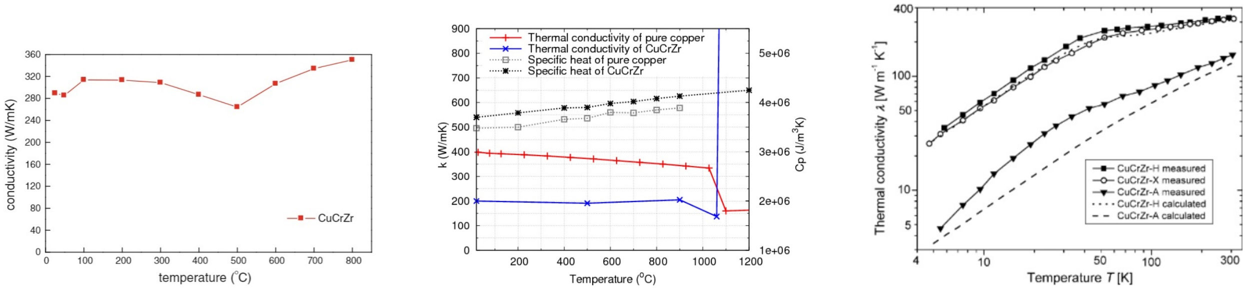

(a) CuCrZr [41]

(b) CuCrZr vs pure Cu [42]

(c) Annealed(A)/Hardened(H) [43]

Figure 47: Thermal Conductivity and Specific Heat

Fluid material - Water

The density, specific heat, thermal conductivity and viscosity of water are defined by linear temperature-dependent functions. Reference temperature is set to constant value of the saturated vapour temperature. The latent heat is equal to the difference of vapour and liquid state enthalpy. Saturated vapour temperature, enthalpies and latent heat were calculated using the following Coolprop Python code:

```python
from CoolProp.CoolProp import PropsSI

# Saturated vapour temperature of Water at 6 bar in J/kg
print(CP.PropsSI('T','P',600000,'Q',1,'Water')-273.15)

# Saturated vapour enthalpy of Water at 6 bar in J/kg
H_V = PropsSI('H','P',600000,'Q',1,'Water')
print(H_V)

# Saturated liquid enthalpy of Water at 6 bar in J/kg
H_L = PropsSI('H','P',600000,'Q',0,'Water')
print(H_L)

# Latent heat of vaporization of Water at 6 bar in J/kg
print(H_V - H_L)
```

output:

T_{sat}	**158.83**	°C
h_{vapour}	2 756 142	$J.kg^{-1}$
h_{liquid}	670 377	$J.kg^{-1}$
Latent Heat	2 085 765	$J.kg^{-1}$

Table 9: The Water Properties

Vapour	49 665 678.84	$J.kmol^{-1}$
Liquid	12 080 193.54	$J.kmol^{-1}$

Table 10: The Standard State Enthalpy

ANSYS Fluent material properties require standard state enthalpy in the unit of J/Kmol. Input parameters after unit transfer (multiplication by molecular weight of H_2O) are shown in Table 10.

NOTE: ANSYS Fluent unit of standard state enthalpy (mole specific energy) is defined as J/kgmol, this is probably a typo in the software taking into account the physical meaning. The correct unit is J/kmol.

7.1.3 Boundary Conditions

Velocity Inlet	Velocity	4 [$m.s^{-1}$]
	Turbulent Intensity	5 [%]
	Hydraulic Diameter	10.888 [mm]
	Temperature	50 [°C]
	Vapour Volume Fraction	0
Pressure Outlet	Pressure	600 000 [Pa]

Table 11: Boundary Conditions

For the turbulence boundary conditions: turbulence intensity is set on the default value of 5 %, hydraulic diameter on an inlet is calculated in equation (62). A represents inlet area in mm^2, C is the inlet circumference in mm. Hydraulic diameter is also used to determine the Reynolds number (63). v represents the inlet velocity and ν represents the kinematic viscosity of 50 °C water.

$$D_h = \frac{4 \cdot A}{C} = \frac{4 \cdot 196}{72} = 10.888[mm] \tag{62}$$

$$Re = \frac{v \cdot D_h}{\nu} = \frac{4 \cdot 10.888 \cdot 10^{-3}}{0.553 \cdot 10^{-3}} = 78755.8 \tag{63}$$

7.1.4 Tetrahedral Mesh

The polygon mesh used in numerical model consists of 479 783 cells, it is shown in the Figure 50. Mesh was created using software ANSYS Mechanical/Meshing. A tetrahedral meshing method without wall refinement was selected for two main reasons: it is possible to generate a simple tetrahedral mesh for any different cooling channel geometry and run the simulation, so other geometries can be easily examined. Previously mentioned models by Milnes, Písek and Pitoňák were based on hexahedral element type, Gleitz model works on polyhedra mesh. Tetrahedral approach was not used in any previous hypervapotron CFD research, so it was included in this model. Many different cell sizes were evaluated, the choosen one is the optimal compromise of the computational time and the results quality. The two layers of prismatic inflation are applied on the walls between fluid and solid body to ensure correct turbulence modeling. Skewness metric in tetrahedral elements is calculated as a deviation from a regular tetrahedron shape (all four faces are equilateral triangles). The Figure 48 shows mesh cells of a different skewness quality. The skewness measure ranges from 0 (good) to 1 (bad).

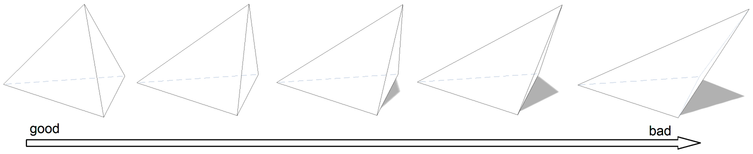

Figure 48: The Skewness Metric

The orthogonal quality evaluates the angles between the face normal vector, the vector connecting centers of two adjacent cells and the vector from the cell center to each of the faces (Figure 49). Orthogonality measure ranges from 0 (bad) to 1 (good). Variants of mesh with wall refinement and lower skewness/orthogonal quality performed really serious convergence problems. Subsequent mesh adaptation in ANSYS Fluent was also considered, but did not lead to any meaningfull improvements. The coarser mesh performed better results in boiling modeling than fine mesh with smaller cells. Mesh metrics data in the Figure 51 shows high orthogonal and skewness quality of used mesh. Red bars in plot represent tetrahedral mesh, green bars represent quality of cells of the inflation layer.

Element Type	Tetrahedral
Inflation	Prismatic
Cells	479 783
Faces	986 092
Nodes	95 224
Minimum Volume (m^3)	7.734626e-13
Maximum Volume (m^3)	6.452427e-11
Minimum Face Area (m^2)	9.608411e-09
Maximum Face Area (m^2)	4.337943e-07

Table 12: Tetrahedral Mesh Cell Parameters

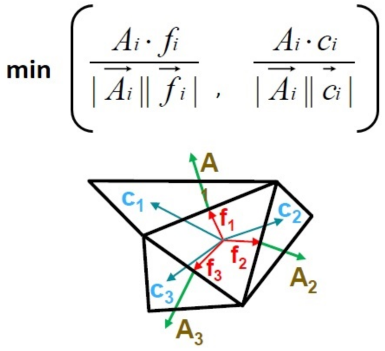

$$\min\left(\frac{A_i \cdot f_i}{|\vec{A_i}||\vec{f_i}|}, \frac{A_i \cdot c_i}{|\vec{A_i}||\vec{c_i}|}\right)$$

Figure 49: Orthogonal Quality

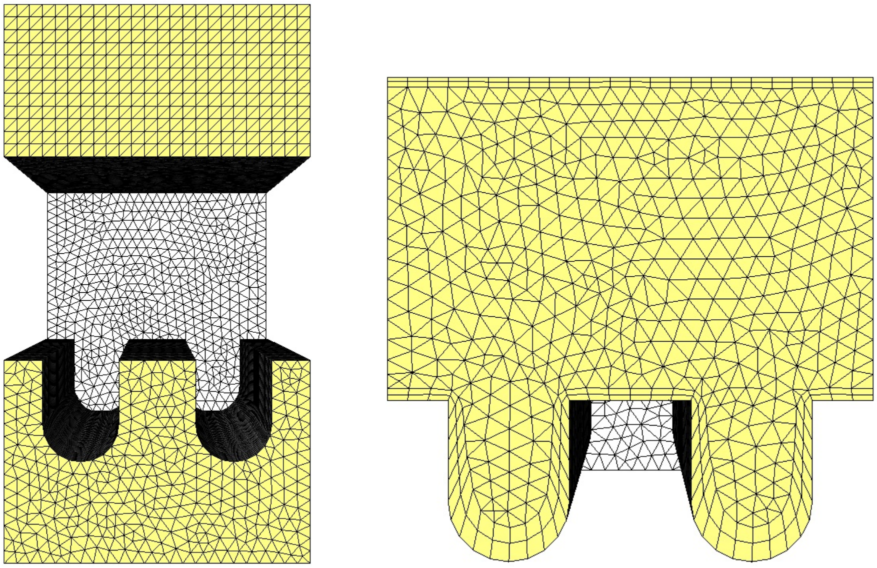

(a) Solid Mesh (b) Fluid Mesh

Figure 50: The Tetrahedral Mesh

Mesh Quality

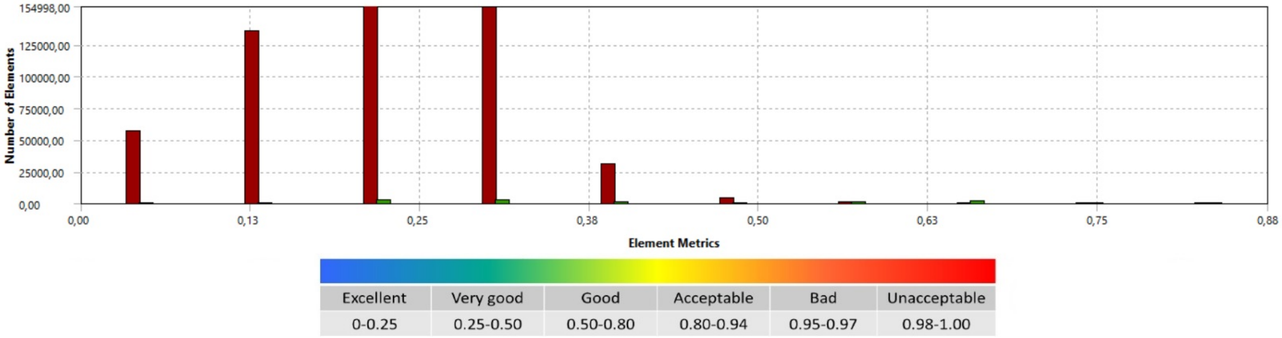

Excellent	Very good	Good	Acceptable	Bad	Unacceptable
0-0.25	0.25-0.50	0.50-0.80	0.80-0.94	0.95-0.97	0.98-1.00

(a) **Skewness**

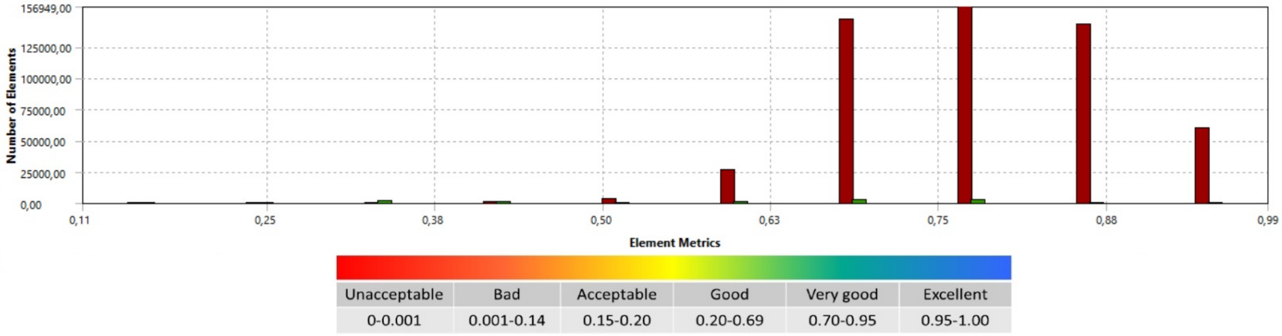

Unacceptable	Bad	Acceptable	Good	Very good	Excellent
0-0.001	0.001-0.14	0.15-0.20	0.20-0.69	0.70-0.95	0.95-1.00

(b) **Orthogonal quality**

Figure 51: The Mesh Metrics

7.1.5 Turbulence Modeling

Viscous Model	$k-\varepsilon$
k-ε Model	Realizable
Near-Wall Treatment	Enhanced Wall Treatment
Multiphase Model	Per Phase

Table 13: The Turbulence Model Settings

The k-ε turbulence model is based on calculating two transport variables: the turbulent kinetic energy k and the rate of dissipation of turbulent kinetic energy ε. Table 14 shows the setting of constants in turbulence model equations. Turbulence equations are solved for the each phase. Modeling the vapour bubbles as dispersed phase to reduce number of equations was considered but did not resulted in converged solution.

$$\frac{\partial(\rho k)}{\partial t}+\frac{\partial(\rho k u_j)}{\partial x_j}=\frac{\partial}{\partial x_j}\left[\left(\mu+\frac{\mu_t}{\sigma_k}\right)\frac{\partial k}{\partial x_j}\right]+G_k+G_b-\rho\varepsilon-Y_M+S_k \tag{64}$$

$$\begin{aligned}\frac{\partial(\rho\varepsilon)}{\partial t}+\frac{\partial(\rho\varepsilon u_j)}{\partial x_j}=&\frac{\partial}{\partial x_j}\left[\left(\mu+\frac{\mu_t}{\sigma_k}\right)\frac{\partial\varepsilon}{\partial x_j}\right]+\\ &\rho C_1 S\varepsilon-\rho C_2\frac{\varepsilon^2}{k+\sqrt{\nu\varepsilon}}+C_{1\varepsilon}\frac{\varepsilon}{k}C_{3\varepsilon}G_b+S_\varepsilon\mu_t E_{ij}E_{ij}-C_{2\varepsilon}\rho\frac{\varepsilon^2}{k}\end{aligned} \tag{65}$$

$$C_1=max\left[0.43,\frac{\eta}{\eta+5}\right],\eta=S\frac{k}{\varepsilon},S=\sqrt{2S_{ij}S_{ij}} \tag{66}$$

Model Constants	
C2-ε	1.9
C3-ε	1.3
TKE Prandtl Number σ_k	1
TDR Prandtl Number σ_ε	1.2
Dispersion Prandtl Number	0.75
Energy Prandtl Number	0.85
Wall Prandtl Number	0.85

Table 14: The Turbulence Model Constants

Near Wall Treatment

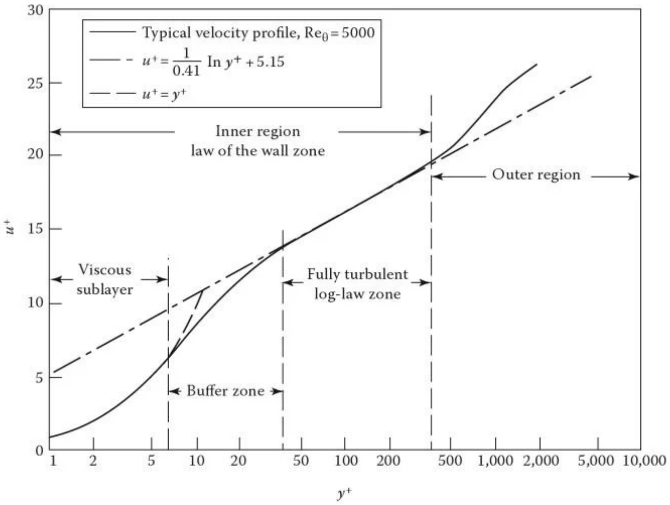

Figure 52: u^+/y^+

$$u^+ \equiv \frac{u}{u_*} \tag{67}$$

$$y^+ \equiv \frac{u_* y}{\nu} \tag{68}$$

$$u_* = \sqrt{\frac{\tau_\omega}{\rho}} \tag{69}$$

$$\tau_\omega = \mu \left(\frac{\partial u}{\partial y} \right)_{y=0} \tag{70}$$

Near wall region can be divided into two zones: the viscous sublayer and the fully turbulent logarithmic layer. The Figure 52 shows relation between a non-dimensional distance from the wall y^+ and a non-dimensional velocity u^+. The crucial problem of using wall functions to model behaviour of fluid near walls is the transition buffer layer between linear and logarithmic zones. For this reason it is recommended to avoid y^+ values 5 to 30 while using the standard wall function model. Non-dimensional metrics are dependend not only on the used mesh, but also on the boundary conditions (velocity, fluid material properties), so it is necessary to run the simulation to calculate its values. The Figure 53 shows y^+ values of used mesh ranging from 5 to 100. Although majority of cells have y^+ over 30, Enhanced Wall Treatment was applied to solve fluid behaviour inside cells in the buffer zone. Enhanced Wall Treatment model is able to blend the linear (laminar) and the logarithmic (turbulent) zone by equation (71) using the blending function given by $\mathit{\Gamma}$.

$$u^+ = e^{\mathit{\Gamma}} u^+_{lam} + e^{1/\mathit{\Gamma}} u^+_{turb} \tag{71}$$

$$\mathit{\Gamma} = \frac{a(y^+)^4}{1 + by^+} \quad a = 0.01, b = 5 \tag{72}$$

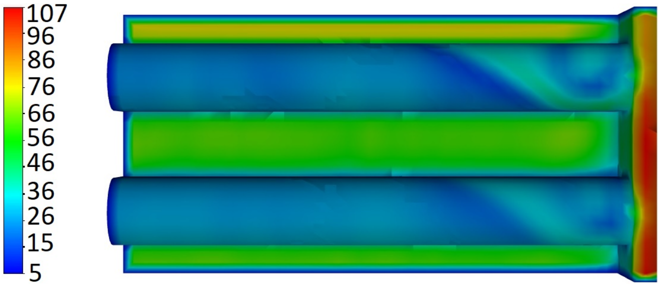

Figure 53: y^+ Values, Tetrahedral Mesh

7.1.6 Multiphase Modeling

Multiphase Model	Eulerian
Boiling Model	RPI
Volume Fraction Formulation	Implicit
Bubble Departure Diameter	Tolubinski Kostanchuk
Frequency of Bubble Departure	UDF, 412 Hz
Nucleation Site Density	Lemmert Chawla
Area Influence Coefficient	Delvalle Kenning
Drag Coefficient	Schiller Naumann
Lift Coefficient	Tomiyama
Turbulence Interaction	Troshko Hassan
Surface Tension Coefficient	0.046845 N/m

Table 15: The Multiphase Model

Wall lubrication, turbulent dispersion, turbulence interaction and virtual mass coefficient are neglected.

Interphase Drag

The drag force acting on the primary phase:

$$D_{pq} = \frac{1}{2}\rho_q C_D A_p (U_p - U_q)|U_p - U_q| \tag{73}$$

Drag force per unit volume (V):

$$D_{pq} = \frac{1}{2}\rho_q C_D \left(\frac{A_p}{V}\right)(U_p - U_q)|U_p - U_q| \tag{74}$$

U_q is the velocity of primary phase, secondary phase moves at velocity U_p. Drag coefficient C_D and interfacial area concentration $\left(\frac{A_p}{V}\right)$ need to be defined. The following equations ((75), Attachment 1) are describing the Schiller Neumann correlation, assuming bubbles of vapour are spherical.

$$C_D = \begin{cases} \frac{24}{Re}\left(1 + 0.15Re^{0.687}\right), & Re < 1000 \\ 0.44, & Re > 1000 \end{cases} \tag{75}$$

$$Re = \frac{\rho_q |U_p - U_q| d_p}{\mu_q} \tag{76}$$

Interphase Heat Transfer

Heat transfer between the phases is calculated using Ranz-Marshall correlation:

$$Nu = 2 + 0.6Re^{0.5}Pr^{0.33} \tag{77}$$

7.1.7 Bubble Diameter

Bubble Departure Diameter

Tolubinski-Kostanchuk (78) correlation was selected to calculate bubble departure diameter based on previously mentioned thesis and other articles [44]. Bubble departure diameter is dependent on subcooling degree in Tolubinski-Kostanchuk correlation. Other available options in ANSYS Fluent are Unal and Kocamustafaogulari-Ishii correlations, both are not suitable for conditions in hypervapotron. The Unal correlation (39) was implemented in one version of model and resulted in very large bubble diameters and high vapour volume fraction, but solution never reached stable temperature profile in the solid body and the convergence. Tolubinski-Kostanchuk and Unal correlations in hypervapotron conditions are compared in the Figure 54(a).

$$D_w = min\left[0.0014, 0.0006e^{\left(\dfrac{-(T_w - T_l)}{45.0}\right)}\right] \qquad [m] \tag{78}$$

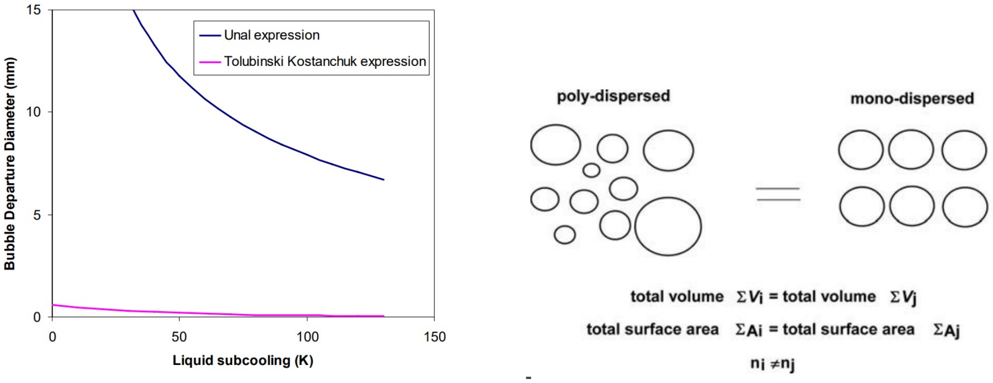

(a) Bubble Departure Diameters [33] (b) Sauter-mean Diameter [34]

Figure 54: Bubble Diameter

Interfacial Area Concentration

Interfacial area concentration is defined as the interfacial area between the continuous liquid phase and the dispersed vapour bubbles. Písek thesis [37] uses simplified model with bubble diameter fixed to 0.15 mm, model in this thesis is considering various bubble diameter to include coalescence/breakage effects. Bubble distribution in this thesis is limited by minimal and maximal bubble diameters of 0.15 and 3 mm, determined by Anglart and Nylund approximation [38] and the dimensions of hypervapotron fins. Interfacial area between the liquid phase and the spherical bubbles is calculated using Sauter-mean function. Physical meaning of Sauter-mean diameter is shown in the Figure 54(b): a collection of spherical objects of different diameters is simplified to a collection of spheres of same diameter. Both systems are equal in total surface area and total volume, but differ in number of objects.

7.1.8 Bubble Departure Frequency

There are two most used bubble departure frequency correlations: Situ and Cole. Milnes thesis tested both settings and confirmed: the Cole correlation is not suitable for conditions in hypervapotron, while Situ correlation with some adjustments can output reasonable values. Other approach for bubble departure frequency is to calculate the velocity of fluid rotation between hypervapotron fins and set frequency to fixed value, this was applied in Písek thesis. Pitoňák thesis used the exactly same approach as Milnes.

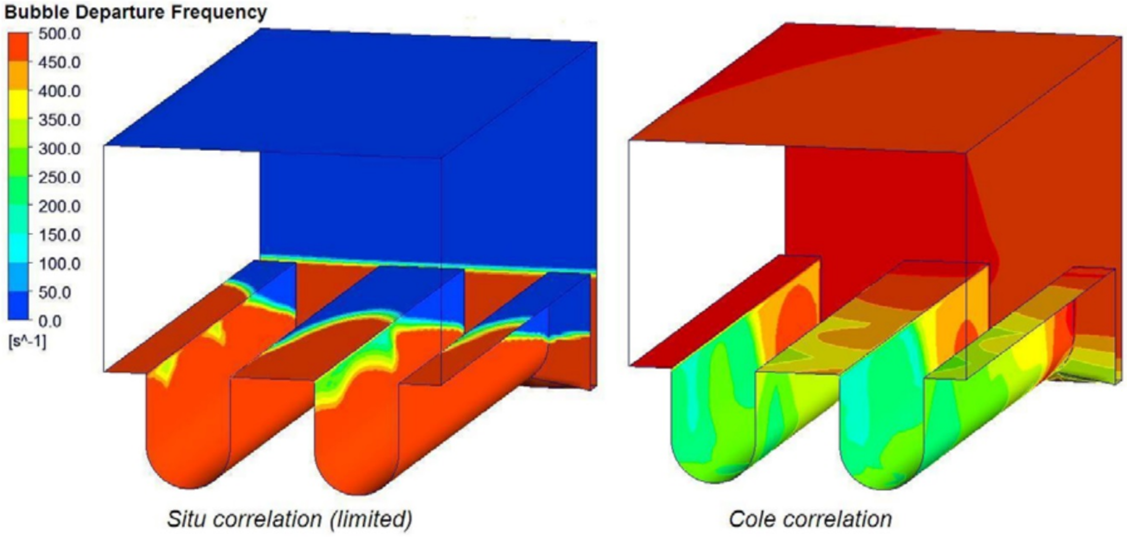

Figure 55: Situ and Cole Results [33]

The Figure 55 shows the resuling frequencies given by Situ and Cole correlation calculated by Milnes. Bubble departure frequency in this thesis is fixed to a constant value of 412 Hz. This frequency was calculated by Milnes using equations (79) and (80). Idea of constant bubble departure frequency is based on the constant fluid rotation between the fins. The rotation time of liquid in the groove T_r is calculated using the inlet velocity ($v = 4m/s$) and the wetted length of the cavity ($l_h = 10^{-3}m$). Frequency is the multiplicative inverse of roration time. Constant frequency is implemented in Fluent as user defined function (UDF) written in C language. This function is presented in Attachment 3 of this thesis.

$$T_r = \frac{l_h}{v} = \frac{9.7 \cdot 10^{-3}}{4} = 2.4 \cdot 10^{-3} s \tag{79}$$

$$f = \frac{1}{T_r} = \frac{1}{2.4 \cdot 10^{-3}} = 412 \; Hz \tag{80}$$

7.1.9 Solution

Conservation equation for transport of a scalar quantity φ:

$$\int_V \frac{\partial \rho\varphi}{\partial t}\, dV + \oint \rho\varphi\vec{v} \cdot d\vec{A} = \oint \Gamma_\varphi \nabla\varphi \cdot d\vec{A} + \int_V S_\varphi\, dV \tag{81}$$

$$\frac{\partial \rho\varphi}{\partial t} V + \sum_f^{N_{faces}} \rho_f \vec{v}_f \varphi_f \cdot \vec{A}_f = \sum_f^{N_{faces}} \Gamma_\varphi \nabla\varphi_f \cdot \vec{A}_f + S_\varphi V \tag{82}$$

The gradient $\nabla\varphi$ of given variable φ is calculated using the **Least Squares Cell-Based** method. This method is assuming the variable is varying linearly. Figure 56(a) and equation (83) shows a change in cell values between cell c_0 and c_i along the vector r_i. Equation (84) represents the system of solved equations where $[J]$ is the coefficient matrix that is purely a function of geometry.

$$(\nabla\varphi)_{c0} \cdot \Delta r_i = (\varphi_{ci} - \varphi_{c0}) \tag{83}$$

$$[J]\,(\nabla\varphi)_{c0} = \Delta\varphi \tag{84}$$

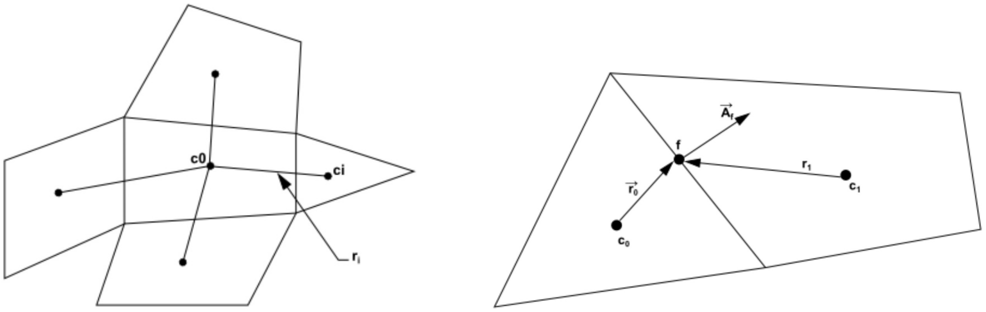

(a) Cell Centroid Evaluation

(b) Control Volume

Figure 56: Discretization

Discrete values of the scalar φ are stored at the cell centers (c_0, c_i). Face values φ_f must be interpolated from the cell center values, this is accomplished using upwind scheme. In the upwind scheme: face value φ_f is derived from quantities in the cell upstream, or "upwind," relative to the direction of the normal velocity $\vec{v}_f$ (82). **First-Order Upwind Scheme** sets the face value φ_f equal to the constant cell-center value of φ in the upstream cell. **Second-Order Upwind Scheme** provide higher order accuracy by implementing the $\nabla\varphi$ gradient of the upstream cell and the displacement vector from the upstream cell centroid to the face centroid $\vec{r}$. Equation (86) represents the Second-Order Upwind Scheme.

$$\varphi_{f,1st\ order} = \varphi \tag{85}$$

$$\varphi_{f,2nd\ order} = \varphi + \nabla\varphi \cdot \vec{r} \tag{86}$$

Pressure-Velocity Coupling	Coupled
Gradient	Least Squares Cell Based
Pressure	PRESTO!
Momentum	Second Order Upwind
Volume Fraction	First Order Upwind
Turbulent Kinetic Energy	First Order Upwind
Turbulent Dissipation Rate	First Order Upwind
Energy	First Order Upwind
Interfacial Area Concentration	First Order Upwind

Table 16: The Solution Methods

Tables 16 and 17 show used settings of methods and under relaxation factors. The pressure-based solver is chosen, since the flow is incompressible. The standard pressure-based algorithm solves the momentum equation and the pressure correction equations separately. Coupled algorithm is implemented to solve the momentum and pressure-based continuity equations together. Relaxation factors are improving the stability of calculation. Under relaxation is limiting the amount by which the variable changes from the previous iteration to the next one. In general: lowering the under-relaxation increase the stability, but also slow down the solution. Following equation (87) describes the principle of relaxation factor α. φ^n represents the new value, φ^{n-1} refers to value in the previous iteration and φ^{n*} is the predicted new value. Relaxation factor $\alpha < 1$ means the solution is under-relaxed, for $\alpha = 1$ no relaxation is applied. To acceelerate the convergence, over-relaxation for $\alpha > 1$ can be also used. Flow Courant Number (Tab. 17) in Fluent does not represent the general definition of Courant Number, but it is a type of relaxation factor.

$$\varphi^n = \varphi^{n-1} + \alpha \times \left(\varphi^{n*} - \varphi^{n-1}\right) \tag{87}$$

Flow Courant Number	20
Momentum	0.5
Pressure	0.5
Body Forces	1
Vaporization Mass	1
Volume Fraction	0.6
Turbulent Kinetic Energy	0.8
Turbulent Dissipation Rate	0.8
Turbulent Viscosity	1
Energy	0.8
Interfacial Area Concentration	0.01

Table 17: The Under Relaxation Factors

7.1.10 Covergence

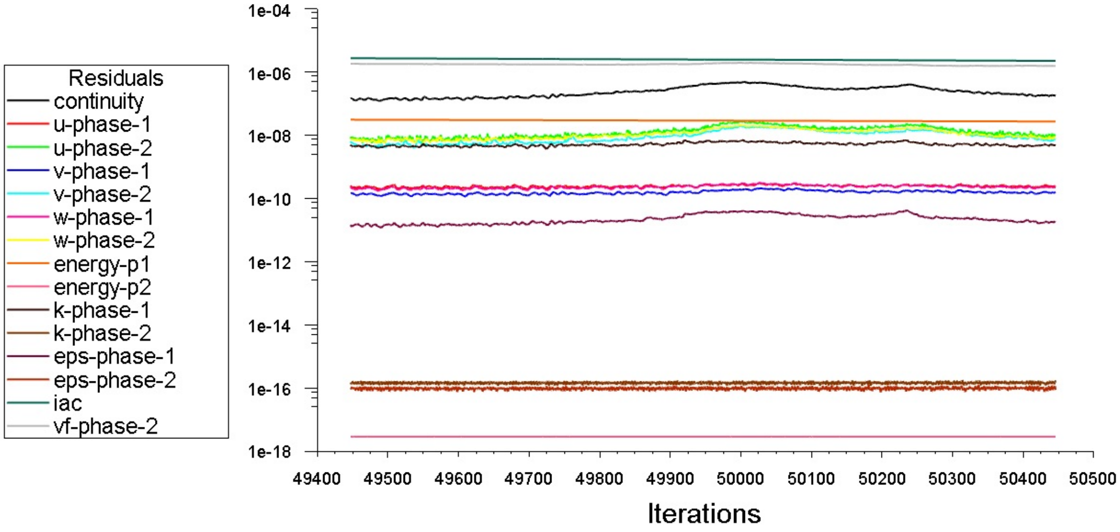

Figure 57: Reached Convergence

Since the analytical solution of given equations is not known, the numerical approach is applied. Numerical approach to solve diferential equations is not able to reach the exact solution, the imbalance of a conserved variable in control volume is measured by a scaled resudials. Figure 57 shows the general convergence criterion for scaled residuals of 10^{-3} was reached for all solved equations. Is it also visible that 15 conservation equations were solved in this model. Model was solved in steady state regime to reach the convergence, switching to the transient solution did not resulted in any significant changes of values. Total heat transfer rate was calculated to ensure the convergence of solution. Minor $0.023W$ imbalance shows the solution converged really well.

```
    mixture
    Total Heat Transfer Rate                  [W]
-------------------------------- --------------------
                       inlet           160931.27
                      outlet           -164291.3
                   wall_flux                3360
            ---------------- --------------------
                         Net        -0.023876448
```

7.1.11 Validation

Experimental data for a model validation are obtained from the 1999 article *Design issues and fatigue lifetime of hypervapotron elements of the JET neutral beam injectors [35].* Hypervapotron channel samples were tested using electron beams at the JAERI Elecron Beam Irradiation System (JEBIS) [45]. One of the three tested hypervapotron channels is used as a horizontal beam limiter at the end of Neutral Injector Boxes (NIB) on JET tokamak (Chapter 1.12.1). The experiment objectives were: test fatigue lifetime of components presently used at JET and test performance of the new optimised Box Scraper hypervapotron element. The "Box Scraper" represents the channel geometry examined in this thesis. Schematic of the experiment is in the Figure 58(a).

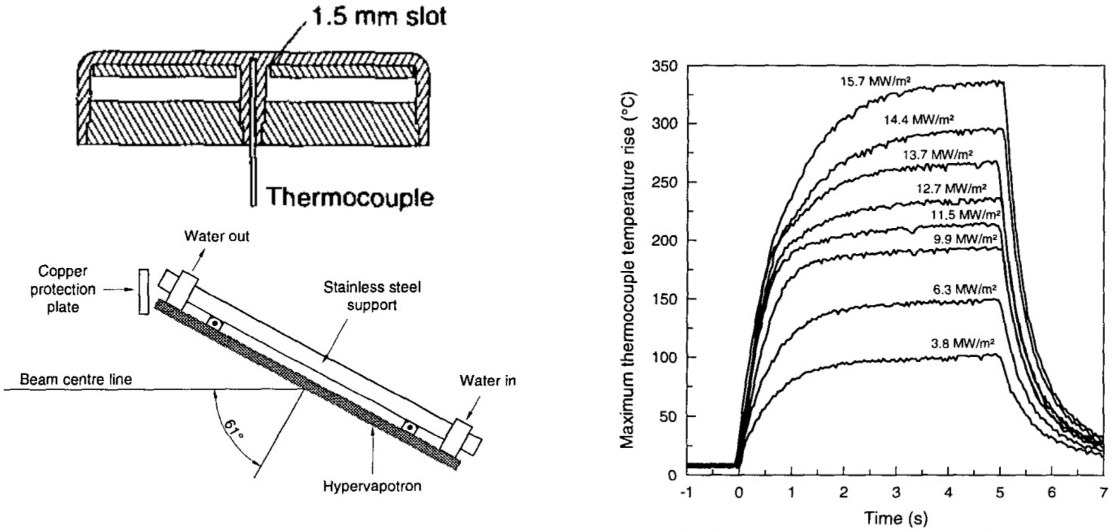

(a) Layout of Experimental NB Test Bed

(b) Thermocouple Temperature Rise (Flow Velocity 6.15 m/s)

Figure 58: The Hypervapotron Experiment

Temperature of the solid body was measured using one thermocouple (see Figure 58(a)) and surface temperature was measured using an infrared imaging system. Milnes [33] assumed the position of thermocouple (Figure 59(a)) and successfully validated his numerical results with available experimental data. Písek and Pitoňák followed Milnes validation in the same way. Unfortunatelly, any other experimental data are not available for model validation, so the validation process is based only on the solid temperature measurement. Experimental measurements on the vapour behaviour in hypervapotron will be benefitial for further research.

NOTE: vertical axis in the Figure 58(b) is labeled as "temperature rise". The experiment was realized in form of heat flux pulses, thus the differences between initial and peak temperatures were measured. This explains why Figure 58(b) and all the validation curves have beginning in the point where no heat flux equals zero temperature rise.

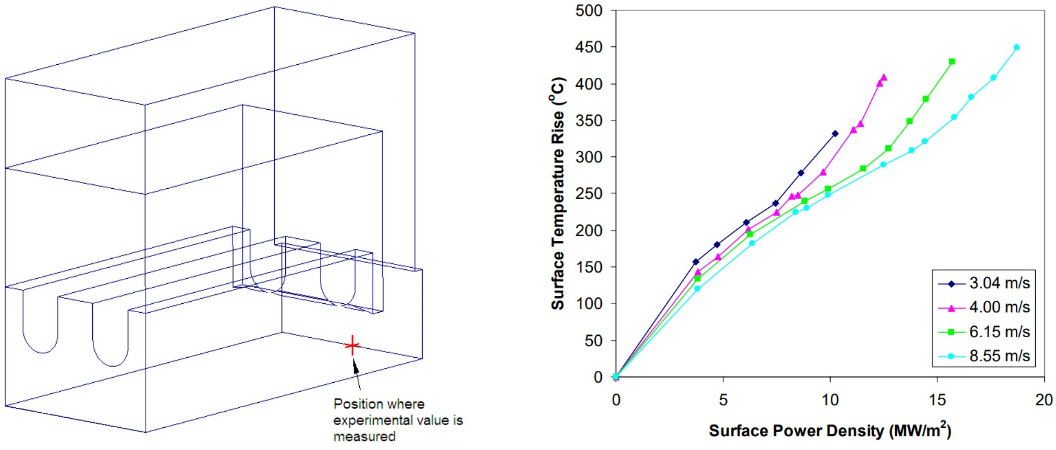

(a) Thermocouple Position (b) Experimental Data

Figure 59: The Experimental Data Processed by Milnes [33]

Comparison of the experimental data and the numerical results is shown in the Figure 60. Temperatures measured in the position of the thermocouple (Fig. 59(a)) are well corresponding with numerical results on the selected range from 0 to 12 MW.m^{-2}. Maximal difference between experimental and numerical results is around 40 °C. Considering the solid body temperature profile, model can be recognized valid. However, there are not enough data points to make definitive conclusions if the numerical model match reality.

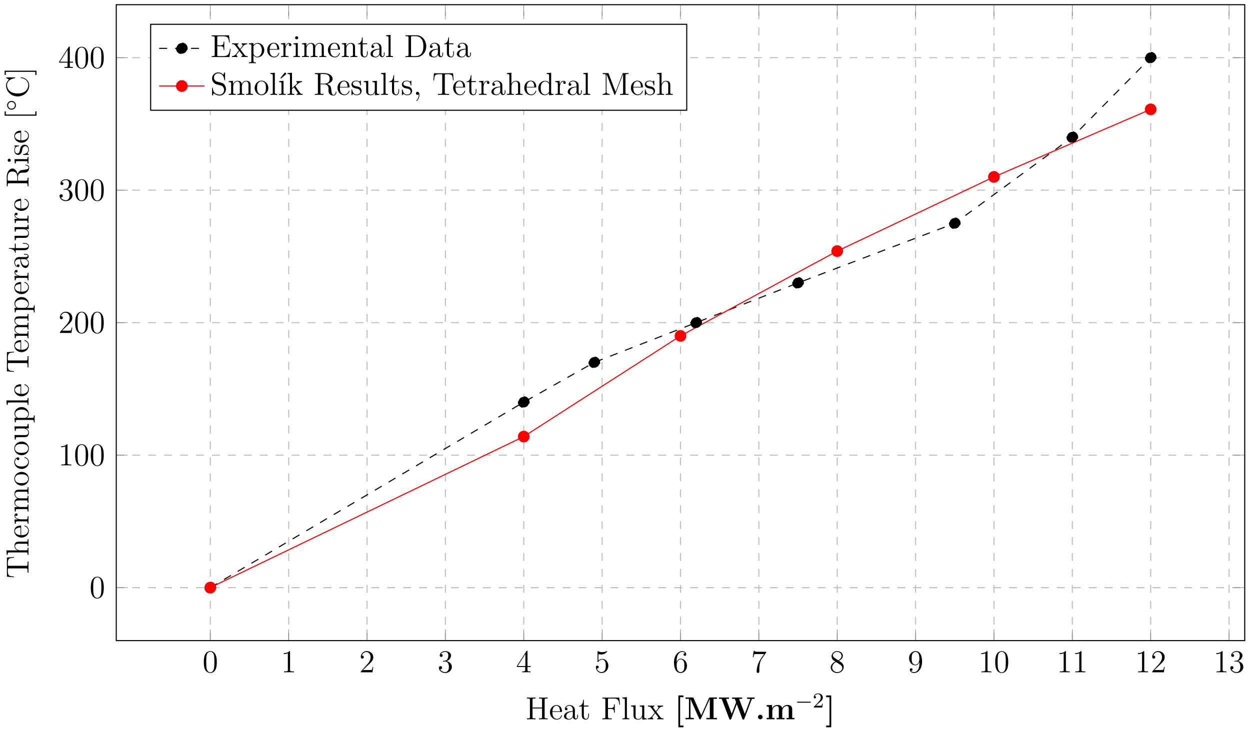

Figure 60: The Validation of Numerical Results

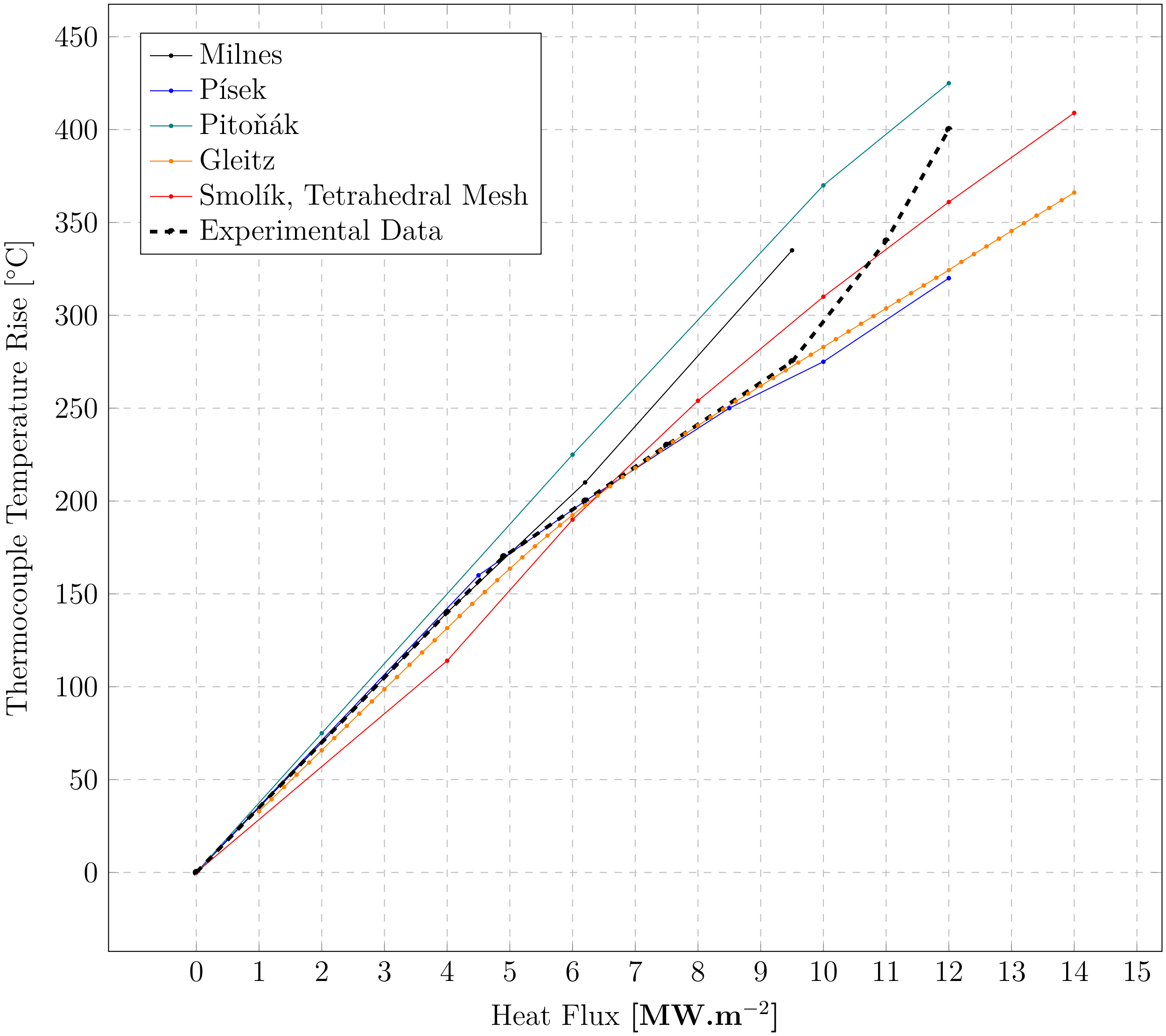

Figure 61: The Validation of Numerical Analysis

The Figure 61 shows the comparison of experimental data and the results of previously conducted numerical anylysis to illustrate how well are the other thesis validated. Heat flux range shown in 61 is limited to 14 MW.m^{-2} to highlight the differences between experimental and numerical data. The experimental data curve show the increased slope for heat fluxes higher than 9.5 MW.m^{-2}. This behaviour can be explained by the creation of stable vapour layer on the walls, insulating the solid body. Similar behaviour is slightly observable in the results of Gleitz thesis (Chapter 6.5 Figure 45) for higher heat fluxes. Only Písek numerical analysis successfully reached this result matching the experimental data. However, this Písek conclusion is based on increased temperature of only one data point and the vapour distribution in his model is questionable. From this poin of view: none of the numerical analysis matched experimental results. For heat fluxes over 6 MW.m^{-2}, results of this thesis stay in the range between maximal and minimal temperatures of other numerical analysis. Results of solid body temperature are further discussed in the following chapter.

7.2 Results

The following chapters are describing various results of performed simulation. To illustrate the process of solution: resulting maximal solid temperature and vapour volume fraction during the calculation are shown in the Figure 62. The initial temperature of solid body was set to 300 °C, initial liquid temperature of 50 °C is corresponding with the inlet boundary condition. Both values are stabilized after 14 000 iterations. There are observable similarities between the temperature plot in Figure 62 and the experimental data shown in Figure 58. However, the horizontal axis in numerical results do not represent any time scale. It represents temperature value progress per iteration, that is highly dependent on numerical approach and relaxation factors used for solution.

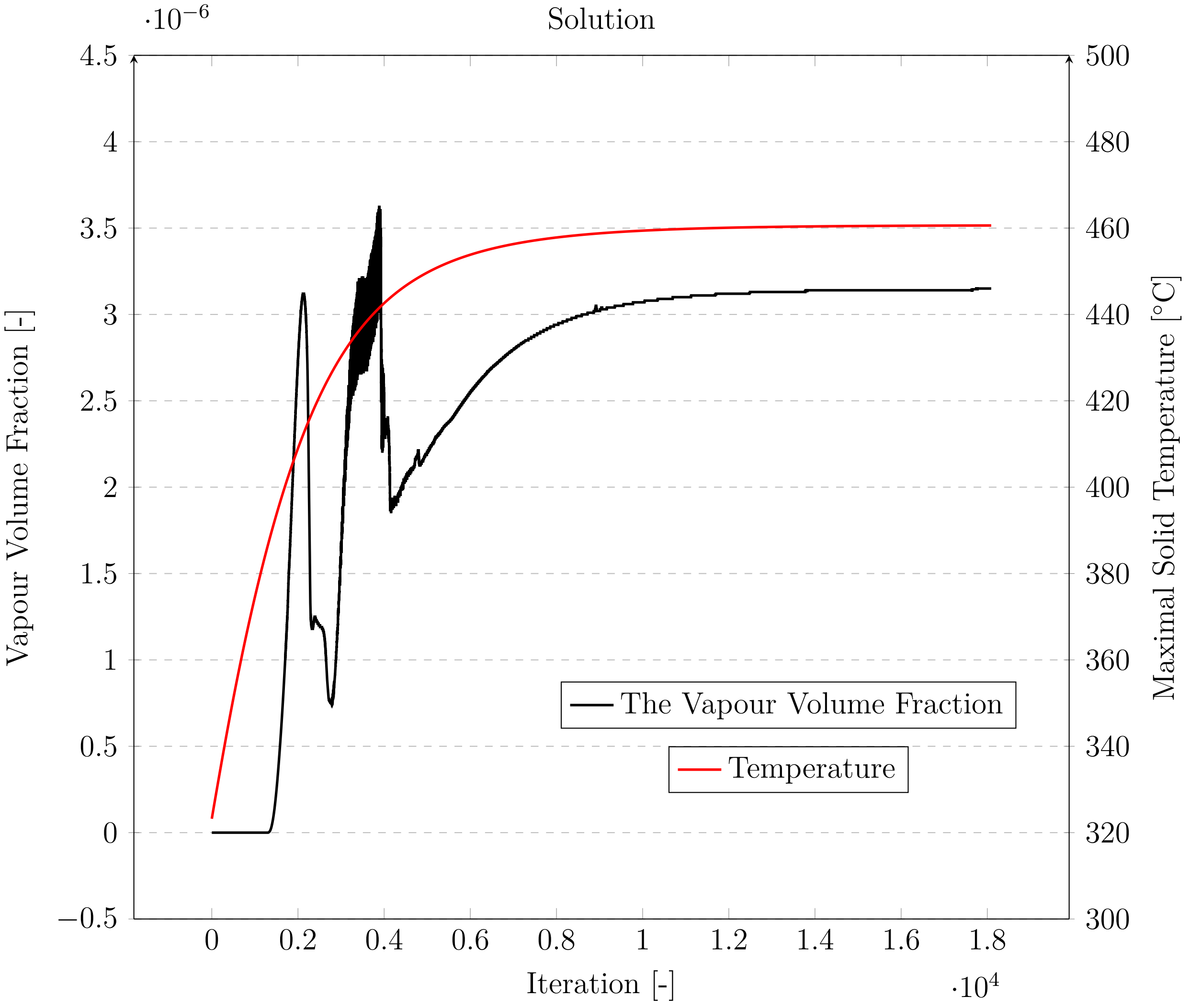

Figure 62: The Solution, 12 MW.m^{-2}

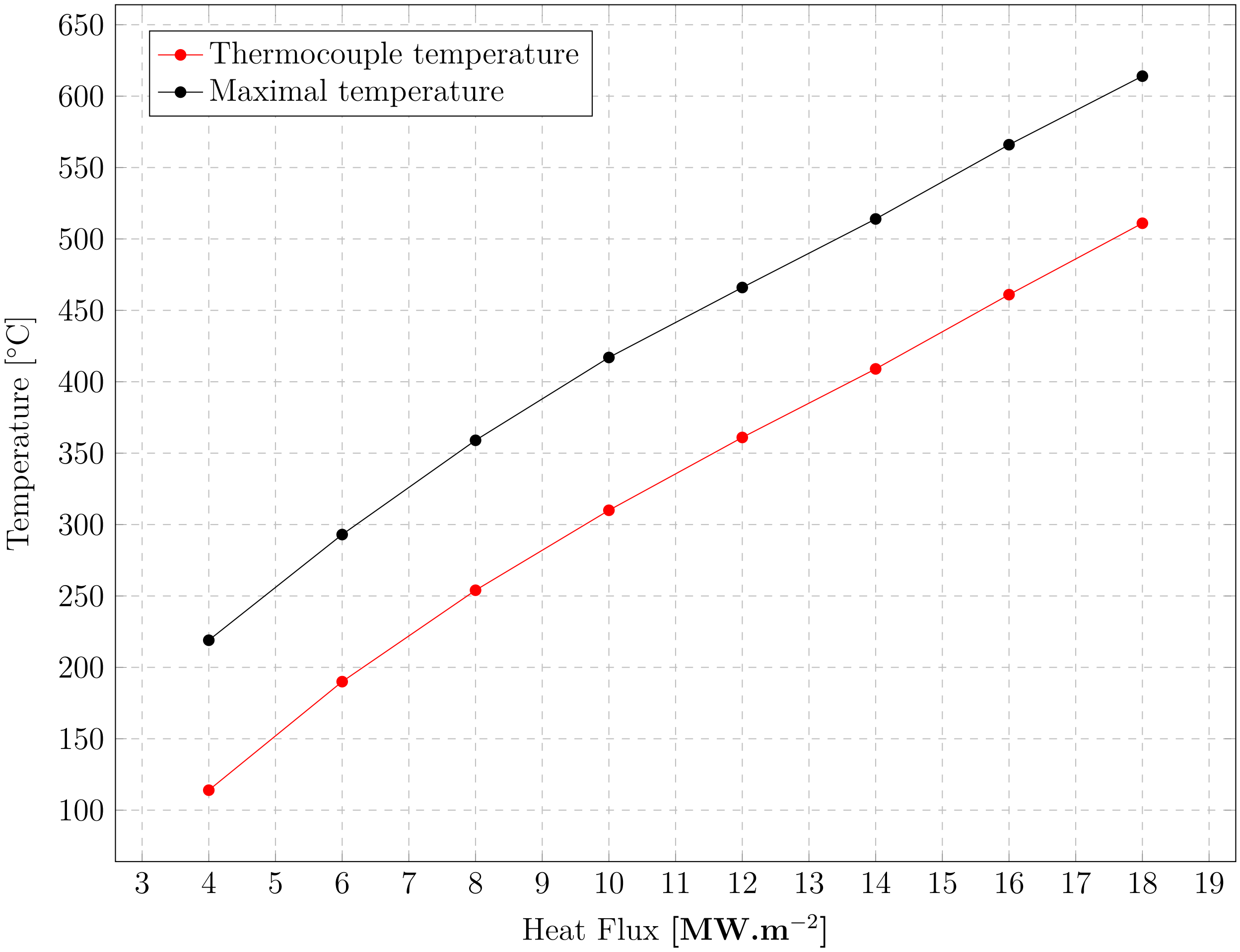

Figure 63: The Solid Body Temperature, Tetrahedral Mesh

Previous validation graphs mentioned the *temperature rise* to match the experimental data. Figure 63 shows the complete results of maximal solid body temperature and the temperature measured at the thermocouple position (Fig. 59(a)). The slope of the temperature curve changes slightly over the selected heat flux range. Results are limited to 18 MW.m^{-2} for the reason of limited computational time within this thesis.

Resulting slope of the temperature curve is not increasing for higher heat fluxes, because the vapour is concentrated in the center of vortex between the hypervapotron fins. The vapour behaviour is described in detail in the following chapter. In the case of stable vapour layer on the channel walls: the temperature will increase due to the insulation ability of vapour. Experimental data indicates the vapour layer should be present, therefore the performed numerical analysis is not accurate from this point of view. This inaccuracy is most likely caused by tetrahedral mesh used in this model. Vapour behaviour of the same model applied on a different type of mesh is described in the following Chapter 7.2.6. .

7.2.1 Temperature Profile

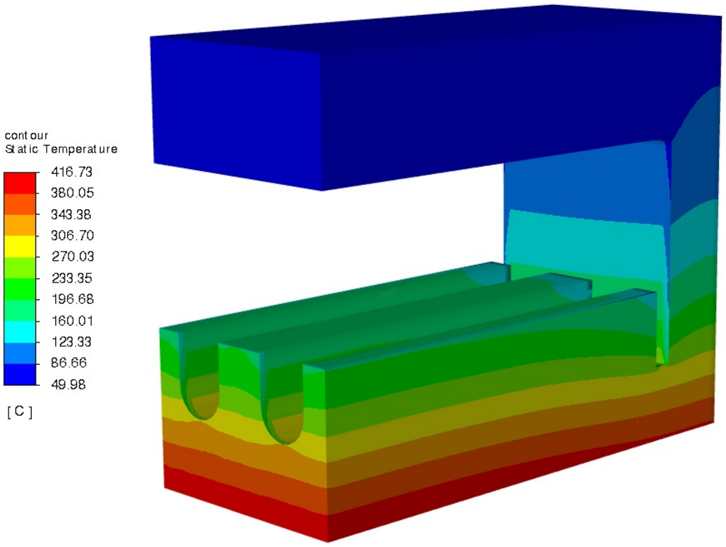

Figure 64: The Temperature Profile, 10 MW.m^{-2}

Figures 64 and 65 show the temperature profile of the solid body for heat flux of 10 MW.m^{-2}. The maximal temperature on the exposed wall reaches 416.73 °C. Table 18 compares the maximal temperature reached by the previous thesis on the same boundary conditions. Results vary in a wide range of the values.

Milnes	Písek	Pitoňák	Gleitz	Smolík
448 [°C]	413 [°C]	452 [°C]	343 [°C]	416 [°C]

Table 18: Maximal Solid Temperatures, 10 MW.m^{-2}

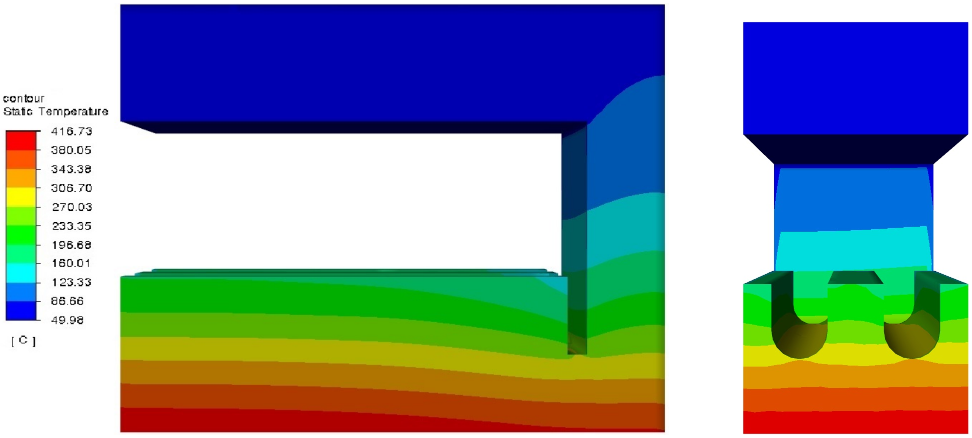

(a) (inlet)

(b) (symmetry)

Figure 65: The Temperature Profile, 10 MW.m^{-2}

7.2.2 Velocity Streamlines

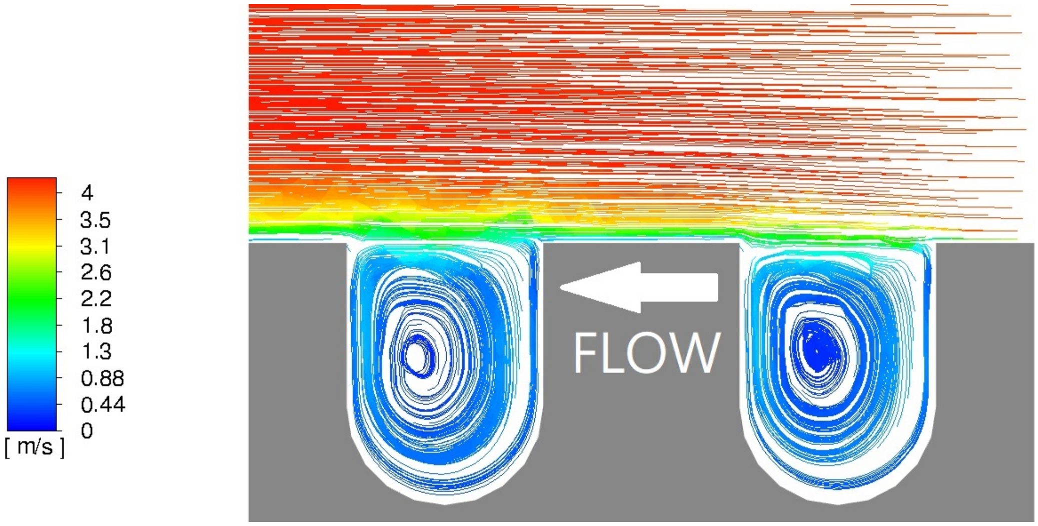

Figure 66: The Velocity Streamlines, v = 4 $m.s^{-1}$

The Figure 66 shows the velocity streamlines profile in the central symmetry plane. Rotation inside fins corresponds with Milnes simulation of hypervapotron 2D solution in Chapter 6.1. Vortex formation and velocity profile is in agreement with particle image velocimetry data described in chapter 4.3. From this point of view, model behaviour of fluid between the fins can be considered valid. Figure 67 shows how much is the flow affected by the presence of the groove on the side of channel. Milnes thesis calculations proved the most efficient velocity profile is the one present on the symmetry plane (Figure 66). Thus, any disturbing of this one-vortex rotation is not desirable. Arrow in figures indicates the direction of main channel flow.

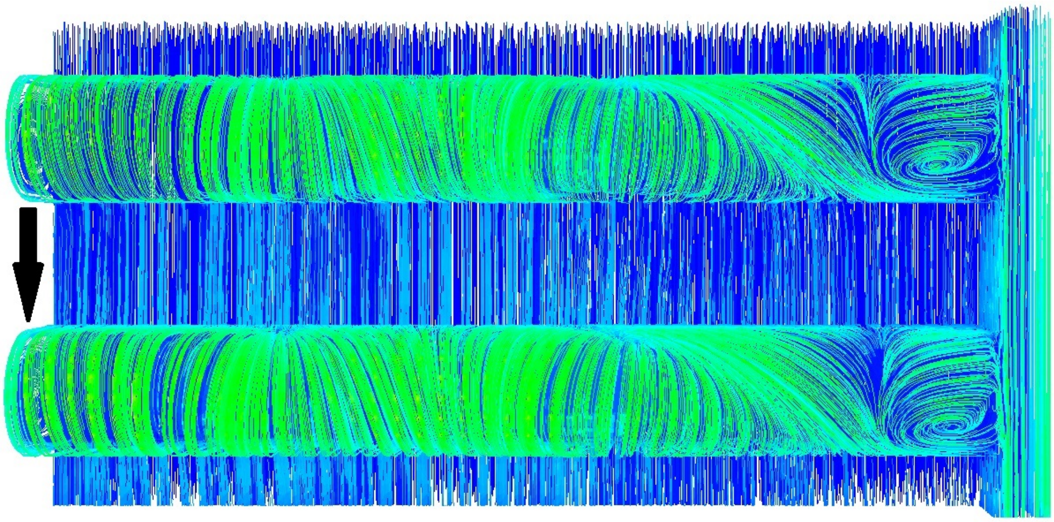

Figure 67: The Streamlines, v = 4 $m.s^{-1}$

7.2.3 Vapour Volume Fraction

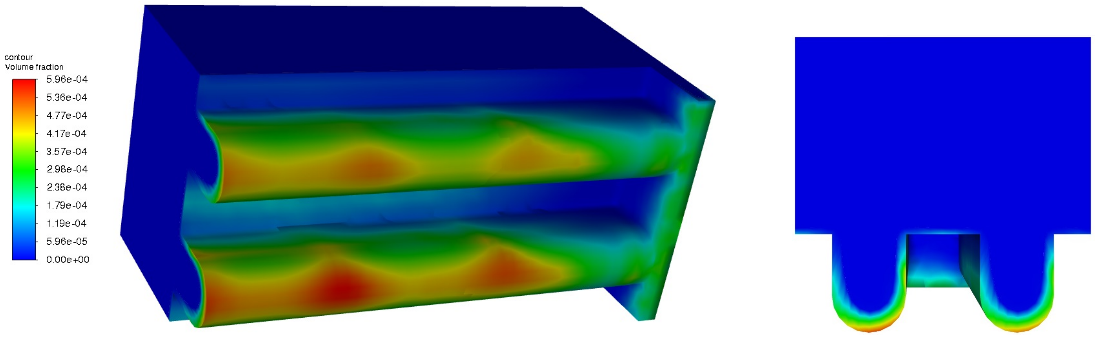

(a) Contour

(b) Symmetry Plane

Figure 68: The Vapour Volume Fraction, Tetrahedral Mesh, 10 MW.m^{-2}

Figure 68 shows the vapour volume fraction distribution inside the hypervapotron channel for heat flux of 10 MW.m^{-2}. Maximum value of volume fraction is $5.69.10^{-4}$, this value is really low compared to the other previous simulations. Distribution of vapour is visibly corresponding with the velocity streamline profile shown in the previous chapter. The area where the rotation of fluid is the least affected by the flow inside groove on the side of channel generate the highest vapour volume fraction. To test the vapour behaviour of model, heat flux was increased up to 20 MW.m^{-2}. Figure 69 shows the vapour distribution for 18 MW.m^{-2} heat flux. For lower heat fluxes: the bubbles of vapour are distributed only along the channel wall and the vapour fraction is lower than results in all the other thesis. Around 16 MW.m^{-2}: the bubbles start to detach from the walls, gathering and interconnecting in the flow vortex (visible in Figure 69(b)). For 20 MW.m^{-2}: vapour is fully concentrated in the central vortex.

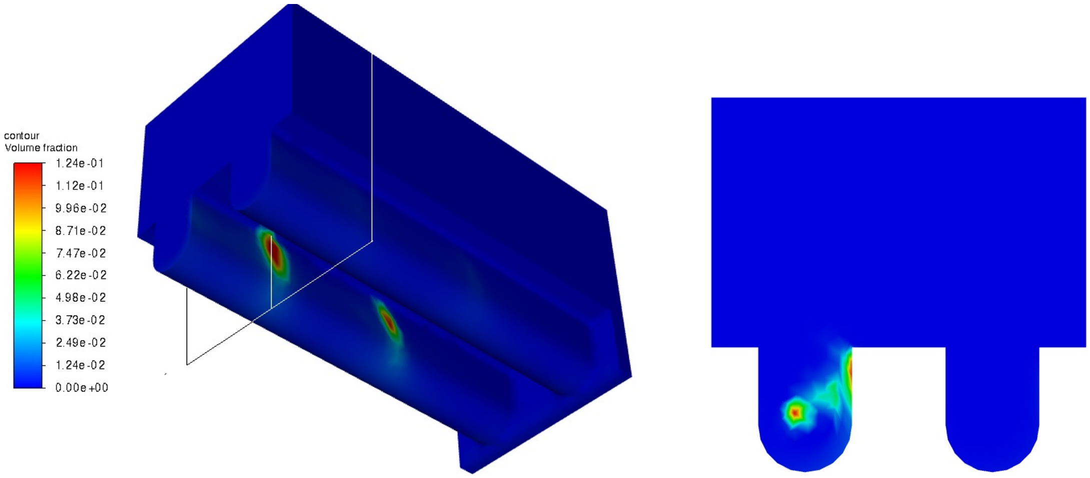

(a) Contour

(b) Plane

Figure 69: The Vapour Volume Fraction, Tetrahedral Mesh, 18 MW.m^{-2}

The biggest shortcoming of this numerical analysis (compared to the other thesis) is the low vapour volume fraction. The production of vapour for different heat fluxes is shown in the Figure 70, logarithmic scale was applied on vertical axis. For 10 MW.m^{-2}: previous analysis resulted in maximal vapour volume fractions in the range of 10^{-1}, results of this thesis are in the range of 10^{-3}. Vapour volume fraction near 1 was reached at the heat flux of 18 MW.m^{-2}. The previous works on hypervapotron subcooled boiling did not cover similar graph measure and the experimental data are also not available, therefore it is difficult to evaluate results. Vapour fractions are expected to reach higher values, a presence of local vapour layer on the channel wall is also expected for heat fluxes over 10 MW.m^{-2}. Problems with vapour behaviour at higher heat fluxes are revised in the following Chapter 7.2.6. .

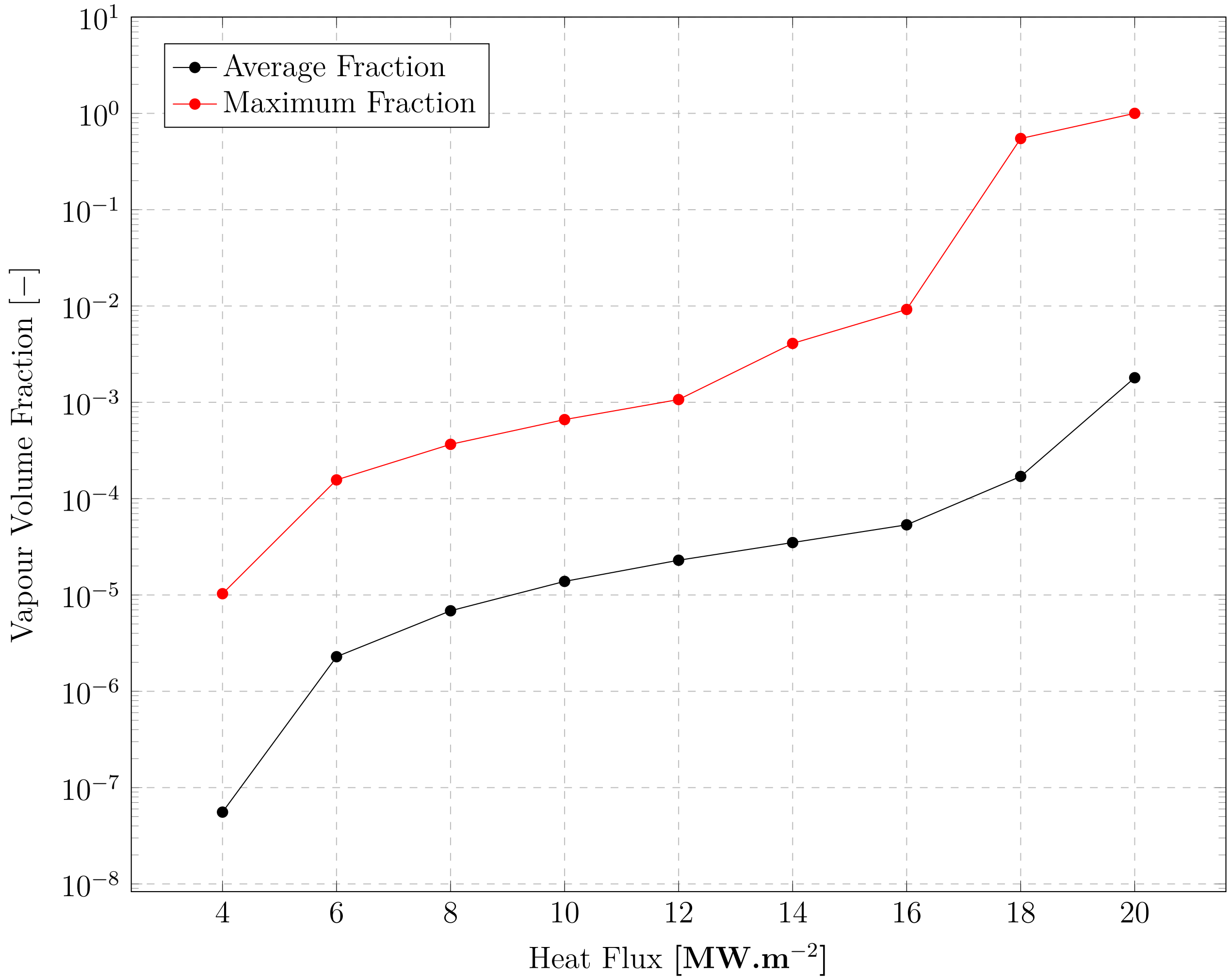

Figure 70: The Vapour Volume Fraction, Tetrahedral Mesh

7.2.4 Bubble Diameter

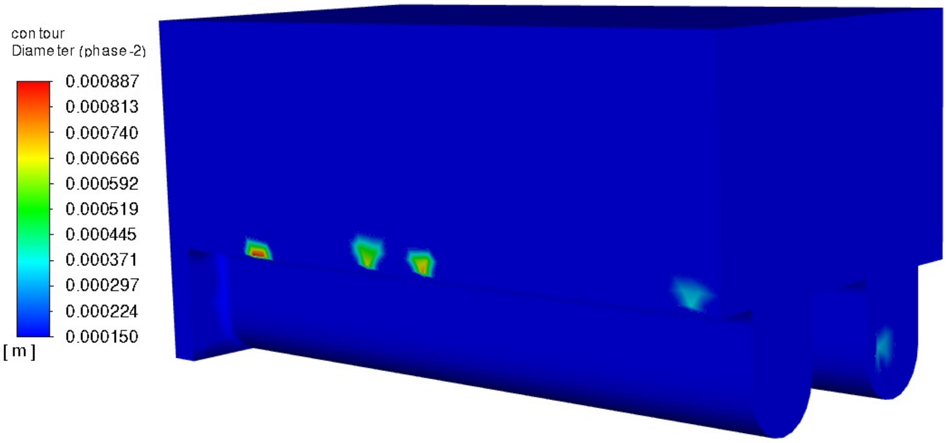

Figure 71: Bubble Diameter Distribution, 10 MW.m^{-2}

Figure 71 shows the bubble size distribution inside hypervapotron channel. The bubble diameter vary from 0.15 to 0.887 mm. Variable bubble diameter is the evidence of functional bubbles coalescence simulation. Location of the larger bubbles also indicates the physically reasonable behaviour of used model. The bubble diameter distribution is also shown in bar chart in the Figure 72. Vertical axis represent the percentage representation of given diameter in fluid.

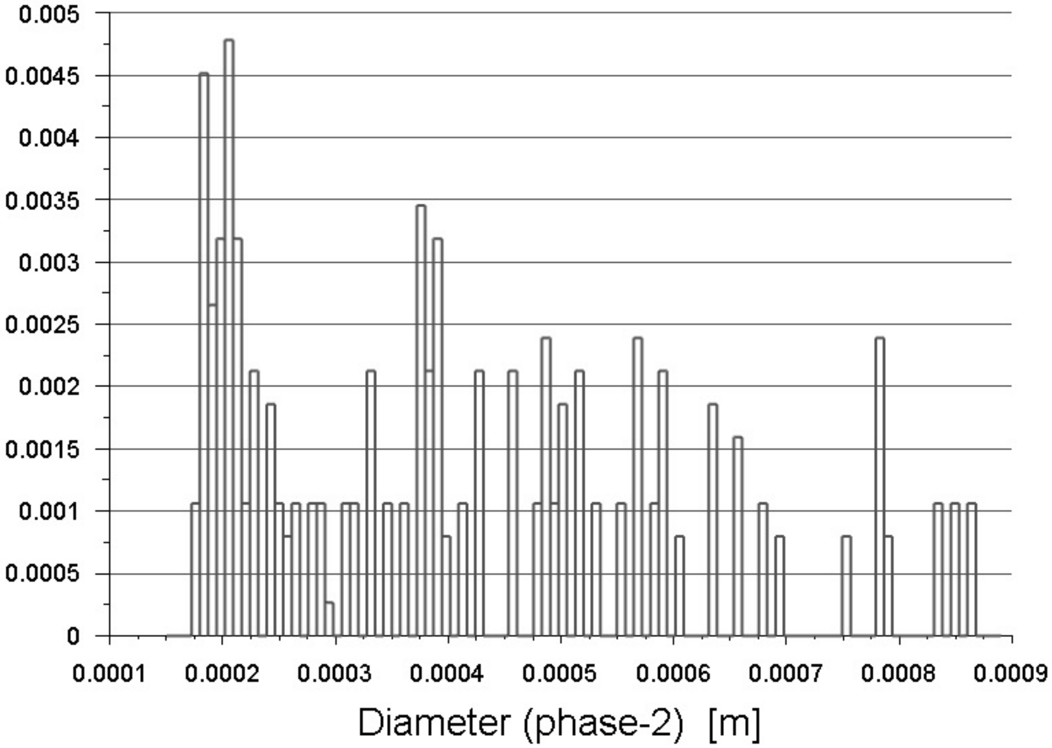

Figure 72: Bubble Diameter Distribution Bar Chart, Tetrahedral Mesh, 10 MW.m^{-2}

7.2.5 Diverse Mesh Solution 1 - Geometry Modification

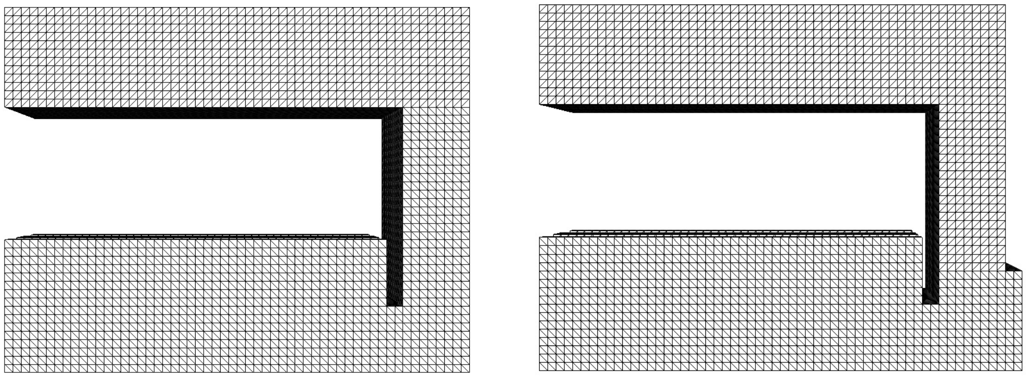

(a) Original Geometry (b) Modificated Geometry

Figure 73: The Mesh Modification

A modificated mesh with additional side solid part was created to test the effect of the temperature profile difference between Milnes model and a simplified model used in this thesis. Figure 73 shows the mesh modification. Figure 74 shows how the temperature profile of solid body changed. Additional area of exposed wall results in increased total heat flux. However, this additional heat increased the maximal solid body temperature only by 1.2 °C. Additional solid body can be neglected. The simplified geometry of cooling channel (Figure 74(a)) was also implemented in Gleitz model (Chapter 6.5).

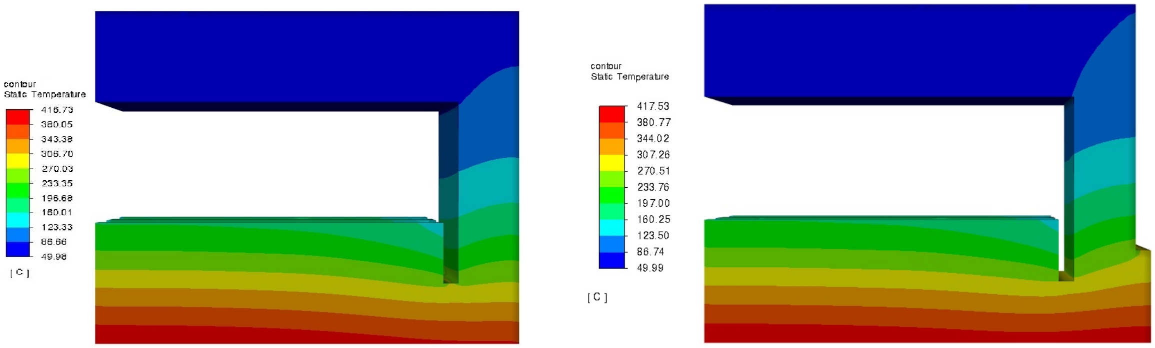

(a) Original Geometry (b) Modificated Geometry

Figure 74: The Solid Body Temperature Distribution

7.2.6 Diverse Mesh Solution 2 - Hexahedral Mesh

Model used for solution was also applied to a different type of the mesh. Mesh created for the purpose of this thesis contains certain imperfections (for expample: variable first layer thickness), as the the author did not have enough experience with the meshing process. Hexahedral mesh used by Písek and Pitoňák was implemented to check how the results will differ. Hexahedral mesh is described in detail in Attachment 4 of this thesis. Multiphase model is unchanged, turbulence model was set to Písek solution (Non-Equilibrium wall functions) since its very mesh-dependend. The Figure 75 shows the solid temperature profile for 10 MW.m^{-2} heat flux. There is only 2°C difference in maximal solid temperature between tetrahedral and hexahedral mesh solution. Unfortunatelly, Písek did not defined the whole exposed solid wall as one cell zone, thus it was not possible to exactly match the heat flux boundary condition. The cell zones are hardly changeable after the mesh is fully generated, so there is a visible difference in temperature distribution.

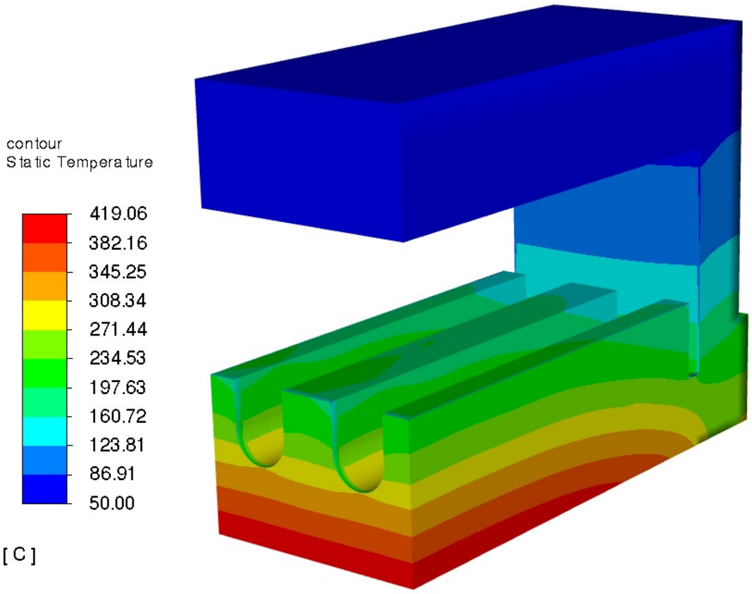

Figure 75: The Temperature Profile, Hexahedral Mesh, 10 MW.m^{-2}

Vapour distribution is the major difference compared to the original Písek results mentioned in Chapter 6.3 and also the tetrahedral mesh results of this thesis. At lower heat fluxes, hexahedral and tetrahedral mesh give similar results. At 10 MW.m^{-2} heat flux: vapour forms a stable local layer on the surface of the cooling channel. For higher heat fluxes: vapour is filling the space between the hypervapotron fins.

NOTE: heat fluxes over 10 MW.m^{-2} require transition solution, as the large bubbles of vapour are leaving the channel fins in pulses. Higher heat fluxes experienced serious convergence issues, it was not possible to fully solve this problem for the reason of limited computational time within this thesis.

The Figure 76 represents the final results of numerical analysis of this thesis. Results of tetrahedral and hexahedral solution are compared with experimental data. Hexahedral mesh solution resuls match with the experimental data on a larger heat flux range. Increased slope of the resulting curve for high heat fluxes indicates the presence of an insulating layer of vapour. Thus, switching from tetrahedral to hexahedral mesh radically changed the vapour behaviour and helped to more precisely match the available experimental data. Figures 77, 78 and 79 show the vapour volume fraction for different heat fluxes.

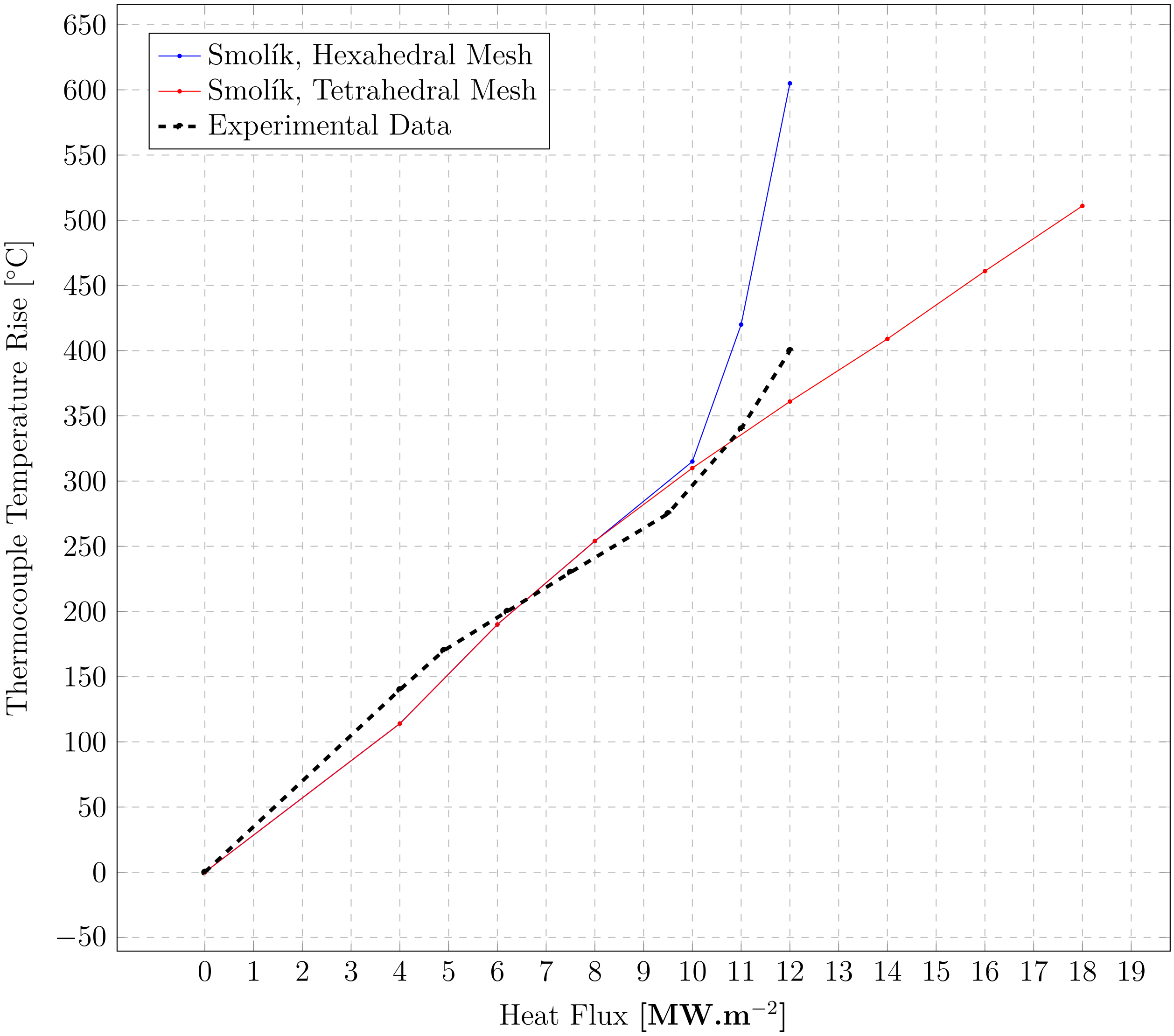

Figure 76: The Final Results of Numerical Analysis

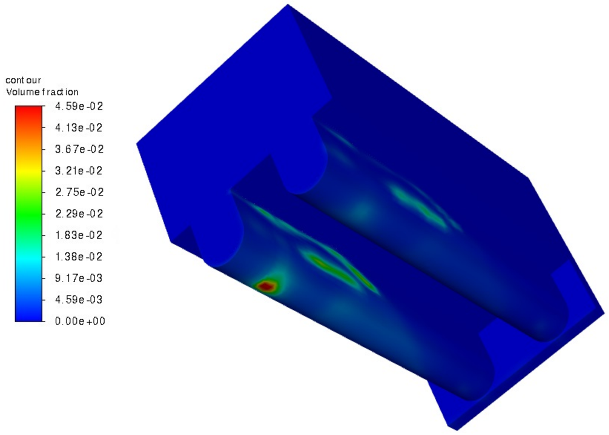

Figure 77: Vapour Volume Fraction, Hexahedral Mesh, 10 MW.m^{-2}

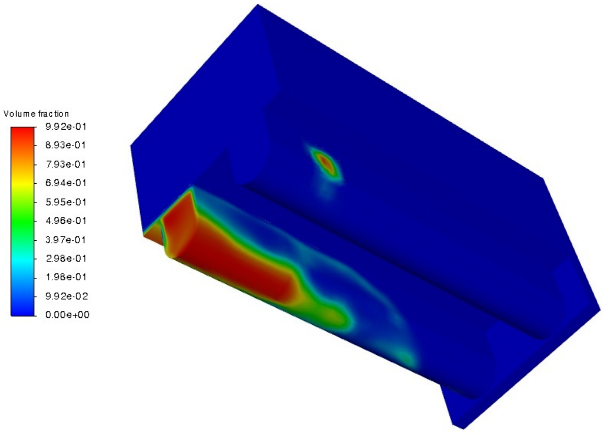

Figure 78: Vapour Volume Fraction, Hexahedral Mesh, 11 MW.m^{-2}

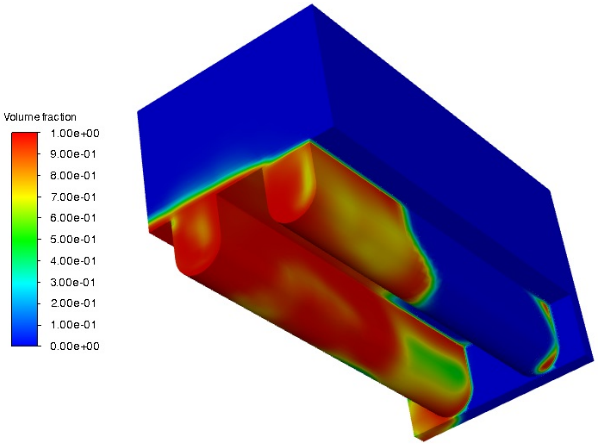

Figure 79: Vapour Volume Fraction, Hexahedral Mesh, 12 MW.m^{-2}

Figure 80 shows the bubble diameter distribution bar chart for 10 MW.m^{-2} heat flux calculated using hexahedral mesh. There are differences in comparison with results mentioned in Chapter 7.2.4. . The majority of bubble diameters are near the minimal limit of 0.15 *mm*. Figure 81 shows the bubble diameter distribution bar chart for 12 MW.m^{-2} heat flux. Solution for higher heat flux contain larger number of bubbles near the maximal diameter.

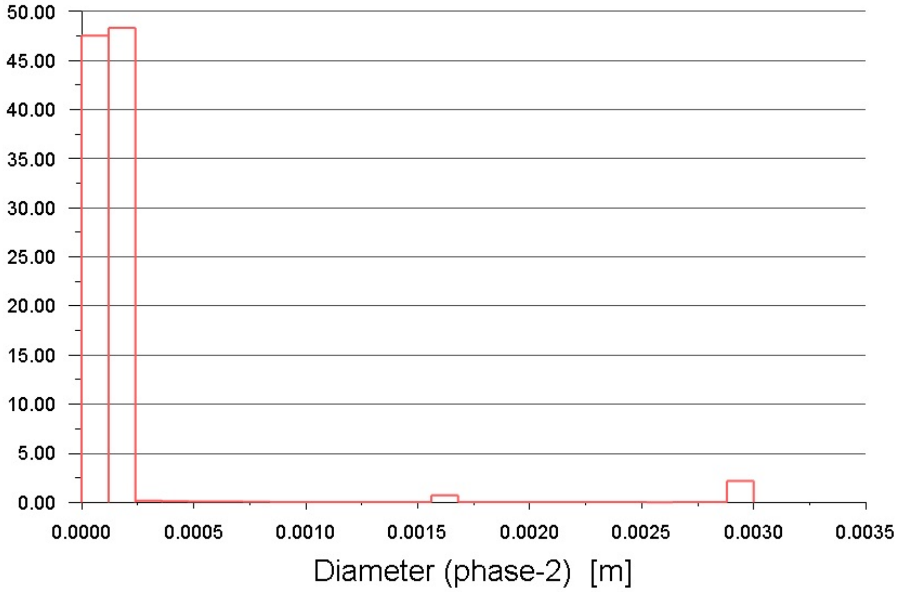

Figure 80: Bubble Diameter Distribution Bar Chart, Hexahedral Mesh, 10 MW.m^{-2}

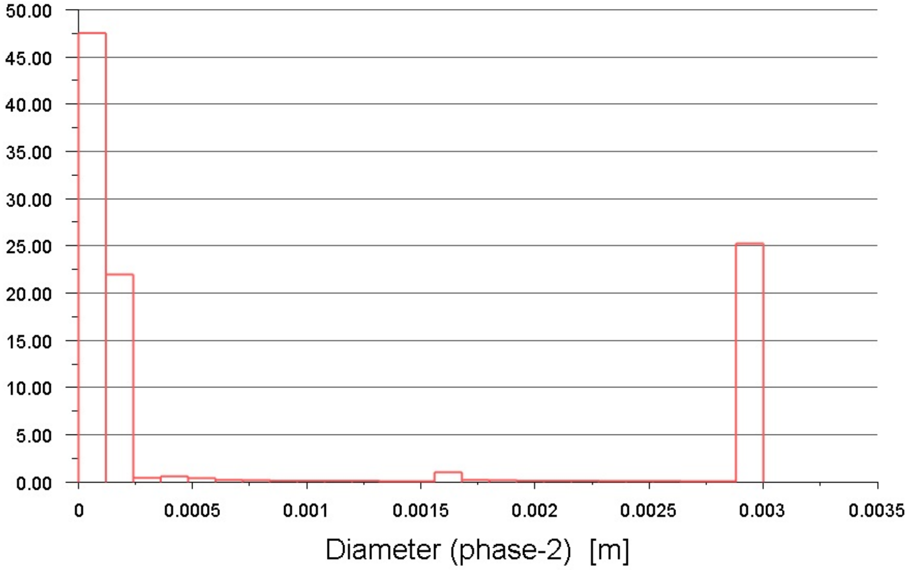

Figure 81: Bubble Diameter Distribution Bar Chart, Hexahedral Mesh, 12 MW.m^{-2}

8 Conclusion

This diploma thesis is focused on the high heat flux cooling technology based on the subcooled boiling phenomenon. The theoretical part of this thesis descibes the current status of nuclear fusion research and the application of hypervapotron cooling channel in fusion reactors. Introduction to the heat transfer theory is followed by the systematic review of experimental and numerical studies of hypervapotron. The theoretical part lays the foundation for the numerical analysis performed in the following practical part.

ANSYS Fluent 2021 R2 was selected for the CFD numerical analysis. The hypervapotron geometry tetrahedral mesh was created to match the previous numerical analysis by other authors and the available experimental data. Eulerian multiphase model was set to fit the conditions of hypervapotron subcooled boiling. The results of numerical analysis showed flow patterns inside the channel, vapour distribution and the temperature profile of solid body. Vortex formation between the hypervapotron fins is in agreement with the previous work of Milnes and experimental data.

The vapour distribution and the interaction between phases in the cooling channel represents the biggest challenge of hypervapotron solution. The results of analysis performed on the tetrahedral mesh (created by the author of this thesis) performed well for lower heat fluxes. However, the experimental data show increased slope of the temperature curve for heat fluxes over 10 MW.m^{-2}, most likely caused by the insulating layer of vapour inside the channel. This increase of slope in not present in the tetrahedral mesh results. Therefore, the second solution was performed using the indentical multiphase model, but diverse mesh. Hexahedral mesh was taken over from the previous thesis by Václav Písek.

The results of solution based on the hexahedral mesh show increasing temperature for higher heat fluxes, caused by the increase of vapour volume fraction in the space between the hypervapotron fins. From this point of view, hexahedeal mesh solution is in better agreement with available experimental data. However, the high vapour fraction is causing extreme overheating of the solid body up to the temperatures exceeding the experimental values.

One of the contributions of this thesis is the simulation of variable bubble diameters, previous ANSYS Fluent work of Písek fixed bubble diameter to a constant value. The vapour bubble diameters distributions are shown in bar charts in Figure 72, 80 and 81. Comparison of this thesis (2021) and Písek thesis (2016) also represents how the ANSYS Fluent software changed between version 16.2 and 21.2. The results of numerical analysis can also be compared with the works of other authors based on the ANSYS CFX and Star CCM+ software. CFD software used for numerical analysis is able to solve the subcooled boiling, but most of the models are validated for the conditions in pressurized water reactors. The models parameters are set to deal with higher pressure values (PWR: 15 MPa, Hypervapotron: 0.6 MPa), therefore the hypervapotron solution requires many user settings.

One of the biggest challenges of this thesis was the computational time management. Many different types of meshing and boundary conditions were considered and the correctness of solution could be often evaluated only after many hours of solution.

Two numerical results are presented, both fit the experimental values for low heat fluxes. For heat fluxes over 10 MW.m^{-2}: results of the tetrahedral mesh reach lower and hexahedral mesh exceed the experimental data. More experimental results are needed to fully evaluate the quality of performed numerical solution. Experimental analysis of vapour bubble behaviour inside the hypervapotron channel can help to adjust the multiphase interaction settings to improve the accuracy of future numerical models.

ANSYS Fluent 21.2 is not able to fully simulate the subcooled boiling regime in hypervapotron conditions

9 Bibliography

[1] J. Ongena, “Fusion: a true challenge for an enormous reward,” *EPJ Web of Conferences*, vol. 189, p. 00015, 01 2018.

[2] M. Agostini, K. Altenmüller, S. Appel, V. Atroshchenko, Z. Bagdasarian, D. Basilico, G. Bellini, J. Benziger, R. Biondi, D. Bravo, B. Caccianiga, F. Calaprice, A. Caminata, P. Cavalcante, A. Chepurnov, D. D’Angelo, S. Davini, A. Derbin, A. Di Giacinto, and G. Zuzel, “Sensitivity to neutrinos from the solar cno cycle in borexino,” *The European Physical Journal C*, vol. 80, 11 2020.

[3] J. Ongena, “Fusion: A true challenge for an enormous reward,” *EPJ Web of Conferences*, vol. 98, p. 05004, 01 2015.

[4] R. Hameed and O. Oudah, “Reaching to a featured formula to deduce the energy of the heaviest particles producing from the controlled thermonuclear fusion reactions,” *Journal of Physics: Conference Series*, vol. 1003, p. 012076, 05 2018.

[5] J. D. Lawson, “Some criteria for a power producing thermonuclear reactor,” *Proceedings of the Physical Society. Section B*, vol. 70, pp. 6–10, jan 1957.

[6] T. Kammash, “Fusion power and its prospects,” in *Alternative Energy Sources* (J. T. Mannasah, ed.), pp. 607–685, Academic Press, 1981.

[7] G. Dimov, “Helium-3 from the moon for the low radioactive nuclear energetics,” *Journal of Fusion Energy*, vol. 33, 10 2014.

[8] P. Kulhánek, *Úvod do teorie plazmatu.* Prague: AGA, 2011.

[9] https://www.iter.org/ [accessed 20.4. 2022], “Iter organisation [online],” *ITER.*

[10] I. Maemunah, Z. Su’ud, A. Waris, and D. Irwanto, “Study on fusion blanket with ceramic solid as tritium breeding material,” *Journal of Physics: Conference Series*, vol. 2072, p. 012004, 11 2021.

[11] T. Hirai, S. Panayotis, V. Barabash, C. Amzallag, F. Escourbiac, A. Durocher, M. Merola, J. Linke, T. Loewenhoff, G. Pintsuk, M. Wirtz, and I. Uytdenhouwen, “Use of tungsten material for the iter divertor,” *Nuclear Materials and Energy*, 07 2016.

[12] B. H.-S, R. Wolf, T. Andreeva, J. Baldzuhn, B. D., B. T., B. H., V. Bykov, A. Cardella, F. Durodie, E. M., E. V., G. G., D. Hartmann, H. D., H. P., H. B., H. C., and M. Zuin, “Technical challenges in the construction of steady-state stellarator wendelstein 7-x,” *Nuclear Fusion*, vol. 53, p. 126001, 12 2013.

[13] B. Zohuri, *Inertial Confinement Fusion (ICF)*, pp. 193–238. 01 2017.

[14] O. Larroche, *An extended hydrodynamics model for inertial confinement fusion hohlraums.* 08 2021.

[15] https://lasers.llnl.gov/science/icf [accessed 20.4. 2022], "National ignition facility [online]," *NIF.*

[16] S. Entler, "Engineering breakeven," *Journal of Fusion Energy*, vol. 34, pp. 513–518, 06 2015.

[17] M. Keilhacker and M. Watkins, "D–t experiments in the jet tokamak," *Journal of Nuclear Materials*, vol. s 266–269, p. 1–13, 03 1999.

[18] https://ccfe.ukaea.uk/research/joint-european-torus/ [accessed 20.4. 2022], "Culham center for fusion energy [online]," *Joint European Torus, JET.*

[19] M. Claessens, *ITER: The Giant Fusion Reactor: Bringing a Sun to Earth.* 03 2020.

[20] G. Dell'Orco, W. Curd, J. Berry, K. Chang, J. Ferrada, B. Gopalapillai, D. Gupta, S. Kim, I. Kuehn, A. Kumar, F. Li, A. Petrov, and W. Reiersen, "Design modification and optimization of the iter cooling water system," *Fusion Engineering and Design*, vol. 86, no. 1, pp. 15–19, 2011.

[21] Y. Someya, K. Tobita, R. Hiwatari, and Y. Sakamoto, "Fusion demo reactor design based on nuclear analysis," *Fusion Engineering and Design*, vol. 136, 05 2018.

[22] K. Leong, J. Ho, and K. Wong, "A critical review of pool and flow boiling heat transfer of dielectric fluids on enhanced surfaces," *Applied Thermal Engineering*, vol. 112, pp. 999–1019, 2017.

[23] P. Agrawal and G. Mchale, *Leidenfrost Effect and Surface Wettability*, pp. 189–233. 01 2022.

[24] J. Lim and M. Park, "Predicting the onset of nucleate boiling heat flux of one-side heated flat heat sink in sub-cooled flow conditions for fusion divertor cooling," *Physica Scripta*, vol. 96, 12 2021.

[25] R. Pitts, X. Bonnin, F. Escourbiac, H. Frerichs, J. Gunn, T. Hirai, A. Kukushkin, E. Kaveeva, M. Miller, D. Moulton, V. Rozhansky, I. Senichenkov, E. Sytova, O. Schmitz, P. Stangeby, G. De Temmerman, I. Veselova, and S. Wiesen, "Physics basis for the first iter tungsten divertor," *Nuclear Materials and Energy*, vol. 20, p. 100696, 2019.

[26] P. Chen, W. Wu, B. G. Jones, and T. A. Newell, "Heat transfer for subcooled flow boiling in hypervapotron configuration," *Nuclear Technology*, vol. 164, no. 1, pp. 89–96, 2008.

[27] Y. Wang and A. Dedov, "An review for the heat transfer researches of hypervapotron in the iter first wall," *Journal of Physics: Conference Series*, vol. 1683, p. 022100, 12 2020.

[28] A. Sergis, Y. Hardalupas, and T. Barrett, “Isothermal analysis of nanofluid flow inside hypervapotrons using particle image velocimetry,” *Experimental Thermal and Fluid Science*, vol. 93, pp. 32–44, 2018.

[29] B. Pan, W. Wang, D. Chu, L. Mei, and Q. Zhang, “Experimental investigation of hypervapotron heat transfer enhancement with alumina–water nanofluids,” *International Journal of Heat and Mass Transfer*, vol. 98, pp. 738–745, 07 2016.

[30] J. H. Lim, M. G. Park, H. G. Oh, D. K. Hwang, G. C. Lee, M. H. Kim, and H. Jo, “Experimental study of hypervapotron channel with square fin structure for divertor cooling by one-side, electric joule heating system,” *Fusion Engineering and Design*, vol. 161, p. 112072, 2020.

[31] W. Wang, H. Deng, S. Huang, D. Chu, B. Yang, L. Mei, and B. Pan, “Experimental and numerical investigation of HyperVapotron heat transfer,” *Nuclear Fusion*, vol. 54, p. 123004, oct 2014.

[32] V. N. M, M. Bandyopadhyay, M. Singh, A. Chakraborty, J. Joshi, H. Patel, S. Khirwadkar, S. Belsare, R. Swamy, K. Bhope, and S. Tripathi, “Evaluation of heat transfer performance of hypervapotron elements in two phase flow devised in indian test facility,” *Fusion Engineering and Design*, vol. 155, p. 111543, 2020.

[33] J. Milnes, *Computational Modelling of the HyperVapotron Cooling Technique for Nuclear Fusion Applications.* PhD thesis, Department of Aerospace Sciences Cranfield University, Cranfield, UK, 2010.

[34] P. Kowalczuk and J. Drzymala, “Physical meaning of the sauter mean diameter of spherical particulate matter,” *Particulate Science and Technology*, vol. 34, pp. 645–647, 10 2015.

[35] D. Ciric, M. Akiba, H.-D. Falter, D. Martin, K. Sato, and K. Yokoyama, “Design issues and fatigue lifetime of hypervapotron elements of the jet neutral beam injectors,” in *18th IEEE/NPSS Symposium on Fusion Engineering. Symposium Proceedings (Cat. No.99CH37050)*, pp. 407–410, 1999.

[36] V. Pitoňák, “Studie podchlazeného varu v hypervapotronu,” Master’s thesis, ČESKÉ VYSOKÉ UČENÍ TECHNICKÉ V PRAZE, Fakulta Strojní, Prague, 2017.

[37] V. Písek, “Ověření aplikovatelnosti cfd metodik pro výpočty podchlazeného varu,” Master’s thesis, ČESKÉ VYSOKÉ UČENÍ TECHNICKÉ V PRAZE, Fakulta Strojní, Prague, 2016.

[38] J. Milnes, A. Burns, and D. Drikakis, “Computational modelling of the hypervapotron cooling technique,” *Fusion Engineering and Design*, vol. 87, no. 9, pp. 1647–1661, 2012.

[39] P. Domalapally and F. Subba, “Computational thermal fluid dynamic analysis of hypervapotron heat sink for high heat flux devices application,” *Fusion Engineering and Design*, vol. 98-99, pp. 1267–1270, 2015. Proceedings of the 28th Symposium On Fusion Technology (SOFT-28).

[40] M. Gleitz, P. Zacha, S. Entler, and J. Syblík, “Design of experimental device for testing of subcooled flow boilling,” pp. 150–153, 01 2020.

[41] Y. Birol, “Thermal fatigue testing of cucrzr alloy for high temperature tooling applications,” *Journal of Materials Science*, vol. 45, pp. 4501–4506, 08 2010.

[42] J. Wisniewski, J.-M. Drezet, D. Ayrault, and B. Cauwe, “Determination of the thermophysical properties of a cucr1zr alloy from liquid state down to room temperature,” *International Journal of Material Forming*, vol. 1, pp. 1059–1062, 04 2008.

[43] P. Hanzelka, V. Musilova, T. Kralik, and J. Vonka, “Thermal conductivity of a cucrzr alloy from 5k to room temperatures,” *Cryogenics*, vol. 50, no. 11, pp. 737–742, 2010.

[44] T. Pirez and G. Ribeiro, “Numerical evaluation of the wall heat flux partitioning model of a r134a subcooled boiling flow,” 10 2019.

[45] H. Shirakata, “The jt-60 machine upgrade and development towards the next step in japan,” in *Fusion Technology 1990* (B. KEEN, M. HUGUET, and R. HEMSWORTH, eds.), pp. 7–19, Oxford: Elsevier, 1991.

10 Attachments

10.1 Attachment 1

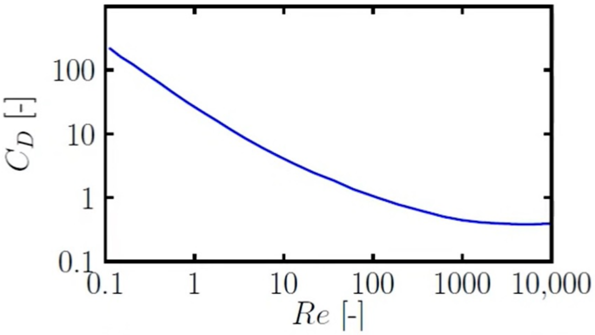

Figure 82: Schiller Neumann Correlation

10.2 Attachment 2

Anglart and Nylund correlation for bubble diameter [33]:

$$d_b = \frac{d_1 - d_0}{T_1 - T_0} T_{sub} + \frac{d_0 T_1 - d_1 T_0}{T_1 - T_0} \tag{88}$$

T_{sub} is the local liquid subcooling, and d_0 and d_1 are the bubble diameters at reference liquid subcoolings, T_0 and T_1, respectively.

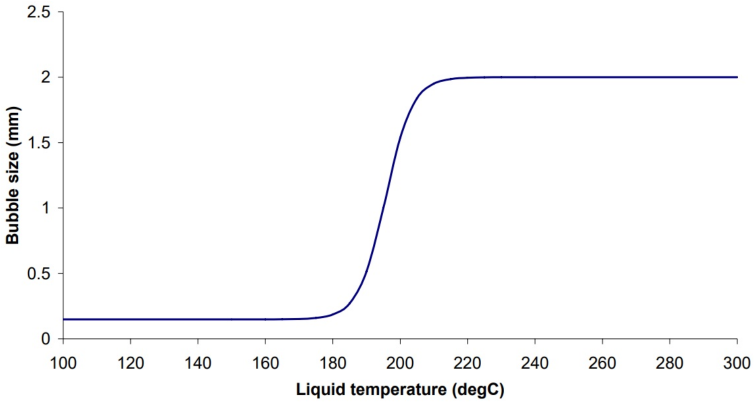

Figure 83: Anglart and Nylund Correlation

10.3 Attachment 3

User defined function to calculate the bubble departure frequency:

```
#include "udf.h"

DEFINE_BOILING_PROPERTY(bubble_frekv,f,t,c0,t0,from_index,from_species_index,
to_index,to_species_index)
{
real bubble_fr;
bubble_fr = 412;
return bubble_fr;
}
```

10.4 Attachment 4

Hexahedral Mesh used for solution in Chapter 7.2.6 *(Created by Václav Písek [37].)*

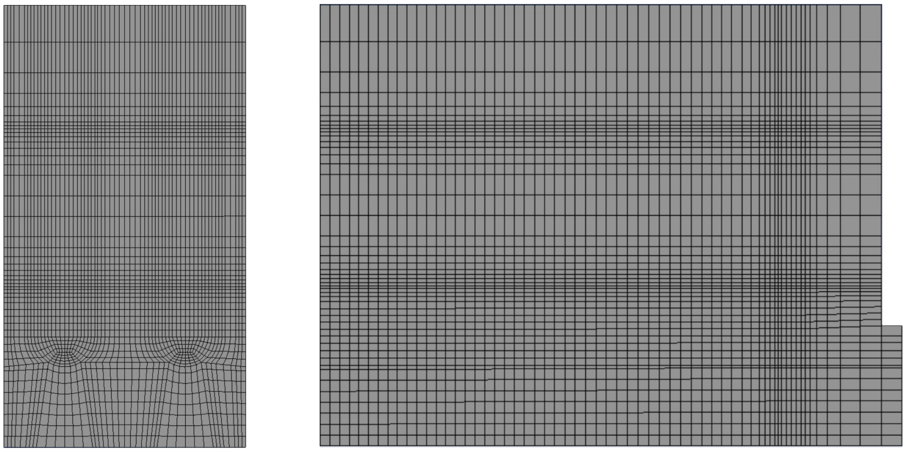

(a) Symmetry View (b) Side View

Figure 84: The Hexahedral Mesh

Element Type	Hexahedral
Mesh Type	Structured
Cells	169 546
Faces	528 035
Nodes	190 479
Minimum Volume (m^3)	2.151551e-12
Maximum Volume (m^3)	5.144513e-10
Minimum Face Area (m^2)	1.434367e-08
Maximum Face Area (m^2)	1.957524e-06
Minimum Orthogonal Quality	0.66
Average Orthogonal Quality	0.99
Maximum Aspect Ratio	12.29
Average Aspect Ratio	3.21
Maximum Skewness	0.56
Average Skewness	0.035

Table 19: The Hexahedral Mesh Cell Parameters